

INFORMATION TO USERS

This manuscript has been reproduced from the microfilm master. UMI films the text directly from the original or copy submitted. Thus, some thesis and dissertation copies are in typewriter face, while others may be from any type of computer printer.

The quality of this reproduction is dependent upon the quality of the copy submitted. Broken or indistinct print, colored or poor quality illustrations and photographs, print bleedthrough, substandard margins, and improper alignment can adversely affect reproduction.

In the unlikely event that the author did not send UMI a complete manuscript and there are missing pages, these will be noted. Also, if unauthorized copyright material had to be removed, a note will indicate the deletion.

Oversize materials (e.g., maps, drawings, charts) are reproduced by sectioning the original, beginning at the upper left-hand corner and continuing from left to right in equal sections with small overlaps.

Photographs included in the original manuscript have been reproduced xerographically in this copy. Higher quality 6" x 9" black and white photographic prints are available for any photographs or illustrations appearing in this copy for an additional charge. Contact UMI directly to order.

**Bell & Howell Information and Learning
300 North Zeeb Road, Ann Arbor, MI 48106-1346 USA**

UMI[®]
800-521-0600

NOTE TO USERS

This reproduction is the best copy available

UMI

GPS SENSING FOR FORMATION FLYING VEHICLES

A DISSERTATION

SUBMITTED TO THE DEPARTMENT OF AERONAUTICS & ASTRONAUTICS

AND THE COMMITTEE ON GRADUATE STUDIES

OF STANFORD UNIVERSITY

IN PARTIAL FULFILLMENT OF THE REQUIREMENTS

FOR THE DEGREE OF

DOCTOR OF PHILOSOPHY

By

Eric Alan Olsen

November 1999

UMI Number: 9961942

**Copyright 2000 by
Olsen, Eric Alan**

All rights reserved.

UMI[®]

UMI Microform 9961942


**Copyright 2000 by Bell & Howell Information and Learning Company.
All rights reserved. This microform edition is protected against
unauthorized copying under Title 17, United States Code.**

**Bell & Howell Information and Learning Company
300 North Zeeb Road
P.O. Box 1346
Ann Arbor, MI 48106-1346**

Copyright © 2000 by Eric Alan Olsen


All Rights Reserved.

I certify that I have read this dissertation and that in my opinion it is fully adequate, in scope and quality, as a dissertation for the degree of Doctor of Philosophy.



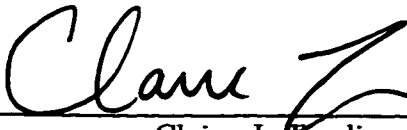
Jonathan P. How
Department of Aeronautics and Astronautics
(Principal Adviser)

I certify that I have read this dissertation and that in my opinion it is fully adequate, in scope and quality, as a dissertation for the degree of Doctor of Philosophy.



Stephen M. Rock
Department of Aeronautics and Astronautics

I certify that I have read this dissertation and that in my opinion it is fully adequate, in scope and quality, as a dissertation for the degree of Doctor of Philosophy.



Claire J. Tomlin
Department of Aeronautics and Astronautics

Approved for the University Committee on Graduate Studies:



To Mikaela and Rachel

Abstract

Autonomous formation flying technologies have the potential to revolutionize many future space and earth science missions such as surveillance, earth mapping, and stellar interferometry. One important application is to use this new technology to develop a virtual spacecraft bus that is comprised of a cluster of small, inexpensive spacecraft that fly in formation and gather concurrent science data. This novel concept distributes the functionality of a large satellite amongst smaller, less expensive, cooperative satellites, thereby significantly enhancing the mission flexibility and robustness. GPS sensing plays a key role in making formation flight a reality.

Differential carrier phase measurements can be to obtain the centimeter level relative position estimates between the vehicles within the formation. However, before these measurements are available, we must solve for the “Integer Ambiguities”. One standard approach is to wait for the GPS satellites to move about overhead, but, for many formation flying missions this will take too long. An alternative solution is to augment the vehicles in the formation with onboard transmitters, which then allows relative vehicle motion to be used to solve for these biases. A key question is then: What is the best (optimal) formation maneuver to undergo? Several quasi-optimal initialization algorithms are developed, and compared to the optimal solution. As part of this development, a measure for the bias observability, the formation NDOP,

is derived. This measure is used to optimize the trajectories for the initialization maneuvers.

Several other issues related to formation flight are also described. Key among these are system robustness and the effects of the polarization of the GPS signal on the measured carrier-phase. Two algorithms are presented which address the robustness of the state estimation. Additionally, a method to account for the polarization is described, along with a convergence proof of the algorithm.

To understand the GPS formation flying problem better, a unique testbed was created to test algorithms, and provide proof of concept. This testbed consists of two lighter-than-air vehicles (blimps), which operate in a large indoor GPS laboratory. In addition, a new, attitude capable receiver was developed for use on the vehicles. A description of the blimp testbed and receiver are given. Experimental flight results are presented for both a single blimp and a two blimp formation. These experiments demonstrated that centimeter-level relative positioning was obtained using differential carrier-phase GPS.

Acknowledgments

I would like to thank several individuals for making this thesis possible. The blimp testbed was the brainchild of my principal advisor, Jonathan How. His guidance, technical expertise, and dedication were appreciated. Thanks also go to my Orals committee: Stephen Rock, Per Enge, Claire Tomlin and Heinz Furthmayr. I would also like to thank Brad Parkinson for first introducing me to GPS, and for his support during my stay at Stanford.

This research would not have been possible without the funding and support of the Charles Stark Draper Laboratory (contract DL-H-505325).

There are several students, in particular, who I would like to thank. Chan-Woo Park worked on various aspects of this project, and will be continuing on with the research on formation flying vehicles. Building blimps would not have been the same without him. Many hours were spent in various discussions (some technical, some not) with Carl Adams, Jon Stone, Gabe Elkaim, Tobe Corazzini, Franz Busse and Roger Hayward.

The following students made my time at Stanford more enjoyable: Dave Rodriguez, “Jk” Chow, Brad Betts, Rick Lu, Brian Engberg, Andrew Robertson, Eric Prigge, Bruce Woodley, Mark Meyer, and one or two others I’m probably forgetting.

Finally, I would like to thank my family. My daughter Rachel provided many hours of comic relief and stress reduction. My wife, Mikaela, was supportive during our entire time at Stanford, and for that I thank her.

Contents

Abstract	v
Acknowledgments	vii
List of Tables	xv
List of Figures	xvii
List of Symbols	xxi
List of Acronyms	xxiii
1 Introduction	1
1.1 Formation Definition	2
1.2 Motivation	3
1.3 Example Formation Flying Space Missions	7
1.4 GPS Basics	9
1.4.1 Standard Pseudoranging	10
1.4.2 Differential Code-Phase GPS	12
1.4.3 Differential Carrier-Phase GPS	13
1.5 Related Work	14

1.5.1	Formation Flying Work	15
1.5.2	GPS Sensing for Vehicle Control	16
1.5.3	GPS Hardware Development	17
1.6	Research Issues	17
1.7	Contributions	18
1.7.1	Demonstrated Robust, 3-D Formation Flight	18
1.7.2	GPS Receiver Development	19
1.7.3	Carrier-phase Bias Initialization	19
1.7.4	Estimation Robustness	20
1.7.5	General Formation Flying Issues	20
2	Experimental Testbed and Environment	21
2.1	Indoor GPS Environment	21
2.1.1	Pseudolite Constellation	23
2.1.2	Multipath	25
2.2	System Architecture	27
2.3	Blimp Vehicles	29
2.4	Software Architecture	34
2.5	Communication Protocol	35
2.6	Summary	38
3	GPS Receiver Design and Testing	41
3.1	Motivation	41
3.2	Hardware Description	42
3.2.1	Correlator Card	43
3.2.2	Interface Card	44

3.2.3	Attitude Receiver	46
3.3	Software	48
3.4	Hardware Testing	51
3.5	The Carrier Tracking Loops	56
3.6	GPS Signal Tracking	59
3.6.1	Integrity	59
3.6.2	Cycle Slip Detection	60
4	Formation State Estimation	67
4.1	Coordinate Systems	67
4.2	GPS Measurements	70
4.2.1	Carrier-Phase Measurements	70
4.2.2	Single Difference Carrier-Phase Measurements (Same Receiver)	71
4.2.3	Single Difference Carrier-Phase Measurements (Different Re- ceivers)	72
4.2.4	Double Difference Carrier-Phase Measurements	73
4.3	Far Constellation Approximation	73
4.4	Sample Time Error	75
4.5	Formation Measurement Equations - General Problem	78
4.5.1	Vehicle Attitude	79
4.5.2	Relative Positioning	80
4.6	Blimp Attitude and Position Coupling	85
4.7	Blimp Testbed Measurement Equations	85
4.8	State Estimation	87
5	Carrier-Phase Bias Initialization	91

5.1	Measurement Equations	91
5.2	Initialization of the Relative Position Biases	95
5.3	GPS Satellite Motion	96
5.4	Formation NDOP	101
5.5	Optimal Bias Initialization Maneuvers	106
5.6	Experimental Initialization Maneuvers	115
5.7	Quasi-Optimal Initialization Maneuvers	117
5.7.1	Dynamic Formulation	118
5.7.2	Way-Point Formulation	120
6	Formation Flying Algorithms	131
6.1	Polarization	131
6.1.1	Magnitude	131
6.1.2	State Solution Incorporating Polarization Term	134
6.2	All-Baseline-in-View	139
6.2.1	Attitude	140
6.2.2	Relative Positioning	141
6.3	Measurement Vector Re-formulation	142
6.4	Pseudolite Aided Attitude	144
6.5	Summary	149
7	Experimental Results	151
7.1	Single Blimp Maneuvers	152
7.1.1	Indoor Auto Landing Test	152
7.1.2	Indoor Circular Flight	160
7.1.3	Outdoor Station-Keeping	165

7.2	Formation Flight Test	166
7.2.1	Formation Flight Indoors	166
7.2.2	Outdoor Formation Flight	172
8	Conclusions	177
8.1	Summary of Contributions	177
8.1.1	Demonstrated Robust, 3-D Formation Flight	177
8.1.2	GPS Receiver Development	178
8.1.3	Carrier-phase Bias Initialization	178
8.1.4	Estimation Robustness	179
8.1.5	General Formation Flying Issues	179
8.2	Transitioning from an Indoor Testbed to LEO	180
8.3	Future Work	181
8.3.1	Outdoor Formation Flying Testbed	182
8.3.2	Self-Constellation	184
8.3.3	Next Generation GPS Receiver	184
8.4	Closing	185
A		187
	Bibliography	189

2

List of Tables

1.1	Cost Savings for Applying GPS Sensing to Spacecraft	4
1.2	GPS Estimation Accuracy	10
1.3	Standard GPS Measurement Error Model	12
2.1	Blimp Testbed Communication Protocol	38
3.1	GPS Receiver Options	42
3.2	Error STD (mm) for Zero-Baseline DCP Tests - Indoors	54
3.3	Error STD (mm) for Zero-Baseline DCP Tests - Outdoors	54
3.4	Prediction Error STD (cm)	63
5.1	Bias Initialization Times (sec)	100
5.2	Initialization Maneuver Statistics	117
5.3	Quasi-Optimal Initialization	126
7.1	Results of 10 Auto Landings.	156
7.2	Estimation Error in Landing Points.	156
7.3	Flight Error for Circular Maneuver.	162

2

List of Figures

1.1	Definition of a Formation of Vehicles.	2
1.2	Separated Spacecraft Interferometry Mission	4
1.3	Formation Flying Vehicles – Air to Air Refueling	6
1.4	Farming	7
1.5	TechSat 21	7
1.6	Carrier-phase Integer Ambiguity	13
2.1	Two Blimps in the Highbay Test Environment.	22
2.2	Mounted Pseudolite	24
2.3	The Back of a Mounted Pseudolite	24
2.4	Pseudo-Constellation in the Highbay.	24
2.5	SNR Plot Showing Robust Tracking Performance	26
2.6	Multipath Test Results	27
2.7	Blimp Sensing and Control System Architecture.	28
2.8	The Original Blimp	30
2.9	Closeup of Two Blimps.	32
2.10	The New Gondola	33
2.11	RC Motors	33
2.12	Props Used on Blimps	33

2.13	Key Components of the Flight Control Software Architecture. . . .	35
3.1	Correlator Cards	43
3.2	Interface Card	45
3.3	Receiver Block Diagram	47
3.4	New GPS Receiver	48
3.5	Winmon Display	50
3.6	Static Receiver Tests	53
3.7	Dynamic Receiver Tests	53
3.8	Tracking Loops	56
3.9	Differential Carrier Phase Plot	65
4.1	Formation Coordinate System.	68
4.2	Highbay Coordinate System.	69
4.3	GPS Signal	74
5.1	Initialization using GPS Satellite Motion.	99
5.2	Orbit Sim Flow Chart.	100
5.3	Algorithm Flow Chart.	110
5.4	Optimal Formation Maneuver.	111
5.5	Plot of X-Y Positions for Optimal Maneuvers.	112
5.6	Plot of X-Z Positions for Optimal Maneuvers.	112
5.7	LOS for Monte Carlo Simulation.	113
5.8	Experimental Maneuvers.	115
5.9	Algorithm Comparison.	128
5.10	Plot of X-Y Positions for Way-Point Algorithm.	129
5.11	Plot of X-Z Positions for Way-Point Algorithm.	129
5.12	Plot of LOS's for the Way-Point Algorithm	129

6.1	Maximum Double Difference Carrier-Phase Error	132
6.2	Predicted Blimp Position Error Due to Polarization Effects	134
6.3	Top Down View of Antenna Arrays	140
6.4	Number of Valid Measurements During a Blimp Flight	143
6.5	Pseudolite Aided Attitude - Dual Antenna System	146
6.6	Pseudolite Aided Attitude - Dual Antenna System	147
6.7	Sensitivity of Pseudolite Aided Attitude - Dual Antenna System	149
7.1	3-D Plot of Auto Landing Flight Path	153
7.2	Vertical and Horizontal Flight Paths.	154
7.3	Measured and Estimated Landing Points.	155
7.4	Auto Landing - Part I.	158
7.5	Auto Landing - Part II.	159
7.6	X-Y Plot of a Circular Blimp Flight	160
7.7	Altitude Plot of a Circular Blimp Flight	161
7.8	Circular Motion - Part I.	163
7.9	Circular Motion - Part II.	164
7.10	Station Keeping	165
7.11	X Axis Position of Formation Flying Blimps	167
7.12	Altitude of Formation Flying Blimps.	168
7.13	Yaw Angle of Formation Flying Blimps.	168
7.14	Indoor Formation Flight - Part I.	170
7.15	Indoor Formation Flight - Part II.	171
7.16	Indoor Formation Flight - Part III.	172
7.17	Outdoor Formation Flight - Part I.	174
7.18	Outdoor Formation Flight - Part II.	175

8.1	Trucks	182
-----	------------------	-----

List of Symbols

ψ_a	Vehicle Euler yaw angle
θ_a	Vehicle Euler pitch angle
ϕ_a	Vehicle Euler roll angle
ρ	Pseudorange measurement
τ	Clock bias
λ	GPS L ₁ carrier wavelength, 19.02 cm
λ_{L_1}	GPS L ₁ carrier wavelength, 19.02 cm
ν	Receiver electronics noise (white)
L_1	GPS L ₁ frequency, 1.575 GHz
L_2	GPS L ₂ frequency, 1.228 GHz
$\Delta\rho$	Differential code-phase measurement
ϕ	Carrier phase measurement
$\Delta\phi$	Differential carrier phase (DCP) measurement
$\nabla\Delta\phi$	Double difference DCP measurement
l	Antenna line bias
K_{ijk}	Geometric carrier integer ambiguity
P_{ijk}	Position vector
G	GPS geometry matrix
β	Bias
X	Position vector
d	Distance
los	Line of sight vector

h	Nonlinear DCP measurement function
h_d	Portion of nonlinear DCP measurement due to differential range
h_p	Portion of nonlinear DCP measurement due to polarization
H_p	Jacobian of h_p
H_d	Jacobian of h_d
y	Measurement vector
R	Measurement covariance matrix
P_N	Covariance matrix
L	Left null space
az	Azimuth
el	Elevation
$S_{avg_i}^k$	Average velocity of vehicle
W_i^k	Way-point
x	State
H_k	Jacobian of measurement function, h evaluated at \hat{x}_k
$T_{I/B}$	Transformation matrix
σ	Standard deviation
C	NDOP constraint

List of Acronyms

AU	Astronomical Unit
CDGPS	Differential carrier-phase GPS
DCP	Differential carrier phase
DGPS	Differential GPS
ECEF	Earth-Centered-Earth-Fixed
EKF	Extended Kalman filter
ENU	East-North-Up
FLL	frequency-locked Loop
GDOP	Geometric dilution of precision
GEO	Geosynchronous earth orbit
GPS	Global positioning system
HDOP	Horizontal dilution of precision
IBLS	Integrity Beacon Landing System
ICP	Integrated carrier phase
LEO	Low earth orbit
LOS	Line of sight
NAA	Non-aligned antenna array
NASA	National Aeronautics and Space Administration
NCO	Numerically controlled oscillator
NDOP	Bias dilution of precision
NMI	New Millenium Program
PC	Personal computer

PDOP	Position dilution of precision
PLL	Phase-locked Loop
PRN	Pseudo-random number
PWM	Pulse-width modulated
RC	Radio controlled
RF	Radio frequency
RHCP	Right hand circular polarization
RMS	Root mean squared
SA	Selective availability
SAR	Synthetic aperture radar
SNR	Signal to noise ratio
STD	Standard deviation
SSDL	Small Satellite Design Lab
TOF	Time of flight
UARTS	Universal asynchronous receiver/transmitter
UAVS	Unmanned air vehicles
UERE	User equivalent range Error
USAF	United States Air Force
VDOP	Vertical dilution of precision
WAAS	Wide Area Augmentation System
WLS	Weighted least squares

Chapter 1

Introduction

This dissertation presents theoretical and experimental results in the use of the Global Positioning System (GPS) as a sensor for a formation of vehicles. To successfully command and control a formation, a knowledge of the cluster's absolute position, as well as very precise estimates of the *relative* positions of the vehicles within the formation are required. To this end, both standard GPS sensing techniques (*e.g.* pseudoranging), and more advanced techniques, such as differential carrier-phase GPS (CDGPS) are used.

As part of this research, a unique testbed was developed to test and demonstrate GPS estimation algorithms in 3-dimensions. This testbed consists of several lighter-than-air vehicles (blimps), which are able to fly in formation both inside using a pseudo-constellation of satellites (pseudolites), and outside using the NAVSTAR constellation. In addition, a new, attitude capable GPS receiver was developed for use in this project.

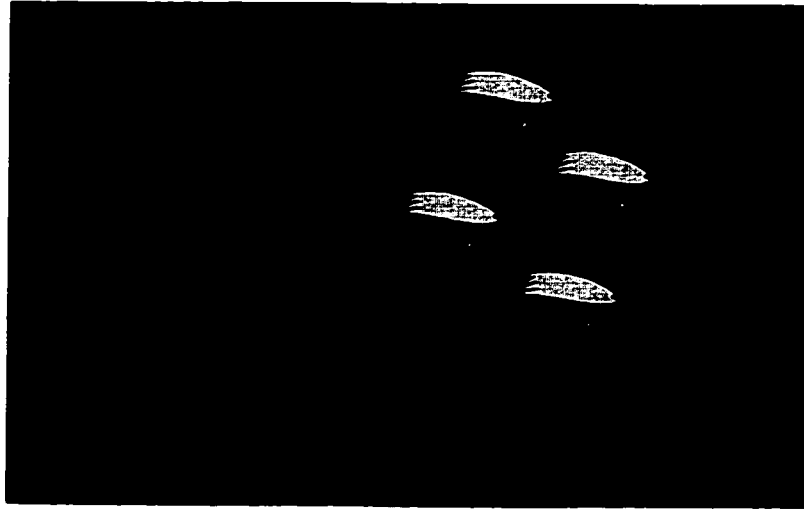


Fig. 1.1: Formation Flying Vehicles.

This thesis covers the algorithms that were developed for use in GPS sensing for formation flying vehicles, as well as the design, and implementation of the experimental testbed.

1.1 Formation Definition

Figure 1.1 shows a *formation* of vehicles somewhere in space. A formation is defined to be a group of multiple vehicles working together in a coordinated manner. The exact nature of their mission is not important, and can range over an vast array of possibilities, as will be discussed later in this chapter.

GPS can provide several modes of sensing which are important for a formation. These sensing options are discussed in detail throughout this thesis, but can broadly be broken down as follows:

1. Coarse (100 meter, single-point position solution) absolute position measurements for the formation position.

2. Precise (centimeter-level) *relative* position estimates between the vehicles within the formation.
3. Precise (mm/s) *relative* velocity estimates between the vehicles within the formation.

1.2 Motivation

The GPS system has made robust, all-weather, precise global navigation a reality for the past decade [BWP96-1], but it has not been until recently that this technology has been applied as a sensor to formations of vehicles. The GPS system provides an array of sensing options for a formation, including: absolute positioning, relative vehicle positioning, attitude estimation, and precise timing. GPS can provide sensing across the entire array of formation flying missions in space (Figure. 1.2), in the air (Figure. 1.3), and on the ground (Figure 1.4). Additionally, significant cost savings can be obtained by using GPS on vehicles within a formation. Table 1.1 summarizes a NASA study on the potential savings of using GPS on spacecraft, and well as the improvements that can be made regarding formation flight.

Perhaps the most obvious formation flying application is that of a cluster of spacecraft in orbit about the Earth. GPS sensing can be used to replace the traditional array of sensors found on many space vehicles, which will lead to a reduction in the weight, power consumption, vehicle cost, and ultimately a reduction in mission ground support costs through enhanced vehicle autonomy [FB97].

The objective for formation flying space science missions is to replace the traditional approach of using a single monolithic satellite (such as Landsat-7) [JCA96, TC97], with a *virtual spacecraft bus* consisting of a cluster of autonomously controlled vehicles. This technology can then be applied to a number of distributed observation missions, including: earth mapping (SAR, magnetosphere), astrophysics (stellar

Table 1.1: Cost Savings for Applying GPS Sensing to Spacecraft (Compiled by NASA GSFC Guidance Navigation and Control Technology Office [FB98])

Spacecraft System	Potential Savings	Achieved Through	Other Improvements
<i>Operational Savings</i>			
Ground Operations and Scheduling	\$100k's-\$M's/year	Autonomous vehicle operations	Hand-off operation, formation flight
Navigation Tracking	\$100k's/year	On-orbit Navigation	Better accuracy, real-time positioning
<i>Design Savings</i>			
Precision Timing	\$1M	Replaces on-board atomic clocks	Synchronization across multiple spacecraft
Attitude Determination	\$100k's	Replaces other attitude sensors	Improved reliability, reduced power and mass
Spacecraft Design and Testing	\$100k's	Reduces interfaces, COTS hardware	Quicker design time, less project risk

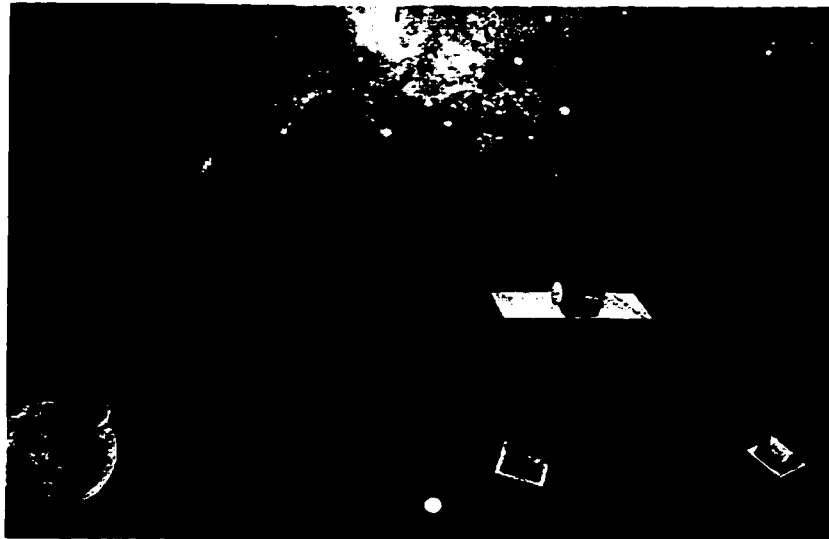


Fig. 1.2: Formation Flying Example from the NASA-JPL Separated Spacecraft Interferometry Missions (DS3 [KL97] and TPF [TPF])

interferometry), and surveillance [TS21, TPF]. The formation flying concept is a key part of both the NASA, and USAF vision for the future [VIS].

The overall objective for formation flying space science missions is to accomplish these science tasks using a distributed array of very simple, but highly coordinated, spacecraft (e.g., micro-satellites). This approach represents a new systems architecture that provides many performance and operations advantages:

1. Enables extensive co-observing programs to be conducted autonomously without using extensive ground support, which should greatly reduce operations cost of future science missions.
2. Increased separation (baseline) between instruments could provide orders of magnitude improvement in space-based interferometry. A distributed array of spacecraft will significantly improve the world coverage for remote sensing, and will enable simultaneous observations using multiple sensors.
3. Replacing the large complex spacecraft of traditional multi-instrument observatories with an array of simpler micro-satellites provides a flexible architecture that offers a high degree of redundancy and reconfigurability in the event of a single vehicle failure.
4. Places the design emphasis on building and flying the science instruments, not on the development of the bus platform itself. Allows standardization of the satellite fabrication process, which will reduce costs.
5. Enables the low cost, short lead-time instruments to be built, launched, and operated immediately. The more costly, long lead-time instruments can then join the fleet when available. This approach would also allow new or replacement instruments to join the formation as they are developed or needed.

Typical airborne formation flying missions include air-to-air refueling and unmanned air vehicles (UAVS). Future wide-area surveillance systems mounted on



Fig. 1.3: Formation Flying Vehicles – Air to Air Refueling

UAVS and operating in formation will be capable of collecting SAR imagery at significant rates [CR96]. The relative location of these devices will be required for accurate analysis and synthesis of the data. GPS sensing also has the potential to automate the refueling operations of aircraft during poor weather, and night missions, which could lead to a reduction in linkup times and increased safety [RH99].

Further potential applications include ground based formations of farming equipment (*i.e.* tractors, harvesters, combines, etc.), which is of significant commercial interest. Multiple pieces of equipment operating in precise formations will result in an increase in efficiency, and a significant reduction in waste [MOC97]. GPS will facilitate operations during darkness, dust, fog, and at high speeds. Ultimately, the autonomous formations may be used to replace human labor, freeing up workers for other endeavors.



Fig. 1.4: Farm Equipment in Formation



Fig. 1.5: AFOSR Tech-Sat 21 Space-based Radar Mission for Ground Moving Target Indication [TS21].

1.3 Example Formation Flying Space Missions

There is strong interest in the formation flying concept as a result of two missions that are currently under development as part of the NASA New Millennium Program (NMP). The first, the New Millennium Interferometer (NMI), is a formation of three spacecraft in either GEO or solar orbit (0.1 AU from the Earth) to be used for long baseline optical stellar interferometry [MC97]. As shown in Figure 1.2, two of the spacecraft will be light “collectors”, separated by several kilometers, that focus light from a distant star onto a third “combiner” spacecraft that forms the interference pattern. To form this pattern, the optical path between the spacecraft must be controlled to within a fraction of a wavelength of light. A layered control approach has been proposed to achieve this level of precision. One layer of which will use CDGPS type sensing to regulate the formation relative positions to within a centimeter [KL97].

Very precise formation flying of this type would also be required for distributed SAR and Earth imaging missions.

The second is the EO-1 mission which is planned to be a co-flyer with the Landsat 7 spacecraft [FB97]. The scientific goal of the EO-1 mission is to validate the results obtained with the multi-spectral imager onboard Landsat 7 by taking images with a similar instrument on-board the EO-1 spacecraft. To achieve this, the two spacecraft must be flown in formation so that the relative distance between them can be controlled such that the EO-1 imager is viewing the Earth through the same column of air as the Landsat 7 imager. This will require a formation flying accuracy on the order of 10-20 m, which is an example of coarse formation flying. The initial objective was to demonstrate formation flying using the EO-1 and Landsat 7 spacecraft, but because of a variety of budget and time constraints, no cross link will be possible between the two spacecraft. EO-1 will demonstrate on-board closed-loop autonomous orbit control using AutoCon™, which represents a key step. However this will not provide a true demonstration of formation flying spacecraft.

The Air Force Research Laboratory is also exploring this new paradigm for performing space missions in a coordinated effort called *TechSat 21* (Technology Satellite of the 21st Century) [AFR]. A variety of missions are currently being analyzed for applications such as surveillance, passive radiometry, terrain mapping, navigation, and communications. Figure 1.5 shows an example of a space-based radar mission for ground moving target indication was chosen as the focus of the initial investigation.

1.4 GPS Basics

The Global Positioning System currently consists of 27 satellites and a number of ground stations that track and monitor the constellation. Each satellite is in a 12 hour, circular orbit about the earth. The GPS satellites are in six separate orbit planes, each inclined by approximately 55 deg and the orbits are phased such that the constellation is able to provide world-wide coverage, 24 hours per day. The ground stations monitor each satellite's health, and upload to each satellite an estimate of all the orbits, as well as other data that will be used to form the GPS navigation message [JJS96-1].

Each GPS satellite transmits a signal at both L_1 (1575.42 MHz) and L_2 (1227.6 MHz). The signal has a spread-spectrum structure, wherein the carrier is modulated by a pseudo-random code in order to provide multiple access within the same frequency band. The L_1 signal is modulated by the course acquisition (C/A) code with a frequency of 1.023 MHz, and the P-code (encrypted Y-code) with a frequency of 10.23 MHz. The L_2 signal is modulated by the P-code only. Each signal has a navigation message included within it which provides various pieces of information, including the constellation's almanac and timing information. Due to the fact that the P-code is generally encrypted for military use, civilian users are only able to track the C/A code on L_1 . For this reason, the receivers used on the blimp testbed are only capable of tracking the C/A code on L_1 .

Users around the world can track the GPS signal, and are able to perform navigation with various degrees of accuracy, depending on the mode of operation. The available accuracies are listed in Table 1.2. The formation's absolute position will be derived from standard pseudorange techniques, and will result in measurement errors of ≈ 100 m (single-point solution). Selective Availability (SA) is the intentional

degradation of the clock model transmitted by each satellite. This degradation is imposed by the U.S. military, and does not effect military receivers capable of tracking the P-code. Pseudoranging derives the position estimate by measuring, in effect, the time of flight (TOF) of each GPS signal to the user. The relative positions of the vehicles within the formation are derived by using differential carrier-phase measurements, and can result in measurement accuracies of better then 0.10 m. The main challenge of using differential carrier-phase measurements is solving for the “integer ambiguity” [GPS96]. This will be discussed in detail in Chapter 5.

Table 1.2: GPS Estimation Accuracy

Method	Position Errors (m)	Comments
Pseudoranging (SA on)	≈ 100	Measures time of flight (TOF) of signal
Pseudoranging (SA off)	≈ 15	Measures time of flight (TOF) of signal
Differential Code	1-5	Differences formed between different receivers
Differential Carrier-Phase	< 0.10	Must solve for “Integer Ambiguity”

1.4.1 Standard Pseudoranging

Pseudoranging is based on the user measuring the “range” to each visible satellite, and provides an absolute position estimate. The coordinate frame is typically taken to be an Earth-Centered-Earth-Fixed (ECEF) frame, but may be related to any coordinate frame desired. Most hand-held receivers report position estimates in lat-long coordinates. Pseudoranging provides the absolute position of the vehicle formation

as a whole. The pseudorange measurement is of the form

$$\rho_i = |\tau_i - \tau_u| + \tau_u + \epsilon_{\rho_i} \quad (1.1)$$

where

ρ_i = pseudorange from satellite i

τ_i = position of satellite i

τ_u = user's position (absolute frame)

τ_u = user's clock bias

ϵ_{ρ_i} = errors due to atmospheric effects, satellite position and clock errors, selective availability (SA), receiver noise, multipath, etc

The satellite positions are available from the navigation message that is modulated on each GPS signal, and is known by the user. Atmospheric and relativistic effects are estimated using models computed by the receiver software. There are typically four states that are estimated in the single-point solution: the three user position states designated by the vector, τ_u , and the user clock bias, τ_u . These unknowns can be solved for if the user has visibility to at least four separate satellites. The accuracy of this estimation is driven by a number of measurement error sources as listed in Table 1.3. The major error source is currently SA, the intentional degradation of the satellite clock estimate. The position error is approximately equal to the User Equivalent Range Error (UERE) as shown in Table 1.3 times a scaling factor which is a function of the satellite geometry. This scaling factor is referred to as the Position Dilution of Precision (PDOP), and is typically on the order of 2-5, depending on how many satellites are visible and where the user is located [JJS96-2].

Table 1.3: Standard GPS Measurement Error Model [BWP96-2]

Error Source	One-Sigma-Error,m		
	Bias	Random	Total
Ephemeris Data	2.1	0.0	2.1
Satellite Clock (No SA)	2.0	0.7	2.1
Satellite Clock (SA)	20.0	0.7	2.0
Ionosphere	4.0	0.5	4.0
Troposphere	0.5	0.5	0.7
Multipath	1.0	1.0	1.4
Receiver Noise	0.5	0.2	0.5
RMS User Equivalent Range Error (No SA)	5.1	1.4	5.3
RMS User Equivalent Range Error (SA)	20.5	1.4	20.6

1.4.2 Differential Code-Phase GPS

Differential code-phase GPS techniques [BJ82] are based on measuring the pseudorange at a reference station which is at a fixed, known location. The resulting pseudorange measurements are then used by nearby users, who may use these measurements to form differences with their own pseudorange measurements (Eq.1.1). This differencing eliminates many of the common mode error terms, including the atmospheric effects, satellite position errors, and SA. The resulting difference equation has the form

$$\Delta\rho_i = |\tau_{ref} - \tau_u| + \tau_{u-ref} + \epsilon_{\Delta\rho_i} \quad (1.2)$$

In this case, τ_{u-ref} is the user clock bias relative to the reference station, and $\epsilon_{\Delta\rho_i}$ are the measurement errors. The error in this case is primarily driven by the receiver clock noise and multipath effects. The user is able to solve for their position relative to the reference station, and can then compute the absolute position by adding the

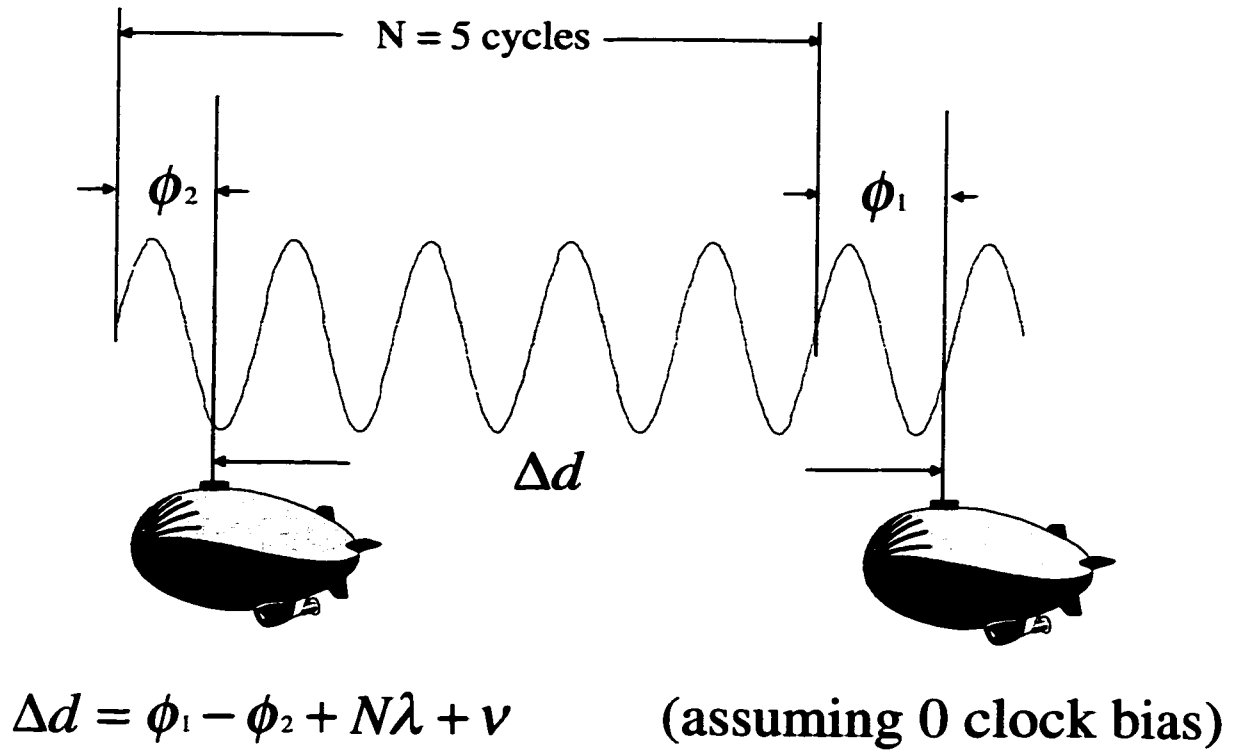


Fig. 1.6: Carrier-phase Integer Ambiguity

reference station's known location. Carrier-smoothed code measurements could also be used to improve the estimate of the pseudorange [GPS96].

1.4.3 Differential Carrier-Phase GPS

Differential Carrier-Phase GPS techniques are based on measuring the phase of the GPS carrier signal [GPS96]. This method is similar to the differential code method, in that the user's measured carrier-phase is compared to the measured phase at a reference station. However, because the accuracy of carrier-phase measurements is very precise (< 0.5 cm) [GPS96], these measurements can be compared between antennas with very short baselines. Differential Carrier-Phase measurements between

at least 3 antennas on a single vehicle can also be used to calculate the attitude of the vehicle [CC92].

The major difficulty in using the phase of the carrier signal is resolving the particular carrier wave cycle that is being looked at. This leads to the so called “integer ambiguity” problem, since the carrier cycles are effectively indistinguishable from one another. This is not a problem for code based methods (*i.e.* pseudoranging, differential code) because each chip in the C/A and P-codes is able to be resolved from one another [GPS96].

Figure 1.6 shows a 1-D plot of the GPS carrier wave between two different users. The receivers are able to measure the received phases, ϕ_1 , and ϕ_2 on the two different vehicles. The desired measurement is the actual distance between the two vehicles, Δd , but this will differ from the computed difference in measured phases by the “integer ambiguity”, designated by $N\lambda$. Effectively, there is an integer number of carrier cycles between the two users that can not be distinguished by the receivers themselves. Methods to solve for this ambiguity for the formation flying problem will be discussed in greater detail later in this thesis.

1.5 Related Work

GPS based sensing and control has been a major area of research at Stanford and elsewhere for two decades. This work encompasses a number of areas, to include vehicle control, the Wide-Area Augmentation System (WAAS) [KC93], the Local Area Augmentation System (LAAS) [CC94], signal structures, anti-jamming, and a host of other GPS based work. The related work can be broken down into a number of areas.

1.5.1 Formation Flying Work

Zimmerman applied GPS based sensing techniques to an indoor, experimental testbed using two free-flying robots [KZ95]. The testbed consisted of an array of six pseudolites placed around a granite table upon which the robots maneuvered. As part of this testbed, an overhead vision system was in place which was used to (re)initialize the vehicle locations whenever the estimation failed due to excessive signal outages. He corrected for the sample time error between receivers by incorporating a phase correction to the measurements. This necessity was eliminated in the blimp testbed by slewing the hardware sample rates in each receiver to a common time standard at 1 Hz. Zimmerman demonstrated that GPS could be used to sense the relative attitude and locations of the two vehicles, and was able to implement a controller using this sensing. However, the main limitation of the testbed was that the robots were constrained to lie in 2-dimensions and could only undergo very limited relative motion.

The work on the 2D testbed used by Zimmerman is being extended by Corazzini [TC98] to include an additional vehicle and onboard pseudolites. Her work is specifically addressing many of the hardware implementation issues related to incorporating transmitters on-board a vehicle. Instead of running the pseudolite signal through a splitter to the on-board receiver, the pseudolites in the testbed are being pulsed and are being tracked by the GPS antennas directly. As part of the work on this testbed, the vehicles are being moved to separate tables to increase the baselines, and allow for increased relative motion. Similar to the work done by Zimmerman, the vehicles are constrained to maneuver in 2-dimensions.

Binning investigated the use of GPS for relative satellite to satellite navigation using both L_1 , and L_2 [BP97]. His work did not use experimental vehicles, but

instead used a GPS simulator to provide a “hardware in the loop” demonstration. The concept of a formation flying “simulator testbed” is currently being extended by researchers at the Applied Physics Laboratory [DR99]. This testbed will have multiple GPS simulators working together which will then allow formation flying space missions to be simulated in hardware. Many of the issues related to transitioning from a terrestrial application to a mission in low-earth-orbit (LEO) (see Chapter 8) can be addressed and tested prior to launching the spacecraft.

1.5.2 GPS Sensing for Vehicle Control

GPS sensing for vehicle control was demonstrated by a number of projects, to include the autonomous radio controlled airplane [MP96], the autonomous helicopter [AC95], and the IBL system [DL96]. These examples utilized a fixed reference station about which the vehicles would maneuver. The IBL system also had in place two fixed pseudolites through which the airplane would fly. The result of this pseudolite “bubble pass” was that the carrier-phase integers could be rapidly computed. The carrier-phase integers were solved for by a simple batch least squares algorithm implemented as a smoother. However, Lawrence [DL96] also applied Kalman filtering techniques to the integer estimation problem to account for the GPS satellite motion.

Lightsey looked at the GPS sensing problem for spacecraft attitude determination and control [GL97], and many of his ideas have been incorporated into a space-qualified receiver developed by Loral [LORAL]. Attitude determination will be a requirement for any formation flying mission. His work looked at the carrier-phase initialization, and signal lock-on issues which will be a major concern in orbit due to the high relative velocities of the vehicles in the system to the GPS satellites. He addressed the all-baseline-in-view concept for the attitude problem.

1.5.3 GPS Hardware Development

Cohen developed an attitude capable receiver in 1992 by modifying some existing Trimble hardware [CC92]. This was the first device capable of supplying attitude solutions for reasonably short baseline systems (< 5 meters). The receiver multiplexed the signals from each of four antennas, which mitigated the effects of RF crosstalk, and eliminated any line bias errors due to different RF path lengths internal to the receiver. He experimentally demonstrated the working receiver on a small, private aircraft.

Cobb developed a small, light weight, GPS transmitter termed a “pseudolite” in 1996 [CS97]. This device was cheap enough to allow it to be practically used on many applications. It transmitted the standard L_1 carrier, with the C/A code modulated on top of it. The 50 bit/sec navigation message is user programmable, or may be neglected entirely. This device was refined by Stone [SJ99] with his work on GPS sensing for mining applications.

1.6 Research Issues

Precise formation flying requires an accurate measurement of the formation states, (*i.e.* the relative attitude and positions of the vehicles) as well as an estimate of the absolute formation location. To this end, standard GPS techniques (*i.e.* pseudo-ranging), as well as more advanced techniques such as carrier-phase differential GPS (CDGPS) are employed [GPS96]. Several challenges exist before GPS measurements can be used to robustly perform the state estimation for a formation of vehicles, either on Earth or in space.

1. The carrier-phase “integer ambiguities” must be solved for before the phase measurements may be used to estimate the position and attitude of the vehicles in the constellation.
2. The estimation must be made robust to frequent signal loss and degraded tracking performance. Signal loss can be a result of vehicle orientation changes, GPS satellite motion, or multipath.
3. The polarization of the GPS signal introduces another phase component that needs to be accounted for in the general problem formulation in order to obtain centimeter-level accuracies.
4. There are several issues related to transitioning a formation from an indoor laboratory to space, including: the high relative doppler between the formation and the GPS satellites, initialization (an orbit propagator may be required), and the space environment (which can effect the line biases, multipath, etc.). These are discussed in greater detail in Chapter 8.

1.7 Contributions

The objective of this thesis was to demonstrate that carrier-phase GPS provides a robust relative navigation sensor for formation flying vehicles. The following contributions were made as part of this research.

1.7.1 Demonstrated Robust, 3-D Formation Flight

Successfully demonstrated the first use of CDGPS sensing for formation flight in 3-D, both inside using a pseudo-constellation of satellites (pseudolites), and outside using the NAVSTAR system. To this end, a unique testbed consisting of two lighter-than-air vehicles (blimps) was constructed. An estimator was implemented on a real-time

operating system, and centimeter-level relative positioning, as well as precise, relative attitude was obtained. The results were validated in our experimental laboratory.

1.7.2 GPS Receiver Development

A key limitation in GPS related research is access to appropriate receiver hardware. This is especially true for the formation flying application, where multiple (low-cost, low-power, open architecture) devices will be required. Extensive hardware and software modifications were made to an available single antenna board, and an **expandable, cheap, open architecture, attitude capable** receiver was developed. This receiver has since formed the basis for several other projects, to include the SSDL Orion Missions [JH99], the Mars Exploration Project [EL99], the Non-Aligned Antenna Experiment [JCA99], and the next generation formation flying experiment (see Chapter 8).

1.7.3 Carrier-phase Bias Initialization

One of the main challenges in CDGPS estimation is the solution of the carrier-phase biases, which are required in order to navigate to centimeter-level accuracy. In order to rapidly solve for these biases, onboard pseudolite augmentation was proposed, which allows the relative vehicle motion to be used as an initialization technique. A measure of the bias observability for a formation of vehicles was derived, and several path-planning algorithms for initialization were developed.

1.7.4 Estimation Robustness

Robustness is an important issue for any system. This is especially true for space-borne formations, since onboard sensing problems will need to be fixed either remotely, or would require a manned-space launch. The measured carrier-phase can suffer from cycle-slips (extra or missing carrier cycles), especially at low SNRs. Additionally, the signals being tracked on the antennas on each vehicle can vary over short time scales due to general vehicle motion. Two algorithms were developed to address the robustness issue. The first is the “all baseline in view” measurement formulation, which accounts for the rapid loss and acquisition of signals on individual antennas on a vehicle. The second is a method to detect measurement errors caused by cycle slips. These two algorithms significantly increase the robustness of the state estimation.

1.7.5 General Formation Flying Issues

The circular polarization of the GPS signal introduces another component to the measurement vector which must be accounted for in the general formation flying application. This was analyzed for the blimp testbed, and a simple method to account for this effect was introduced. A convergence proof for the algorithm was developed.

In addition to being used as an initialization tool, onboard pseudolites may be used as an additional ranging signal as part of the general state estimation problem. To this end, a concept called “Pseudolite Aided Attitude” was proposed. The basic idea of which is that a vehicle’s attitude may be computed by using the measurements available on another vehicle from its own onboard pseudolite. The concept can be used to increase the system robustness, since the vehicle attitude estimate can be determined even in the event of an antenna failure.

Chapter 2

Experimental Testbed and Environment

This chapter provides a description of the experimental testbed designed and built for use in this research. This includes the following: system architecture, software architecture, blimp vehicles, pseudolites, flight electronics, and communications. A detailed description of the GPS receiver will be presented in Chapter 3. A description of the indoor GPS environment, and issues related to it, is also presented as this had a significant impact on the system performance, and robustness.

2.1 Indoor GPS Environment

The blimp testbed is located inside a large building on Stanford University (Figure 2.1). This figure shows a photo of the End-Station 3 highbay from one end, showing the region of the room used for the blimp tests. The dimensions of the room are $200' \times 60' \times 60'$.

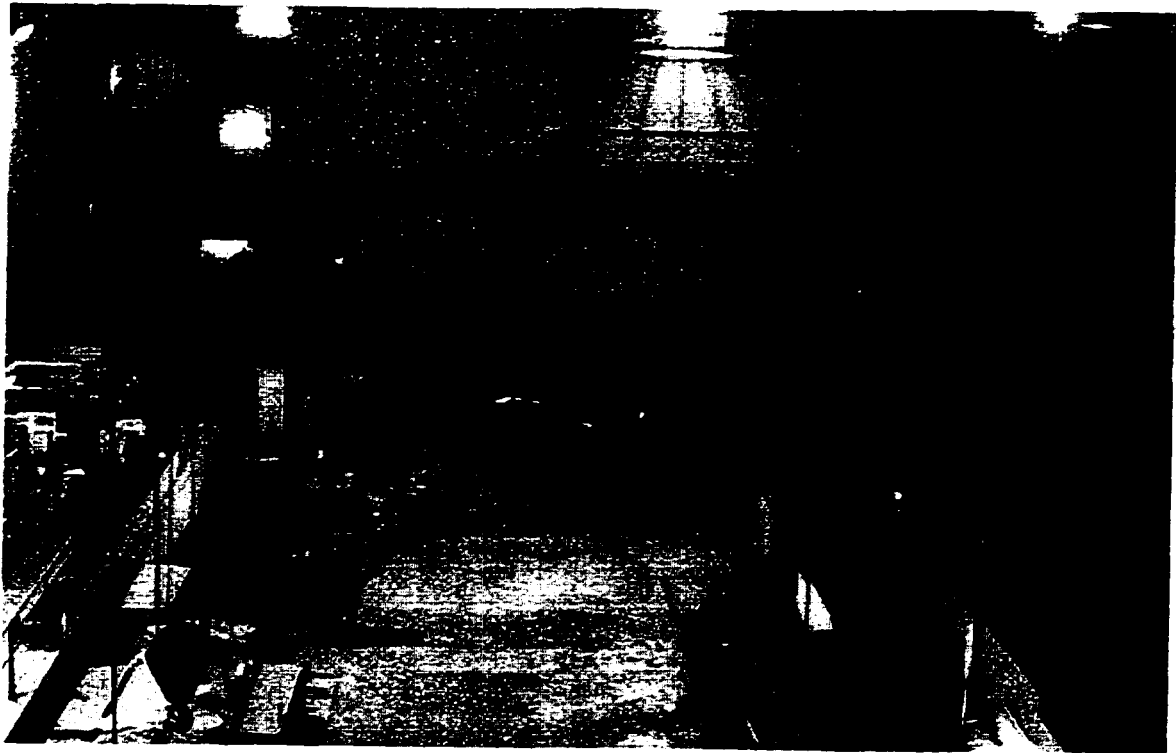


Fig. 2.1: The Blimps in the End-Station Highbay.

Operating multiple vehicles is extremely challenging, and the entire system is quite complex. One of the goals of this research was to create a multi-vehicle testbed which could be used to develop and test algorithms with as little difficulty as possible. Operations inside offers several key advantages:

- The environment is easily controlled (no wind, rain, or darkness), and is big enough to allow the vehicles to undergo large scale maneuvers. Mitigating the environmental impact on the blimps allowed us to concentrate on the technical aspects of the sensing problem.
- No need to move equipment (vehicles, computers, electrical generators) outside during development. Moving the blimp vehicles, in particular, is very difficult and time consuming due to their size.

Ultimately, operating inside allowed us to focus on the general aspects of the GPS sensing problem, without the drawbacks of operating outside (bad weather, darkness, etc.).

2.1.1 Pseudolite Constellation

The GPS signal is very weak, and is typically not available indoors. Thus, as with previous work on the 2D testbed [KZ96], a *pseudo-constellation* of satellites must be built and maintained. Figure 2.2 shows a picture of a typical pseudolite, which is a small signal generator that transmits the GPS signal for a selected pseudo-random number (PRN). Some of the pseudolites used in the blimp testbed are also capable of transmitting a user defined navigation message.

The main issue when operating pseudolites indoors is a trade-off between effective workspace and multipath. The GPS signal will reflect off the walls in the room and most objects that it comes in contact with. Multipath will cause a small (several centimeter), but effectively random (over large motions) error in the measured carrier phase at the receive antennas. This measurement error then translates into position errors as a function of PDOP [JJS96-2].

In an attempt to maximize the effective workspace, while at the same time keeping multipath to a minimum, several antenna designs were experimented with. Previous solutions have used helical (directional) antennas (see Figure 2.2). This minimizes multipath since the signal is radiated over a small cone angle, but it introduces large gradients in the signal power over the workspace as a result of the natural antenna gain pattern. An alternative solution that was extensively tested was the use of patch antennas, which radiate with a near constant gain over most of a hemisphere. The



Fig. 2.2: Mounted Pseudolite Showing the Helical Antenna and Ground Plane. The Signal Generator is Located Behind the Ground Plane.

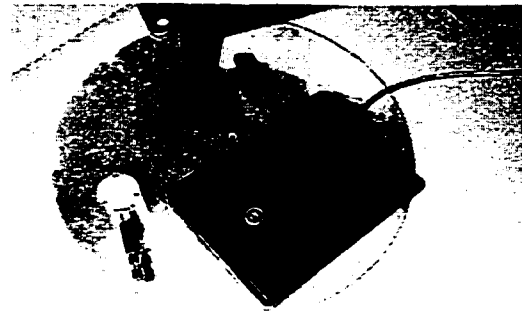


Fig. 2.3: The Back of a Ground Plane, Showing the Signal Generator and Variable Attenuator.



Fig. 2.4: Pseudo-Constellation in the Highway.

radiating field can be choked to a desired cone angle by using an RF absorbent material tuned to the GPS frequency. This approach was tested in the highway, but the experimental results indicated that this combination resulted in excessive multipath. This problem was further complicated by some apparent diffraction patterns near the edge of the cone angle.

Figure 2.4 shows the approximate locations of the final “pseudo-constellation”, which consists of 8 pseudolites with helical antennas tuned to produce radiating cone angles of about 50° . Two are located on the ceiling, above the workspace, while the other six are arrayed around the workspace, near the junction between the ceiling and walls. With this configuration, the effective GPS workspace is approximately 50' (length) \times 25' (width) \times 25' (height).

2.1.2 Multipath

A major challenge with indoor GPS are the significant multipath effects that must be contended with. The reflected signals cause a series of interference patterns throughout the GPS workspace, resulting in significant power fluctuations and localized power nulls. Figure 2.5 shows a plot of the signal-to-noise ratio (SNR) for a received GPS signal at an antenna as it was moved back and forth over several meters. The results are shown for two separate maneuvers, one inside the highbay, and the other outside. The SNR inside the highbay shows significantly larger variations than the maneuver outside. This effect degrades the performance of the receiver tracking loops, resulting in cycle slips and loss of lock. The power nulls (low SNR) that are visible on the plot occur with enough frequency to make robust performance inside a building a significant challenge. This effect, and the design of the receiver tracking loop required to track the signal robustly, is discussed in further detail in Chapter 3.

Carrier-phase measurement errors due to multipath are typically no more than a few centimeters [BM96], but multipath can have a much more pronounced effect on the measured code phase. The C/A code chip [GPS96] is about 300 m long, and typical code phase multipath errors are on the order of several meters. An experiment was performed both indoors and outdoors to measure the relative effect

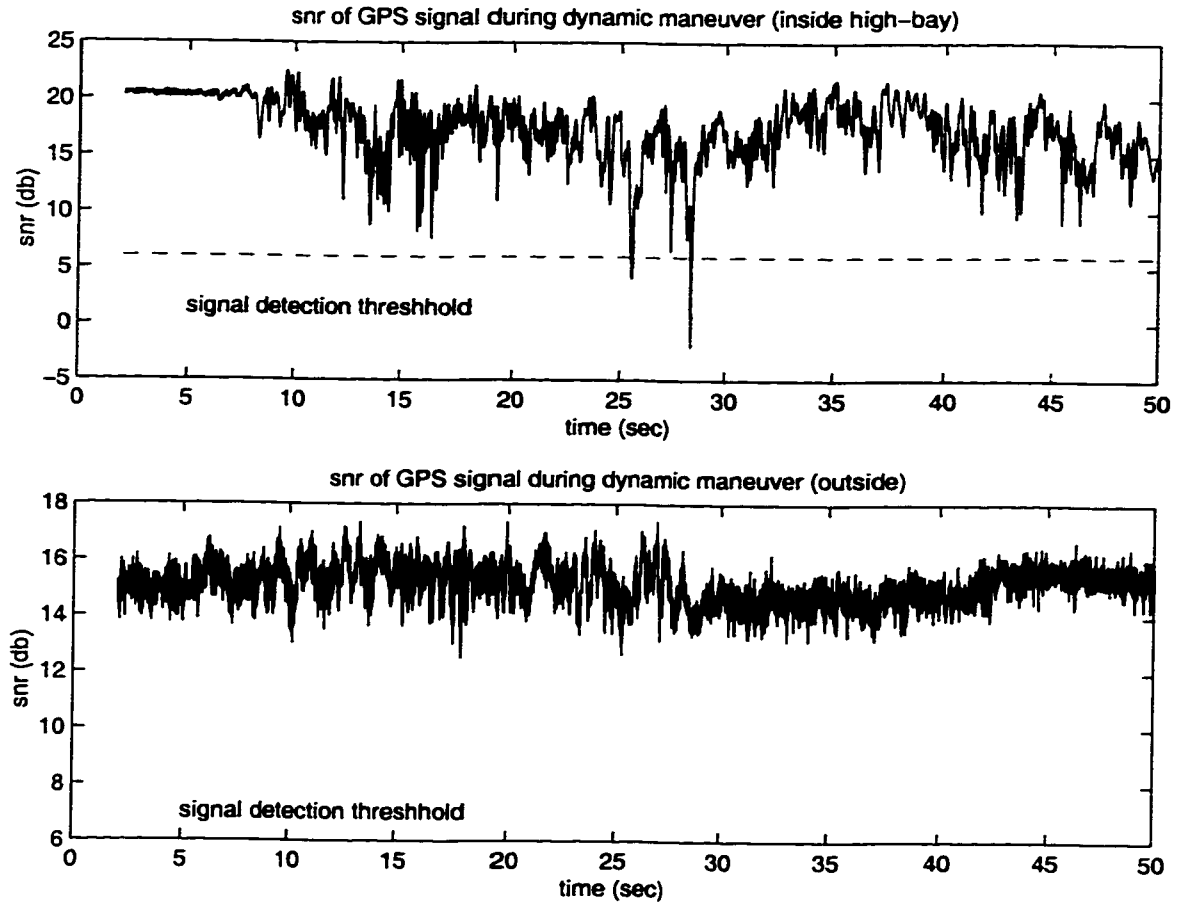


Fig. 2.5: SNR Plot Showing that the GPS Signal Suffers Through Momentary Drops in Power Indoors. The Signal Power is Much Smoother Outdoors.

of multipath on code-phase measurements. In the experiment, differential phase data was collected while an antenna was moved around a fixed antenna for 2 minutes. As shown in Figure 2.6, the outdoor smoothed differential code [GC90] phase change is coherent with the changes in the differential carrier phase. The differential carrier, and smoothed differential code measurements are synchronous over the course of the experiment. However, for the indoor case, the filtered differential code and carrier phase changes are not coherent (they are not the same). Despite the fact that the SNR value for the indoor data was significantly higher than the SNR values for the outdoor data (a smaller variance in the *raw* differential code phase is noticeable in the

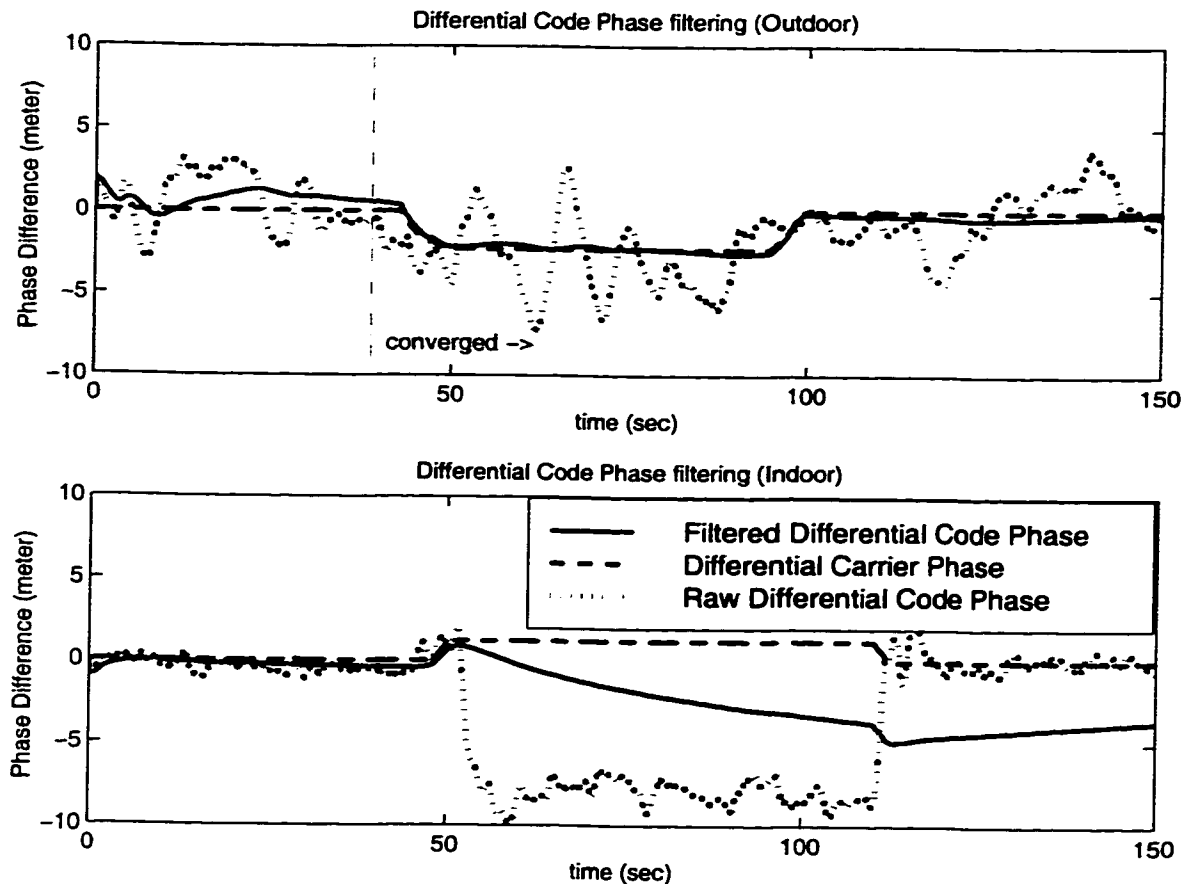


Fig. 2.6: Indoor (Bottom) and Outdoor (Top) Differential Code (Raw and Smoothed). The Plot Shows that the High Multipath Indoors Could Cause Large Positioning Errors for Measurements Based on the Smoothed Differential Code.

indoor plot), the errors in the indoor smoothed differential code phase will degrade the positioning solutions. These results indicate that the carrier-smoothed differential code will be useful as an additional signal outside, but due to multipath, is of limited utility indoors.

2.2 System Architecture

Figure 2.7 shows the basic architecture of the system. The testbed currently consists of two lighter-than-air vehicles (blimps) that are controlled by standard RC motors.

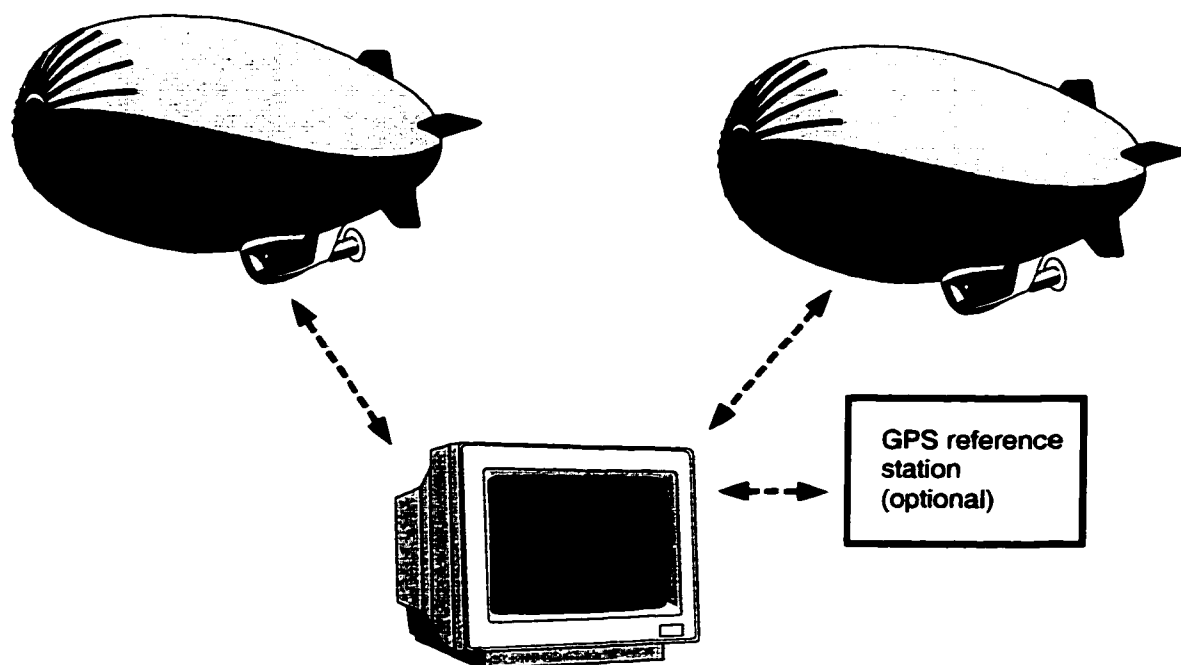


Fig. 2.7: The Basic Sensing and Control Architecture for the Blimp Formation.

Each vehicle has a gondola that houses the motors, GPS receiver, radio modem, micro-controller, and batteries. As shown in the figure, the blimps communicate with a ground station (computer) that is used to perform the control calculations. The long term goal is to move the control and estimation software on-board and have the vehicles communicate to each other directly. However, performing the calculations on the ground station has provided a very convenient development and debugging environment.

Under the current architecture, each vehicle transmits its sensor measurements (GPS) over the serial link to the ground station. The ground station updates the state estimates of the entire system, and then computes the necessary control commands to send to each vehicle. This greatly facilitates development, since most of the code resides on the ground station, where it can easily be debugged. Further, mission

commands (*i.e.* “move there”, “station keep”) can be conveniently entered from the keyboard of the ground computer.

The system also has in place a fixed GPS reference station, which allows operation of the system with only one vehicle. The reference station is optional when two or more vehicles are flying, but it does effectively simulate another vehicle within the constellation. Blimp vehicles were selected because they are capable of moving in 3-D, and are very easy to maintain and fly. Although it would be possible to use multiple RC airplanes or helicopters, experience has shown that a significant amount of time would be spent fixing and maintaining these vehicles. Of course, the blimp dynamics are quite different than would be expected for spacecraft on-orbit. But to create a formation of multiple vehicles, it is important to develop a simple design that is easily replicated, and can be *robustly* operated.

2.3 Blimp Vehicles

The blimp shown in Figure 2.8 was developed at the start of the project to perform a series of initial closed-loop tests. At the time this blimp was first built, the GPS receiver was still under construction, and most of the closed-loop tests were done using a digital compass for sensing. For those tests, the blimp position, and altitude were controlled manually, while the heading was commanded from the ground station, and the yaw motor loops were closed using the on-board microcontroller. Two antennas were added along the top of the blimp for closed loop testing with GPS sensing several months after its construction. The system identification and control design for the blimp was done by Park [DP98].

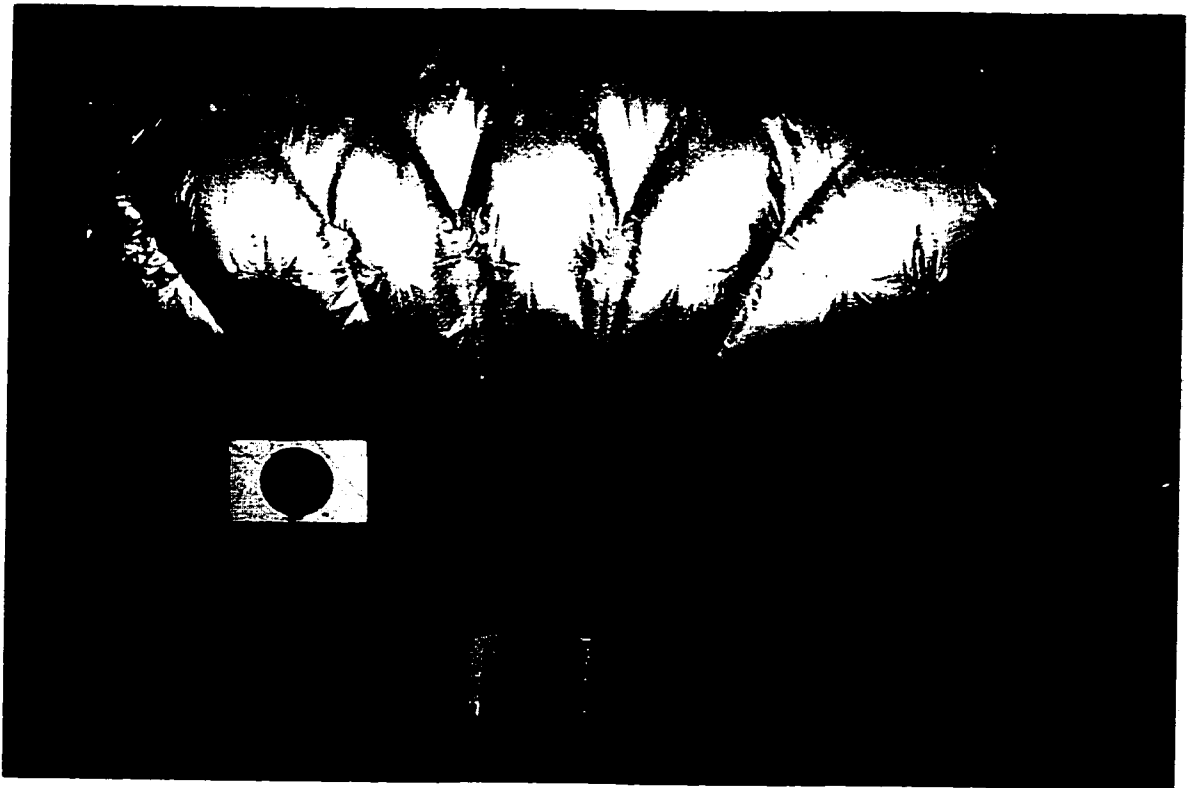


Fig. 2.8: The Original Blimp Developed to Demonstrate the Initial Closed-Loop Tests. Net Lift is on the Order of 20 Lbs.

The blimp bag was made from 1.5 mil, metalized Nylon which was purchased in spools 3 feet wide, and 100 feet long. The material has an adhesive coating along the back side, and can be patched together into arbitrary shapes by connecting smaller pieces together, and heating the adhesive sides up. In this manner, the cylinder shaped blimp bag was constructed from 7 pieces which were laid side by side, and patched together with a small, hand held iron. The spherical end caps were constructed separately, and patched on once they were completed. This operation took somewhere in the neighborhood of 50 man-hours, and was quite physically intensive, as the seams needed to be meticulously connected. A disadvantage of the 1.5 mil metalized Nylon is that it is somewhat fragile. For this reason, a large fishnet was used to encase the

bag, and the connections to the underlying gondola were made by using strings tied to the net.

The original blimp had the following features:

- 7 ft diameter by 13 ft long cylinder
- 400 cubic feet of helium giving a net lift of ≈ 22 lbs
- 1.5 mil metalized nylon skin
- approximately 5 lbs of electronics (motors) and batteries
- balsa wood gondola
- modem communication link to ground
- digital compass
- 2 GPS antennas

The original blimp (Figure 2.8) used only three radio controlled (RC) motors for control. Two were located in the gondola, one of which provided vertical actuation, and the other provided control along the long axis of the blimp bag. The motor attached to the styrofoam fin provided yaw control.

The original blimp did not have enough motors since sideways motion had to be attempted by performing *car-parking* maneuvers (*i.e.* small motions forward and backward while moving sideways). Further, the blimp bag could not be made substantially larger using the metalized nylon material. For this reason, the other blimps in the system were made using commercially available blimp bags. The only disadvantage of this is that they are about an order of magnitude more expensive than the handmade bags.

Figure 2.9 shows a closeup of the two blimps that were used for the formation flying tests, and most of the single vehicle test flights. The commercial blimp bags

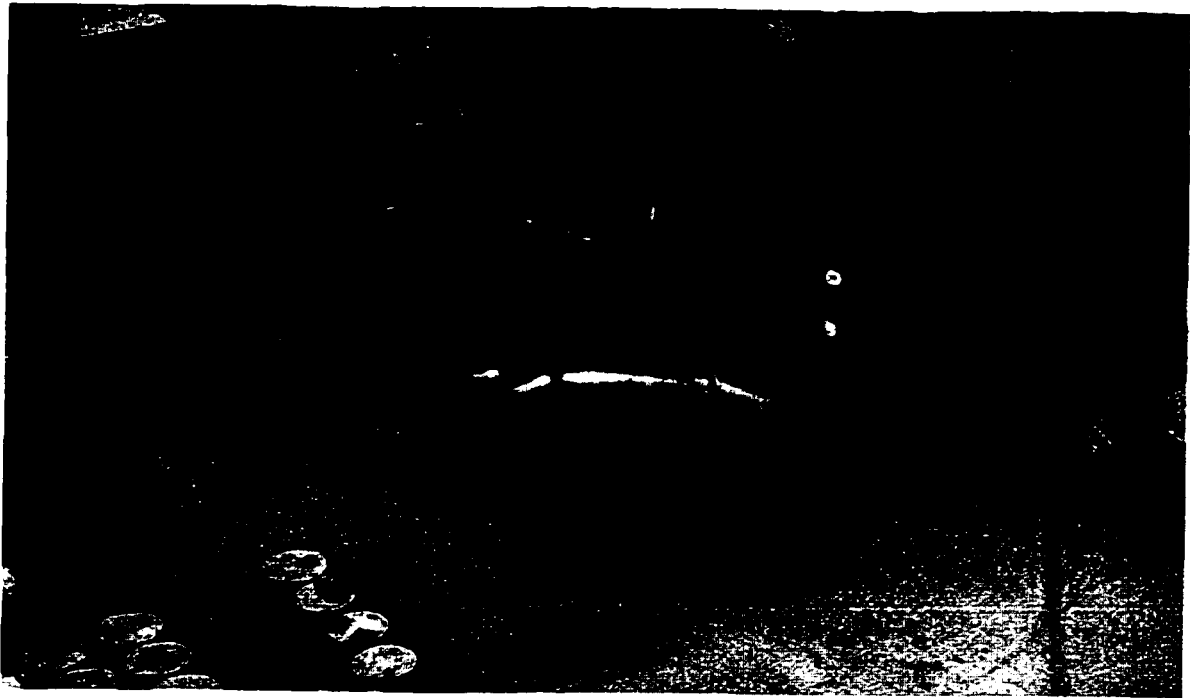


Fig. 2.9: Closeup of Two Blimps.

are made out of polyurethane, which is significantly more durable than the metalized nylon. The bags in the figure are 8 feet in diameter, and about 14 feet long. The commercial bags hold about 600 cubic feet of helium, and have a net lift of 28.6 lbs. The gondola is connected to the blimp from a series of patches connected directly to the bag itself. Visible on top of each blimp are three GPS antennas mounted in a T-pattern. The antennas are resting on small ground planes, and the array structure is made out of light weight styrofoam.

Figure 2.10 shows a close-up view of the balsa wood gondola for the new blimps. The gondola carries a total of five RC motors. Two motors provide vertical control, with a smaller motor being used for fine control when regulating altitude. The two motors at the ends of the gondola provide yaw control, and can also be used to move the blimp from side to side, without introducing any forward motion. The last motor

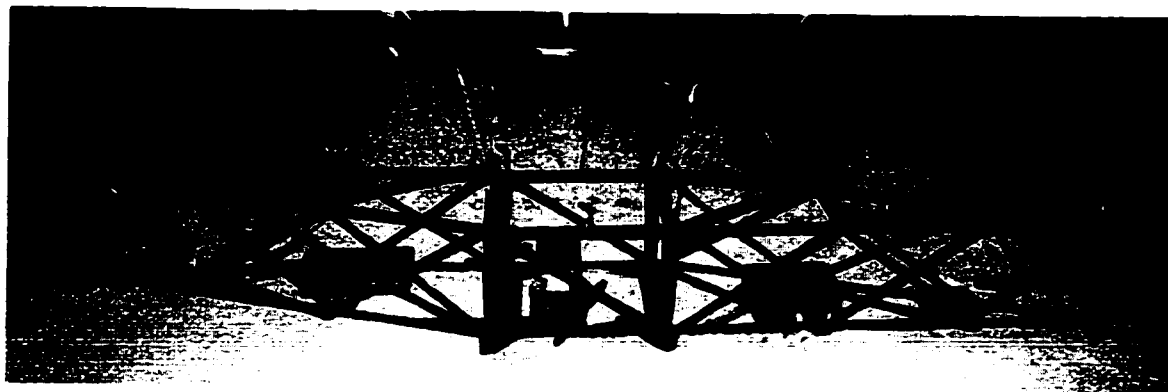


Fig. 2.10: The New Gondola Developed for the New Blimps. Note the Thrusters at the Front and Back that Provide Yaw and Sideways Control.



Fig. 2.11: A Photo of the Type of RC Motors, and Speed Controller Used to Actuate the Blimps

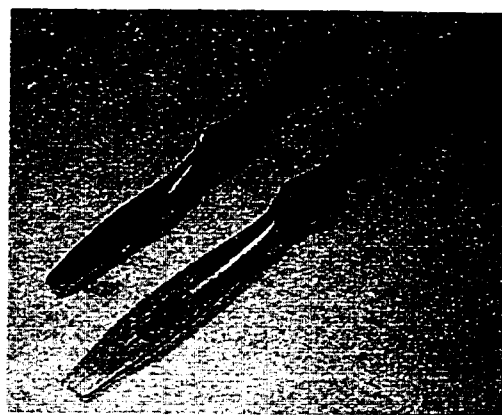


Fig. 2.12: A Photo of Typical Props Used on the Blimps

provides thrust along the axis of the gondola for forward/backward control. The GPS receiver, micro-controller, and batteries are carried near the middle of the gondola.

Figure 2.11, and 2.12 show the RC motors and props used on the blimp vehicles. The RC motors are Speed 400, and Speed 600 motors, available from most hobby stores. They provide 1-2 lbf of thrust, depending on the size of the prop mounted on the motor. The main disadvantage is the significant power requirement, which can

exceed 150 watts/motor. For this reason the blimps are required to carry multiple battery packs to actuate the vehicle.

The flight electronics include a speed controller for each motor, an HC11 microcontroller, power regulation circuitry, and miscellaneous circuitry for communications. The HC11 receives thrust commands from the ground computer, and converts the commands into a 50 Hz pulse-width modulated signal to drive the speed controllers. The power regulation circuitry provides DC power at both 5V and 12V to power the HC11, cooling fan, and modem. Because the communication system used the RS-232 protocol [HH80], a simple multiplexing scheme was built in hardware to allow the ground station to talk to both the on-board microcontroller and GPS receiver.

2.4 Software Architecture

Figure 2.13 shows a block diagram of the software architecture for the formation flying testbed. The software runs on a real-time operating system which allows separate threads of execution to be maintained for the principal blocks. A basic description is given as:

- User Interface - *GNU curses* library.
- Hardware Interface to Vehicle - radio link.
- Vehicles - 2-3 blimps.
- Satellite Tracking Manager - controls which satellites should be tracked by the system.
- Integer Manager - computes & maintains the estimates of the biases.
- State Estimator - computes the state estimate (relative positions and attitude) for the formation.

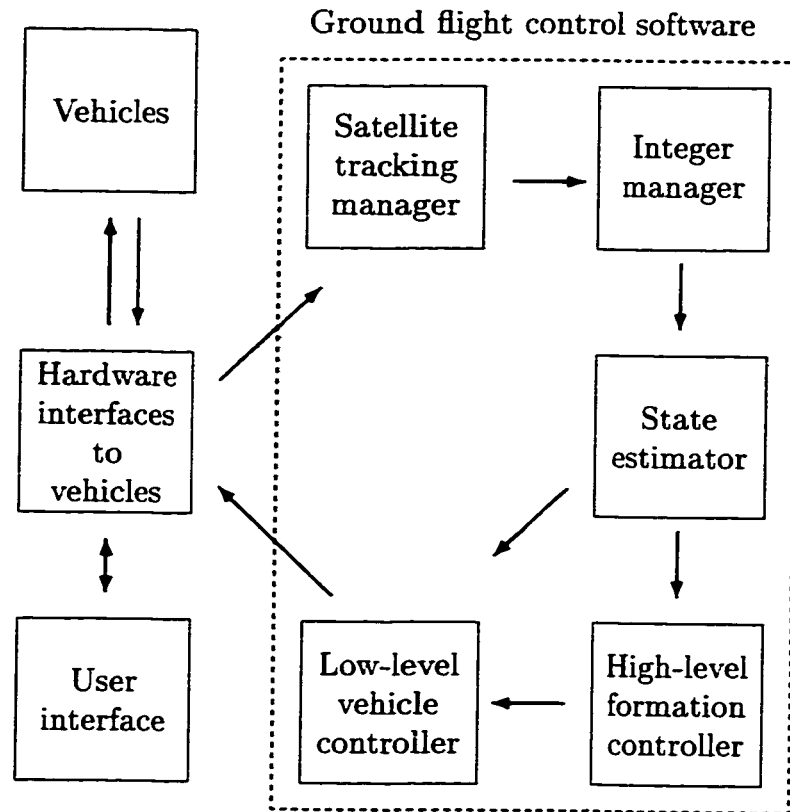


Fig. 2.13: Key Components of the Flight Control Software Architecture.

- High-Level Formation Controller - formation plan and task allocation.
- Low-Level Vehicle Controller - computes the commands that should be sent to each RC motor in the formation.

2.5 Communication Protocol

Some, or all, of the data shown below will need to be shared between the vehicles in the system in order to perform the state estimation. The specific data sent from each vehicle will depend on the particular implementation, and whether a GPS receiver is performing the relative navigation solution, or whether it is being performed by a separate processor (as in the case of the blimp testbed).

1. **Satellite PRN** - The data from each receiver channel should nominally be indexed by a satellite identifier. This is particularly important in space applications, where the actual satellites being tracked may differ from antenna to antenna, as will be the case for a vehicle with multiple non-aligned antennas [JCA99]. This data is sent for every channel in use.
2. **Satellite Line-of-Sight (LOS)** - The LOS from the vehicle to the specified satellite. This information will be available to every receiver in the system if they are generating a pseudorange positioning solution. However, this data will need to be sent if a separate (Non-GPS receiver) processor is used for the estimation.
3. **Measurement Time Stamp** - This is a time stamp at which the data was collected. It is taken to be the NAVSTAR GPS time calculated internal to each receiver when operating outside, and the code phase from an arbitrary pseudolite when inside. Only one time stamp will be sent at each epoch.
4. **Carrier-Phase Data** - This refers to the *integrated* carrier-phase measurement since signal lock-on. It will be initialized to 0 whenever a new satellite is brought on-line on the specific receiver channel. This data is sent for every channel in use.
5. **Carrier-Phase Rate Data** - These measurements can be used to estimate the relative velocities of the vehicles within the system. They can also be used to make phase corrections due to sample time errors between the receivers. This data is sent for every channel in use.

6. **Code-Phase Data** - Although not required for differential-carrier phase GPS, these measurements may be used to provide coarse (meter level) relative positioning. In particular, they will be valuable as an additional relative ranging sensor prior to the carrier-phase integer initialization. This data is sent for every channel in use.
7. **Cycle-Slip Flag** - The receiver may generate a warning when a cycle-slip occurred, or was likely to have occurred, on a specific channel. This gives the estimator a warning that the carrier-phase measurement was corrupted. This data is sent for every channel in use.

Each blimp vehicle sends a packet containing the necessary GPS sensing data to the ground station at 10 Hz. The need for this high data rate is primarily a result of the coupling between vehicle attitude and position that occurs inside the highbay (this will be addressed later in the thesis). This makes it impossible to compute the vehicle attitude on-board without having the measurements from the other vehicles (or reference station) in the system, and the dynamics of the blimps are such that the attitude needs to be computed at a minimum of 5 Hz. For typical formation flying systems that have visibility to the NAVSTAR constellation, it is likely that the system can perform with slower update rates. In this case, the attitude estimation can be performed by the on-board GPS receiver without knowledge of the other vehicle's location within the cluster. The information that needs to be shared between the vehicles in the formation will be used to perform the relative position estimation only, and these dynamics are likely to be slower for many applications (*e.g.* spacecraft on orbit, farm equipment).

The communication protocol for the blimp testbed assumed that the same signals were being tracked on each antenna in the system. This is obviously valid for indoor

Table 2.1: Blimp Testbed Communication Protocol

Message Data	Resolution	# of bytes
Time Stamp	1 μ sec	6
Carrier-phase Data	0.7 mm	4 per channel
Cycle-slip flag	Binary	2 (1 bit per channel)
Packet Overhead	N/A	5

operations, because the same 8 pseudolites are always in operation. This was implemented for the outdoor tests by having the ground station transmit to each vehicle the satellites that should be tracked, and on which channel they should be tracked. This facilitated the signal hand-over that occurred when a new satellite became visible.

The ground station for the testbed was not a receiver, and as such was not computing the satellite LOS's. Because of this, each blimp transmitted the satellite LOS for the signals it was tracking when operating outside. This was not necessary for operation inside the highbay as the pseudolite positions were at fixed, surveyed locations. The measurement time stamps were generated using the code phase of an arbitrary pseudolite when inside the highbay. The stamp was generated from GPS time when operating outside.

The communication data sent during testbed operations is summarized in Table 2.1. The receivers used on the testbed were capable of tracking on 24 separate channels. The data message sent by each blimp at 10 Hz contained a total of 109 bytes, which took ≈ 28 milliseconds when sent over a 38.4 Kbaud serial link.

2.6 Summary

One of the objectives of this project was to develop a simple, easy to maintain testbed for research on GPS sensing for multiple vehicles. The earlier testbed used robots

which were constrained to lie in 2-dimensions, and could only make very small maneuvers [KZ96]. In order to overcome these limitations, a new testbed was built which allowed large scale motions in 3-D.

The blimp vehicles are very easy to fly, and are effectively impossible to crash. Additionally, the simplicity of the design allows them to be cheaply, and easily replicated. Coupling the elegance of the lighter-than-air vehicle with the indoor laboratory enabled us to concentrate our efforts on the research goals of the project.

~

Chapter 3

GPS Receiver Design and Testing

This chapter provides a description of the GPS receiver developed for use on the formation flying testbed. This includes the receiver hardware, software modifications, and test data. This device was used on the blimp testbed, and also on a number of other Stanford projects to include: the non-aligned antenna experiment [JCA99], the Mars Exploration project [EL99], and the SSDL micro-satellite missions [JH99].

3.1 Motivation

Several GPS receivers have already been developed for space applications and these were compared using a variety of criteria: physical size, power required, number of channels, space experience, degree of familiarity at Stanford, cost, access to the source software, and performance. Table 3.1 summarizes this comparison for a number of different devices. Based on this analysis, it was clear that none of the available receivers were a good match in terms of the most important features: power, code access, and cost. Thus the decision was made to develop an in-house GPS receiver that would have:

Table 3.1: GPS Receiver Options

	SiRF	AOA TurboStar	TANS Vector	Honeywell SIGI
Size	10x5x3 cm	21x2x3.7 cm	13x21x6 cm	16x16x22 cm
Power	≈ 8 W	9 W	7.5 W	40 W
# channels	12	8	6	12
Space Experience	None	Orb View, SUNSAT, CHAMP, more	RADCAL, REX II, GADACS, more	Designed for space
Cost	Low	Medium	Medium	High
Software	C Source, not all access	Not all access	Assembly, not all access	Ada, not all access
Notes	Fast acquisition, but otherwise unproven	Complete, designed for LEO package	Most experienced space receiver, but "black box"	Space rated, full GPS/INS package

1. An open architecture with access to the receiver software,
2. Modular and easily expandable design so that it can be used to meet future project needs,
3. Attitude capable,
4. Low weight and power, and
5. Reasonably priced since multiple receivers will be required.

3.2 Hardware Description

The GPS hardware receiver design (Figure 3.3) is divided up into two major components: the correlator card and the interface board. The correlator card contains the GPS correlator, RF front ends, processor, and memory. The interface board provides an external clock signal (optional), power, and a serial interface to communicate with the user.

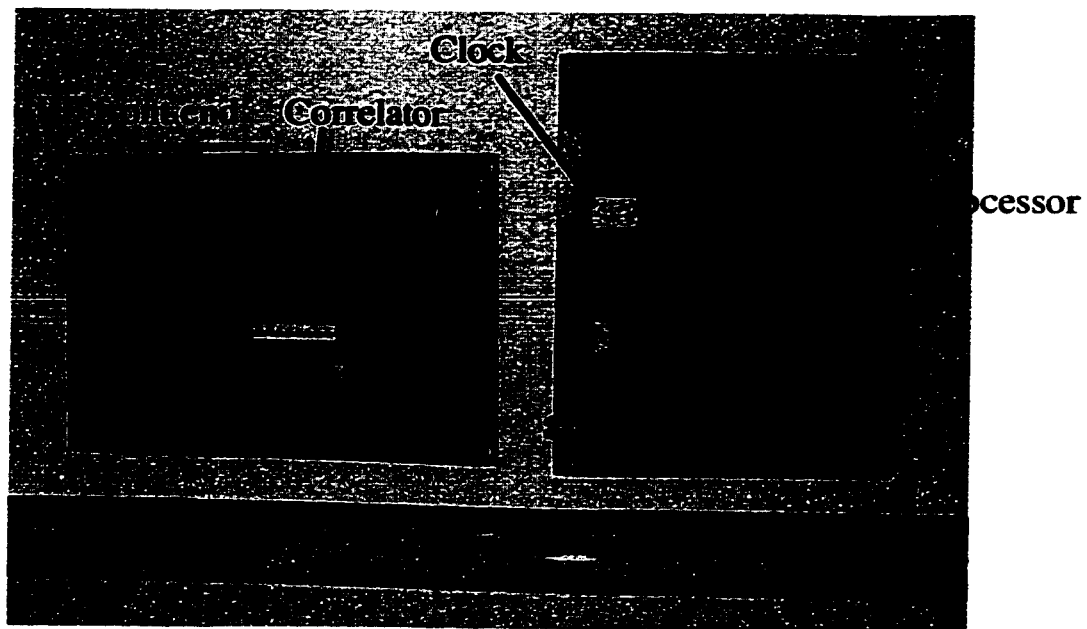


Fig. 3.1: Photo of the Front and Back of the Correlator Card

3.2.1 Correlator Card

Figure 3.1 shows a photo of the front (left) and back (right) of a correlator card. The Mitel corporation made available the design for the base line correlator card, which was a single antenna receiver capable of generating pseudorange positioning solutions.

An attitude capable receiver must be able to track GPS signals on multiple antennas. For this reason, a decision was made to modify the correlator card design in order to use the cards to build an attitude receiver for the testbed. The following hardware features were added:

1. An additional RF front end, providing two antenna capability on each board.
2. The ability to clock the card using either the onboard oscillator, or an off-board, external oscillator.

The final correlator card design has the following characteristics:

1. Total cost of parts and manufacturing is less than \$300,
2. 3" x 4" in size, weighs 65 grams, draws about 2.5 w
3. 2 RF front ends
4. 12 channels, which can be dynamically allocated between the 2 RF front ends.
5. Onboard ARM-60 processor
6. The user may set a jumper to use either the onboard oscillator, or an external oscillator signal which is routed to the board through an SMA connector.

This design allows as little as two cards to be connected together (which would allow for 4 antennas) to form the attitude receiver. Note that it was not clear at the beginning of the hardware design whether an external clock could be used to drive multiple cards, and this provided additional motivation to incorporate a second RF front end on each board. A common clock is an important feature required to eliminate the clock bias between the separate front ends. Fortunately, experimental results have shown that the design performs quite well (see Section 3.4).

3.2.2 Interface Card

The primary purpose of the interface board is to provide power to the correlator cards, and to interface with the two dual UARTs in the correlator chip (GP2021). At least two baselines (a minimum of three GPS antennas) are required to get a full 3-angle attitude estimate, hence two correlator cards must be used together to build an "attitude capable" receiver. With this in mind, the interface board was designed

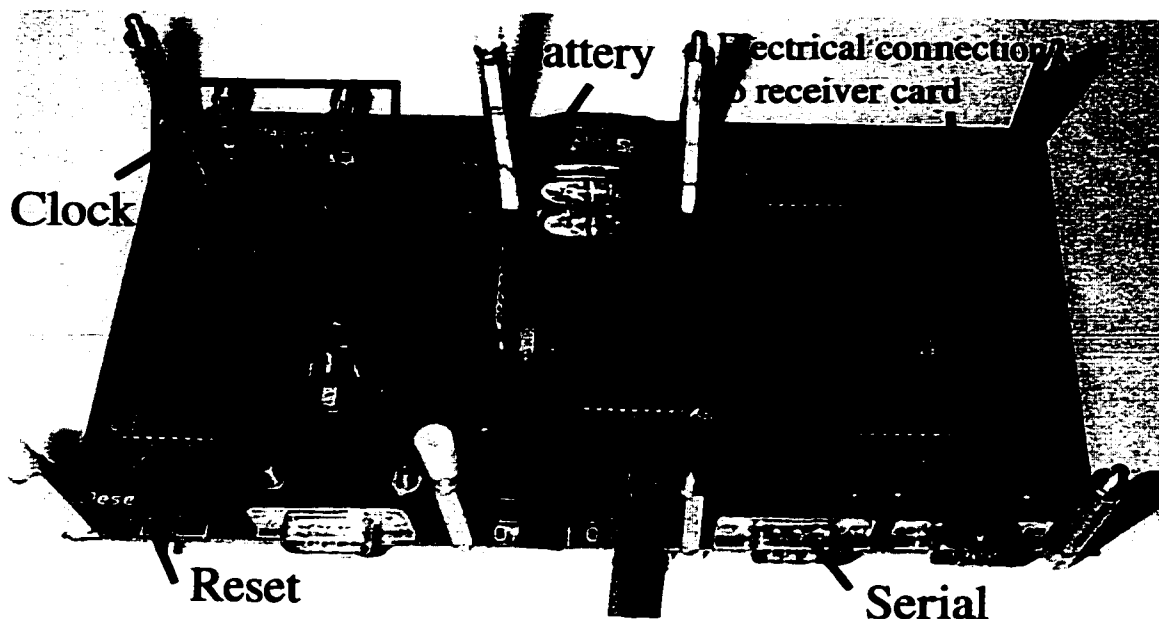


Fig. 3.2: A Photo of the Interface Board for the Receiver.

to mount two separate correlator cards together. Note that the interface board could be designed to allow for more than two correlator cards if more than 4 antennas are desired.

Figure 3.2 shows a photo of the interface card that was designed and built for the receiver. It has three DB9 connectors which are used to communicate with the processors on the correlator cards. One serial port is dedicated to each of the two correlator cards (Duart A on each card). The third serial port is able to communicate with both cards simultaneously (Duart B on each card). The dedicated serial ports facilitate inter-processor communications.

The clock circuitry consists of a Rakon 10 MHz oscillator, an op-amp used as a signal buffer, and some analog filtering. There are two SMA connectors visible in the clock circuit portion (top left) of the photo. These provide connections for the coax cable through which the clock signal is routed into the correlator cards. Also

visible is a 3.3 V Nicad battery (top middle) that provides back up power to the non-volatile memory on the correlator cards. This allows the receiver to maintain the GPS almanac in memory even when the device is powered down.

Of some concern during the initial design was the clock synchronization between the two correlator boards. In particular, the RF front end chips on each card have an internal phase-lock loop (PLL) [RB97] that tracks the 10 MHz signal generated by the oscillator (either internal or external). This clock signal is used by the front ends to generate a 40 MHz signal that in turn clocks the GP2021 correlator chip. The 40 MHz signal is used by the correlator to drive the internal code and carrier replicas, and it also clocks a binary shift register which determines when the GPS measurements are latched in hardware. Because the 40 MHz signal to each of the two correlators in the complete receiver are generated by different RF front ends (as must be the case because the GP2021's are on separate boards), there is the possibility that the correlator cards will latch the data at different times. In fact, this is what happens when the receiver is first powered on, because of the transients in the RF front end PLLs. Fortunately, this sampling offset is eliminated by "resetting" the receiver using the reset switch built into the interface card after the device is powered on. At this point there is at most a 12.5 ns sample time offset, which has a negligible impact on the differential carrier-phase measurements.

3.2.3 Attitude Receiver

Figure 3.3 shows a basic block diagram of the attitude receiver. The correlator cards are connected to the interface board by ribbon cable, and the clock signal is routed through low-loss coax cabling. Figure 3.4 shows a photo of the completed attitude receiver. It was packaged in a light weight aluminum box to protect the electrical

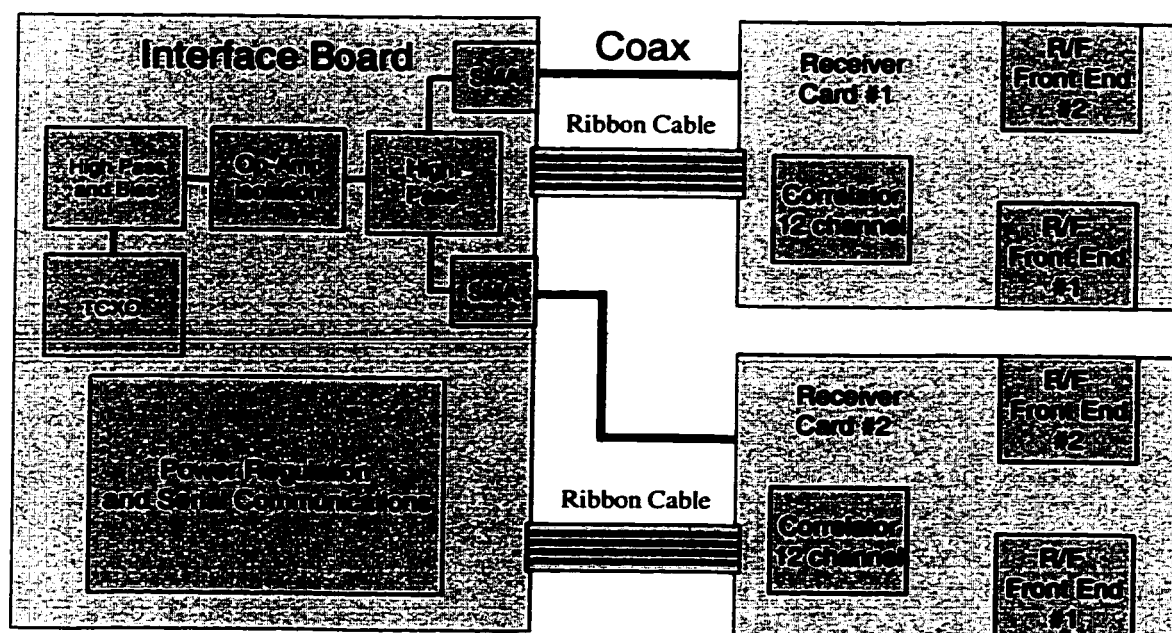


Fig. 3.3: Receiver Block Diagram Showing the Interface Board and Correlator Cards.

components, and for ease of handling. The inside of the box is lined with RF absorbent material tuned to GPS frequencies [RF]. This mitigated any interference potential from nearby jamming sources. Not shown in the photo is a small PC fan connected to one end of the aluminum box. This became necessary due to excessive heat build up inside the box when it was closed. The fan is able to keep the components at a low, uniform temperature.

The attitude receiver in Figure 3.4 has four RF front ends, which will allow four separate antennas to be connected to the device. The power regulator on the interface board has a rated input of upto 40 Volts. When all four antennas are operational, the receiver requires ≈ 5 watts.

The blimps used in the testbed have only three antennas. In order to track all eight pseudolite signals available in the highbay, the signal from one of the antennas

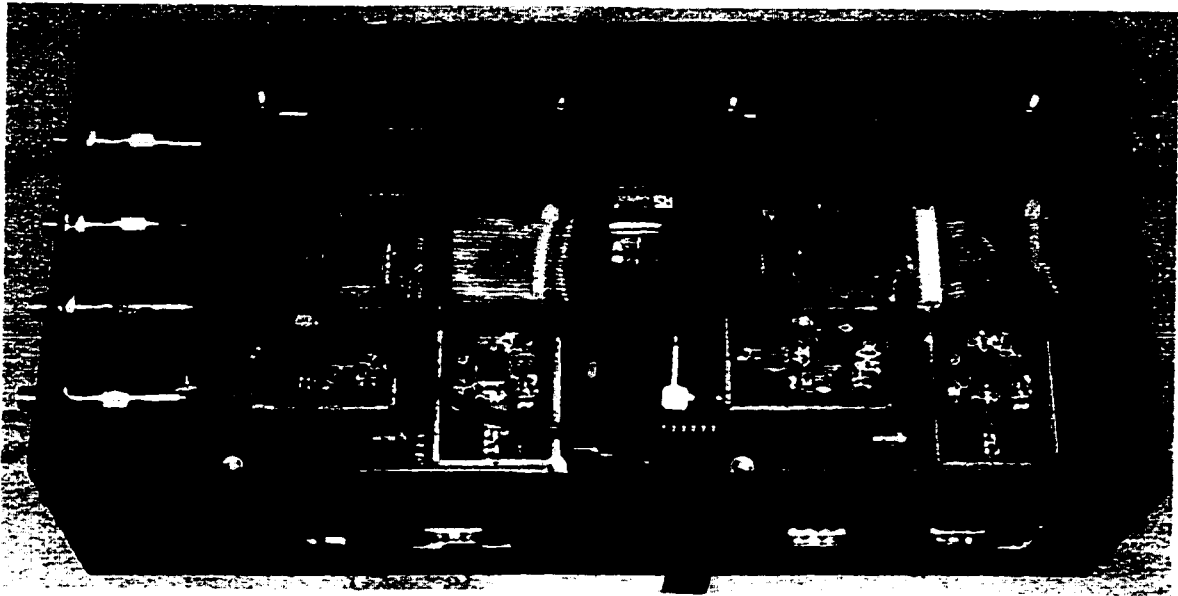


Fig. 3.4: Picture of the New GPS Receiver. There are Two Correlator Boards that each have 2 RF Front Ends. These Boards Run off the Same Clock Signal that is Generated on the Bottom Board. In this Configuration the Receiver has Four Antennas and 24 Channels, but the Design Can Easily be Extended by Adding More Cards.

on the blimp was routed through an RF splitter into each card. In this manner, each antenna on a blimp had eight dedicated receiver channels.

3.3 Software

A key benefit of using hardware based on the Mitel GPS chipset is that this provides access to the GPSBuilder Software (marketed as the “GPS Architect” Toolkit). This software is entirely written in C code. Complete access to the source code has allowed extensive modification to the following:

1. Code Phase and Carrier Phase Tracking Loops - A 3rd order phase-locked loop was added in order to measure the carrier-phase accurately.

2. **Signal Acquisition Routines** - The coarse acquisition loops were modified to improve performance during startup. This included a software select to command the receiver to track either pseudolites or NAVSTAR satellites, and to modify the loops accordingly. In particular, most of the pseudolite carrier signals did not have a data message modulated on them. This removed the half-cycle ambiguity [CC92], and allowed the phase discriminator to be more robustly determined. Additionally, the frequency search during start-up was toggled based on whether the signal was from a GPS satellite (which requires knowledge of the almanac for a warm start), or pseudolite (see item 5)
3. **Sampling Time Algorithm** - The measurements are latched in hardware, and are subject to drift relative to true time due to clock instabilities. Software was added to slew this latch time at 1 Hz to a common time standard (see Chapter 4), so that additional phase corrections were unnecessary when using the measurements from the different receivers in the system to form the state estimation.
4. **Cycle-Slip Detection Routines** - Software was added to detect cycle-slips and send a warning with the message data packet.
5. **Frequency Search Regions During Startup** - Software features to command the receiver to acquire the signal in specific frequency bins were added. The NCO (numerically controlled oscillator) on each channel was saved to non-volatile memory every 5 minutes, and downloaded into working memory at start-up. This allowed the receiver to rapidly acquire the pseudolite signal when first turned on, avoiding the frequency search required during a cold start.

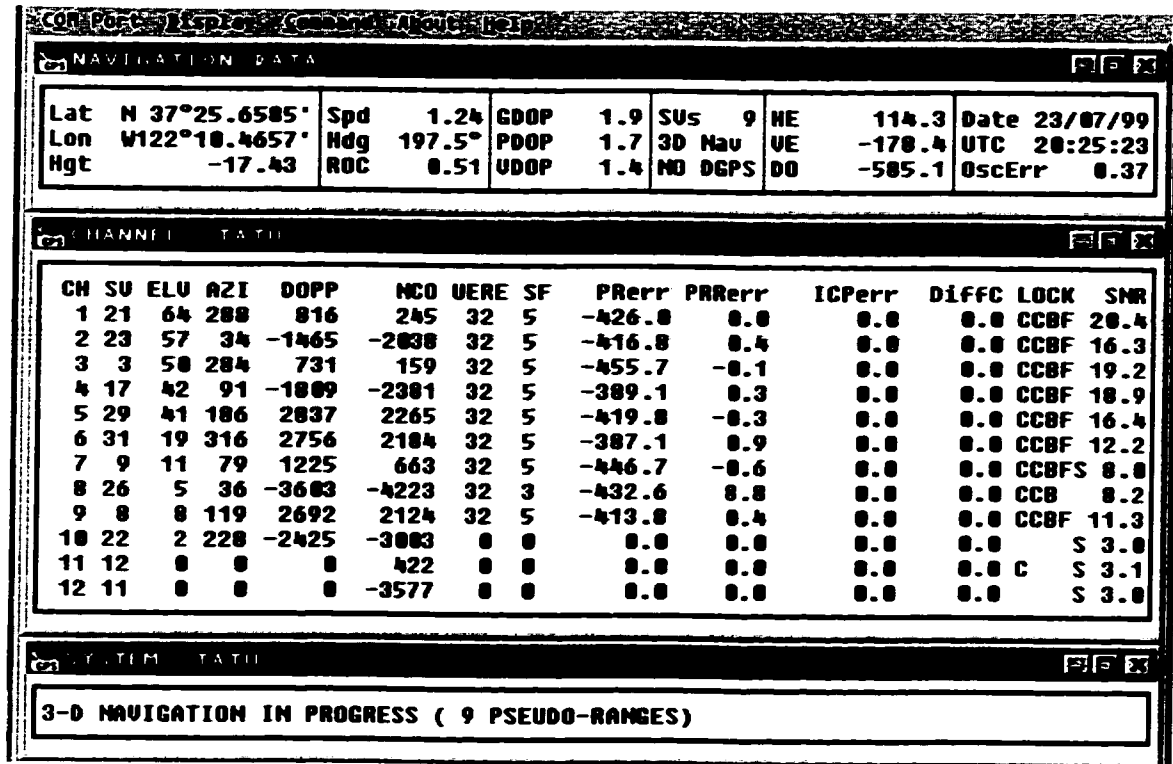


Fig. 3.5: Screenshot of the Basic Receiver Display Interface

- Input/Output Routines - A new message protocol was developed, and incorporated into the receiver software. Several new receiver commands were created.

The GPS Architect toolkit provides a basic software package called WinmonTM that interfaces to the correlator cards. The source code for this software was also made available by Mitel, and was modified for use in the testbed. Figure 3.5 shows a screenshot of the basic Winmon display that is used to present information sent from the correlator cards. This basic display software was also ported over to the real-time operating system for use during the testbed operations. Visible in the display are the satellites (or pseudolite) being tracked (“SV”), the effective doppler (“DOPP”), tracking status (“Lock”), and SNR value among other key pieces of information. The

display that runs on the real-time system also shows the measurement time-stamp, and integrated carrier-phase.

The receiver nominally operates in a “ground mode”, which results in the minimal set of data (see Chapter 2) being sent at 10 Hz for use by the estimator. However, the message protocol used when this display is selected sends over quite a bit more information, which provides a valuable tool in the system development and debugging.

3.4 Hardware Testing

Several tests were performed to determine the carrier-phase noise characteristics of the completed receiver (Figure 3.4). This was especially important in light of the redesign of the correlator card which required moving the onboard oscillator, and running new electrical traces throughout the board. Additionally, the clock signal being routed from the interface board is subject to noise since it is being sent through two SMA connectors as well as coax cabling. Therefore, several tests needed to be made in order to see if these modifications influenced the performance in a significant way.

Four tests were performed to measure the noise characteristics of the new attitude receiver. The integrated differential carrier-phase (DCP) between various combinations of the front ends were measured for the zero-baseline (the signal from a single antenna was routed through a splitter to each front end) case. The tests were:

1. Static Antenna Case - Inside the highbay
2. Dynamic Antenna Case - Inside the highbay
3. Static Antenna Case - Outside
4. Dynamic Antenna Case - Outside

Ideally, the integrated DCP difference between the front ends will be zero for the zero-baseline case. This, of course, must also be true outside even when the LOS to the NAVSTAR satellites changes over time. The purpose of the tests were:

1. The static antenna case inside the highbay provides the best measure of the raw RF noise characteristics. This is because the impact of the tracking loop dynamics (which will effect the measured DCP) are minimized. This is especially so inside the highbay, because the measured doppler to each pseudolite is driven by their clock stabilities. The measured doppler to the NAVSTAR satellites is quite a bit higher due to the satellite dynamics.
2. The indoor dynamic antenna case gives a measure of the total receiver noise in a high multipath environment (see Chapter 2). The effective noise will be driven by the RF noise, the dynamics of the tracking loops, and the impact of the multipath on the power levels of the signal.
3. The outdoor tests provide a measure of the performance in a low multipath environment.

Figure 3.6 shows a plot of the DCP values between the signal being routed through three different RF front end combinations for the stationary receive antenna case. In all cases, data were collected for approximately 2.5 minutes at 1 Hz. Case S1 is between the signal on the *same* front end, but different *channels* on the same correlator board. S2 is between different RF front ends on the same board, and the S3 is for front ends on different correlator cards. Figure 3.7 shows plots for the DCP value between the same combinations of front ends (labeled D1,D2,and D3) for the case of a moving antenna. Both figures are for an antenna inside the highbay. Note that these graphs have quite different vertical scales.

The DCP error between the signal on the same front end, but different channels (S1, D1) is effectively 0, except for jumps of ≈ 0.7 mm visible in the plot. This is a

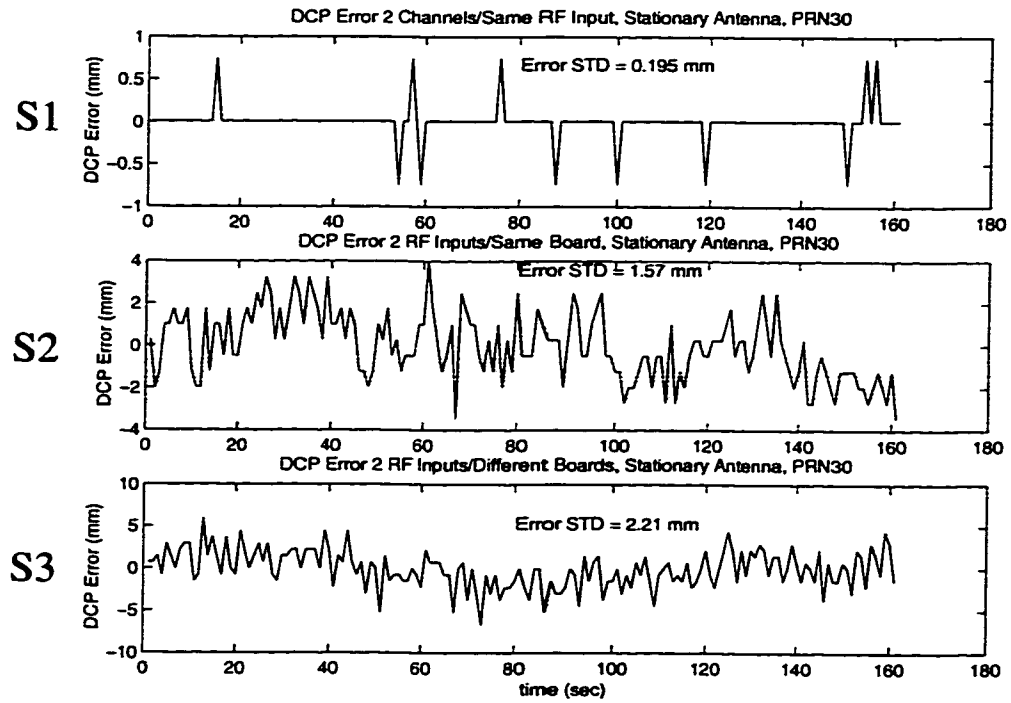


Fig. 3.6: Static Tests Across All Receiver RF Baselines - Indoor Case.

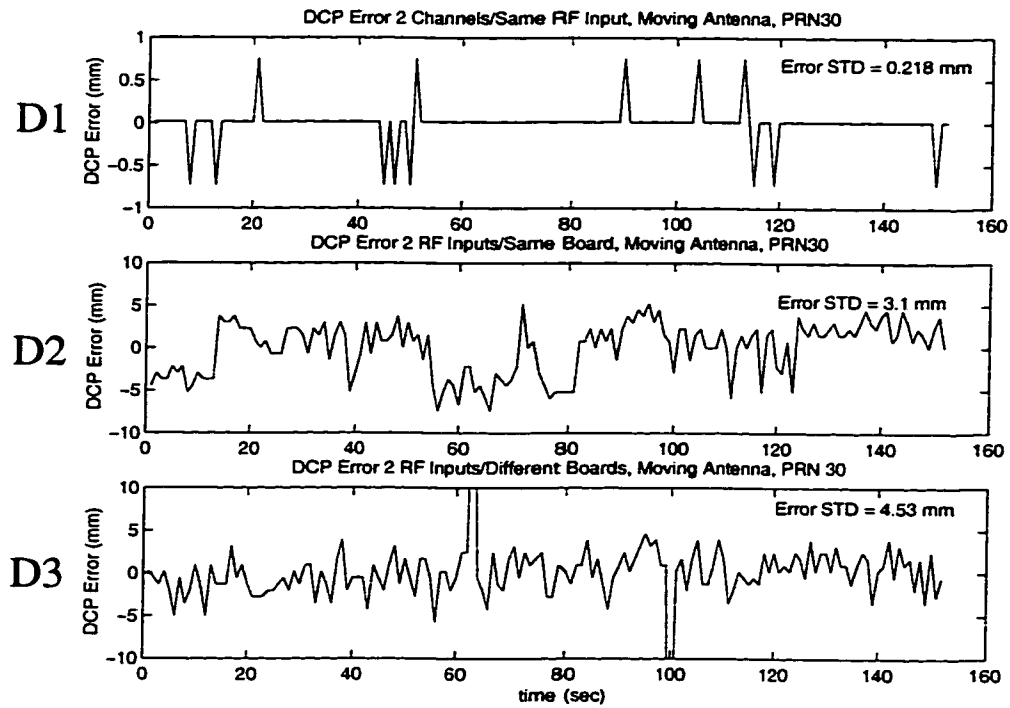


Fig. 3.7: Dynamic Tests Across All Receiver RF Baselines - Indoor Case.

result of the quantization of the carrier-phase signal. The carrier-phase wavelength is 19.06 cm long, and is being sent from the receiver with a resolution of 1 *Byte* ($190.6 \text{ mm}/2^8 \approx 0.7 \text{ mm}$). Because each channel is seeing the exact same digital signal after being sampled in the RF front end, the only error in this case is due to rounding.

Visible in the data set for the case using the signal from two different correlator cards, and using a moving antenna (D3) are two jumps of approximately 2 cm. These were actually cycle slips that were removed during post-processing. Note that this is reasonable, since this test is designed to measure the phase-noise, and these slips would be detected and eliminated for the estimation. The cycle slips are a result of the rapid antenna movement, and the multipath effects that make tracking indoors a challenge. Cycle slips occur significantly more often inside then outside because of the very complex RF environment.

Table 3.2: Error STD (mm) for Zero-Baseline DCP Tests - Indoors

RF front end pair	Stationary Antenna	Moving Antenna
Same front end, different channel	0.20	0.22
Different front end, same card	1.57	3.10
Different front end, different card	2.21	4.53

Table 3.3: Error STD (mm) for Zero-Baseline DCP Tests - Outdoors

RF front end pair	Stationary Antenna	Moving Antenna
Same front end, different channel	0.19	0.20
Different front end, same card	3.19	3.46
Different front end, different card	2.63	2.89

The results are summarized in Tables 3.2 and 3.3. The tests indicate that the phase-noise is very small ($< 0.5 \text{ cm}$), and is comparable to typical commercial receivers [GPS96]. The phase noise for the outside, static antenna case was slightly

higher as compared to the inside, static antenna case (across different front ends) due to the dynamics of the NAVSTAR constellation. When the same front end (but different channels) are compared, the only error visible is a result of rounding errors (for both the inside and outside case), since the same digitized signal is sent to both channels. The noise for the dynamic cases (D2,D3, and corresponding outside tests) increased slightly from the static cases (S2,S3, and corresponding outside tests) due to the impact of the tracking loop dynamics. Of particular note is that the phase noise increased only slightly from the static case to the dynamic case for the outside tests as compared to the indoor tests. This is a result of the fact that multipath is much worse indoors, as discussed in Chapter 2.

All of the results are slightly dependent on the measured SNR at each front end. The phase noise across front end sections on different boards was less than the case of front end sections on the same board for the outside case because of the signal SNRs. However, the impact of the SNR only becomes significant when it drops to very low levels (2-3 db above the GPS detection threshold).

The DCP was subject to some drift as a result of thermal gradients inside the box prior to placement of the PC fan. This drift was on the order of 2 cm as the correlator boards heated up at different rates. The phase *bias* contribution due to the length of coax cable through which the external clock signal is routed can be resolved by using a floating point bias, as was done in our testbed, or it can be included in the line bias.

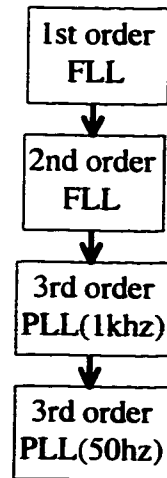


Fig. 3.8: Carrier-Phase Tracking Loops

3.5 The Carrier Tracking Loops

The carrier tracking code contained in the *GPS Architect* software was modified to improve the tracking performance in the receiver. The bandwidth of the coarse acquisition loops (frequency locked loops) were modified, and a phase-locked loop (PLL) was added to allow accurate phase measurements to be made.

Figure 3.8 shows the basic hierarchal control scheme used to track the GPS carrier-phase. The 1st order frequency locked-loop (FLL) is used to reduce the frequency error from as much as 500 Hz down to approximately 10 Hz. The 2nd order FLL then reduces it down to a few Hz, where the PLLs are then employed. The original tracking loops only employed the FLLs, and did not use a PLL. This resulted in the tracking loops being closed around the carrier rate error instead of the carrier phase error. This caused the measured carrier-phase to drift over time, which resulted in an error when forming the DCP.

The GPS signal has a 50 Hz navigation message modulated on it, so it is first necessary to determine where the data bit transition occurs in order to run the PLL

at anything less than 1 kHz. If this transition is not determined accurately, the software integrated in-phase and quadrature correlation measurements will be in error, subsequently destabilizing the loop. The PLL is first closed at 1 kHz until the data transition is detected, at which point the loops are then closed at 50 Hz. There are two advantages to running the tracking loops at 50 Hz. The first is that this results in significantly less load on the processor, freeing up CPU cycles for other activities. Additionally, the software integrated correlation measurements provide a more reliable measure of the phase error at the bandwidths involved. This is especially important in the indoor environment as will be discussed in a later section.

The time and measurement update equations for a 3rd order tracking loop [CC92] are

$$\begin{bmatrix} \bar{\phi} \\ \dot{\bar{\phi}} \\ \ddot{\bar{\phi}} \end{bmatrix}_{k+1} = \begin{bmatrix} 1 & T & \frac{1}{2}T^2 \\ 0 & 1 & T \\ 0 & 0 & 1 \end{bmatrix} \begin{bmatrix} \hat{\phi} \\ \dot{\hat{\phi}} \\ \ddot{\hat{\phi}} \end{bmatrix}_k \quad \text{Propagation} \quad (3.1)$$

$$\begin{bmatrix} \hat{\phi} \\ \dot{\hat{\phi}} \\ \ddot{\hat{\phi}} \end{bmatrix}_k = \begin{bmatrix} \bar{\phi} \\ \dot{\bar{\phi}} \\ \ddot{\bar{\phi}} \end{bmatrix}_k + \begin{bmatrix} L_1 \\ L_2 \\ L_3 \end{bmatrix} \Delta\phi_k \quad \text{Measurement Update} \quad (3.2)$$

where the states are the phase, phase rate, and phase acceleration. The PLL gain is governed by the L_i 's.

The phase error, $\Delta\phi_k$, is derived from the in-phase, I_k , and quadrature, Q_k , correlation values which are latched in the receiver hardware at 1 kHz (they are integrated in software when the loops are closed at 50 Hz). This value is computed

as

$$\Delta\phi_k = \arctan2(Q_k, I_k) \quad (3.3)$$

and is implemented as a look-up table in the receiver software.

The NCO provides a direct measure of the carrier-phase replica frequency, and is therefor modeled as a first order system $\phi_{k+1} = \phi_k + T\mu_k$.

If the NCO state is the phase estimate, $\bar{\phi}_k$, then

$$T\mu_k = \bar{\phi}_{k+1} - \bar{\phi}_k \quad (3.4)$$

$$= \hat{\phi}_k + T\dot{\hat{\phi}}_k + \frac{1}{2}T^2\ddot{\hat{\phi}}_k - \bar{\phi}_k \quad (3.5)$$

$$= \bar{\phi}_k + L_1\Delta\phi_k + T\dot{\hat{\phi}}_k + \frac{1}{2}T^2\ddot{\hat{\phi}}_k - \bar{\phi}_k \quad (3.6)$$

$$\mu_k = \dot{\hat{\phi}} + \frac{1}{2}T\ddot{\hat{\phi}} + \frac{L_1}{T}\Delta\phi_k \quad (3.7)$$

hence the resulting system is given by the equations

$$\begin{bmatrix} \dot{\bar{\phi}} \\ \ddot{\bar{\phi}} \end{bmatrix}_{k+1} = \begin{bmatrix} 1 & T \\ 0 & 1 \end{bmatrix} \begin{bmatrix} \dot{\hat{\phi}} \\ \ddot{\hat{\phi}} \end{bmatrix}_k \quad (3.8)$$

$$\begin{bmatrix} \dot{\hat{\phi}} \\ \ddot{\hat{\phi}} \end{bmatrix}_k = \begin{bmatrix} \dot{\bar{\phi}} \\ \ddot{\bar{\phi}} \end{bmatrix}_k + \begin{bmatrix} L_2 \\ L_3 \end{bmatrix} \Delta\phi_k \quad (3.9)$$

$$\mu_k = \dot{\hat{\phi}} + \frac{1}{2}T\ddot{\hat{\phi}} + \frac{L_1}{T}\Delta\phi_k \quad (3.10)$$

The reduced order system is used in the tracking loop, and only the phase rate and phase acceleration need to be stored in memory and propagated.

The tracking loops on most receivers are closed at 1 KHz, since the hardware *integrate and dump* is synchronized with the C/A code epoch (which has a period

of 1 ms). However, it was found that the performance was more robust inside the highbay when the tracking loops are closed at 50 Hz (Section 3.6.1).

Note that the actual selection of the gains is complicated by the fact that the multipath inside the highbay is effectively a colored noise source that is very difficult to model accurately. Some trial and error was required to obtain an adequate set of gains. The choice of $L_1 = 0.49$, $L_2 = 8.38$, and $L_3 = 71.04$ (when the loops are closed at 50 Hz) resulted in good performance with this receiver. Gains of $L_1 = 0.088$, $L_2 = 4.12$, and $L_3 = 95.47$ were used when the loops were closed at 1 kHz. These were implemented with binary shifts within the tracking loop code. The gain selection for operation outside is typically simpler, because multipath is reduced and bandwidth requirements dominate the gain selection. For our receiver, the same gains resulted in good performance both inside and outside.

3.6 GPS Signal Tracking

3.6.1 Integrity

Figure 2.5 shows a plot of the received SNR in the receiver, both for a maneuver outside with the NAVSTAR constellation, and inside using the pseudo-constellation. As discussed earlier, the multipath interference pattern inside results in rapid power fluctuations, making tracking difficult. Both cases in the figure used a software *integrate and dump* of 20 ms, corresponding to closing the tracking loops at 50 Hz. When the tracking loops are closed at 1 KHz, the large SNR drops indoors (which occur quite frequently, but over short time scales, *i.e.*, approximately a few milliseconds) destabilize the loops. Performing a software integrate and dump over longer periods provides a more reliable measure of the phase error, and helps robustify the tracking

loops to these problems. Further improvement in tracking performance was achieved using the knowledge of the instantaneous SNR value. When the SNR drops below some threshold (nominally the minimum GPS detection level), then the estimator should only perform the time update, and not perform the measurement update for that epoch. This allows the receiver to successfully “coast” through the brief signal drop outs associated with multipath. Figure 2.5 demonstrates that the GPS signal suffers through momentary drops in power, but the signal continues to be tracked throughout the maneuver, indicated by the fact the SNR quickly recovers. It is possible that the measurement corresponding to any epoch where there is a significant power drop can suffer a cycle slip, but this measurement can be easily dropped, temporarily, from the estimation. These results are relevant to any environment since the SNR to low elevation satellites starts to approach the minimum detectable level.

3.6.2 Cycle Slip Detection

A complicating factor in the formation state estimation is the presence of carrier-phase “cycle slips”. In effect, the phase replica internal to the receiver hardware slips past the incoming signal, resulting in the measured phase being off by integer numbers of $1/2$ wavelengths (or whole wavelengths when there is no data modulated on the carrier, as is the case with some of the pseudolites). These are measurement errors that will cause the state estimation to be incorrect if not accounted for.

Cycle-slips are a problem when the SNR becomes too low, as will happen with regularity indoors when the receive antennas move about the room. It also happens outside when the vehicles are in view of low elevation satellites, whether the vehicles are on Earth, or in-orbit. These power drops will also occur outside as the vehicle moves about, since the observed elevation angle is a function of the vehicle attitude.

Several tests were performed to insure that the differential carrier phase could be reliably determined. A cycle-slip flag was added to the receiver software which was generated based on the *instantaneous* measured SNR. Whenever the received SNR dropped below a specified threshold, the slip flag was set internal to the receiver and sent out in the data message. Whenever a measurement was flagged as invalid, it was discarded and not used by the estimator.

A phase predictor can also be used to check for the presence of cycle-slips, or unexpected phase changes that can accompany a signal with a large multipath component. The phase predictor fits a 2nd order polynomial to the integrated differential carrier-phase, whether its formed from single differences for the intra-vehicle measurements, or from double differences for the inter-vehicle measurements. Using these measurements eliminates any effect due to the clock bias, as is explained in Chapter 4.

The 2nd order phase predictor has the general form:

$$\phi_{pred} = \sum_{i=0}^2 \bar{a}_i t^i \quad (3.11)$$

The predictor coefficients, \bar{a}_i , can be formed as follows.

Define A as

$$A = \begin{bmatrix} 1 & t_0 & t_0^2 \\ 1 & t_1 & t_1^2 \\ \vdots & \vdots & \vdots \\ 1 & t_{n-1} & t_{n-1}^2 \end{bmatrix} \quad (3.12)$$

where t_0, t_1, \dots, t_{n-1} are the sample times the differential carrier-phase data was collected, and n is the number of data points chosen to develop the predictor.

Only three points are actually required to solve for the coefficients, since the phase is being modeled as 2nd order (this accurately models the phase acceleration visible due to vehicle accelerations, and clock instabilities). However, better accuracy may be achieved by using several additional points. The predictor coefficients are then solved for in a weighted least square sense as:

$$\bar{a} = (A^T W A)^{-1} A^T W \Phi \quad (3.13)$$

where

W = weighting matrix

Φ = vector of measured integrated differential phases

The weighting, W , is an $n \times n$ matrix defined as:

$$W = \text{diag}(1.0, 1.0, 1.0, 1 - \alpha, \dots, 1 - (n - 3)\alpha) \quad (3.14)$$

where α is a user selectable parameter that varies the weighting on the points. Choosing $\alpha > 0$ effectively de-weights the older points relative to the more recent data collected. It is assumed that less than 13 points are used, so that $W > 0$.

The cycle slip flag is set when the prediction error exceeds some threshold

$$\left| \Phi_n - (\bar{a}_1 + \bar{a}_2 t_n + \bar{a}_2 t_n^2) \right| > \text{Error}_{max} \quad (3.15)$$

where

t_n = time of prediction

Φ_n = measured phase at time t_n

Error_{\max} = prediction error threshold (nominally set to 1/2 of the carrier-phase wavelength)

Large prediction errors indicate that the most recent measurement is corrupted, and should be discarded. The measurements from that transmitter can be incorporated into the state estimation at a later time, once confidence in the measurement has been restored. Thus, the total number of measurements being used to perform the state estimate can vary from epoch to epoch as measurements are brought on/off-line.

Note that the accuracy of this prediction is dependent on the dynamics of the vehicles, as well as the sample rate. The sample rate must be sufficiently fast in order to accurately model the phase with a 2nd order polynomial over short time periods. For the relative position double differences, the bound on the maximum sample period, t_s , can be simply related to the maximum vehicle jerk and L_1 wavelength as $t_s \ll (\lambda_{L_1}/\text{jerk}_{\max})^{1/3}$. For the intra-vehicle single differences, the bound on the maximum sample period can be related to the vehicle rotation rate, ω , and antenna baseline length, b , as $t_s \ll (\lambda_{L_1}/(b\ddot{\omega}_{\max}))^{1/3}$. As with any prediction, the farther into the future it is made, the more unreliable it will become.

The receiver used on the testbed latches measurements at 10 Hz, which is sufficient for many applications, including the blimps and space vehicles. The attitude software on the receiver uses single differences formed between the antennas connected to the receiver, and these can be used by a phase predictor incorporated directly into the receiver software.

Table 3.4: Prediction Error STD (cm)

Number of points	4	5	6	7	8
Error(STD)	3.8	3.6	3.5	3.2	3.2

As mentioned above, the accuracy of the predictor is dependent on the number of points used to solve for the coefficients. The minimum number is three, but depending on the dynamics and sample rate, additional points will improve the accuracy. The number of data points used for the tests shown in Figure 3.9 were varied from 4-8. For the formation flying testbed, the sample rate was set at 10 Hz, and the phase predictions were made 0.1 seconds into the future. The resulting prediction error standard deviations for that data, using $\alpha = 0.1$, are summarized in table 3.4. The accuracy improved with the number of points until seven were used, which would be the final value selected for this data. However, the performance is not significantly effected by the number of points, and anywhere from 5-8 can be used in the receiver software.

Figure 3.9 shows a plot of differential carrier phase between two antennas, one fixed, and one moving across the highbay workspace. The moving antenna starts and stops at the same location. Hence, the initial and final values of differential carrier phase would be identical if the signal was tracked during the entire maneuver without the presence of a cycle slip (accounting for the small DCP error that will be present, since its not possible to move the antenna back to the exact same spot). For the plots shown, the bias was subtracted such that the differential carrier phase was 0 at t_0 . The figure shows the correlation that is present between momentary SNR dips (indicated by an 'x') and large phase prediction errors (indicated by an 'o'). Note that the differential phase for PRN 11 was corrupted by a cycle slip, which is easily visible at $t \cong 9$ sec. This was accompanied by a large prediction error and a power drop. There was another set of prediction errors/power dips at $t \cong 32$ sec. Although there does not appear to be a cycle slip at this point, the measurements at that time suffered from a large multipath disturbance. Using the phase prediction error, in

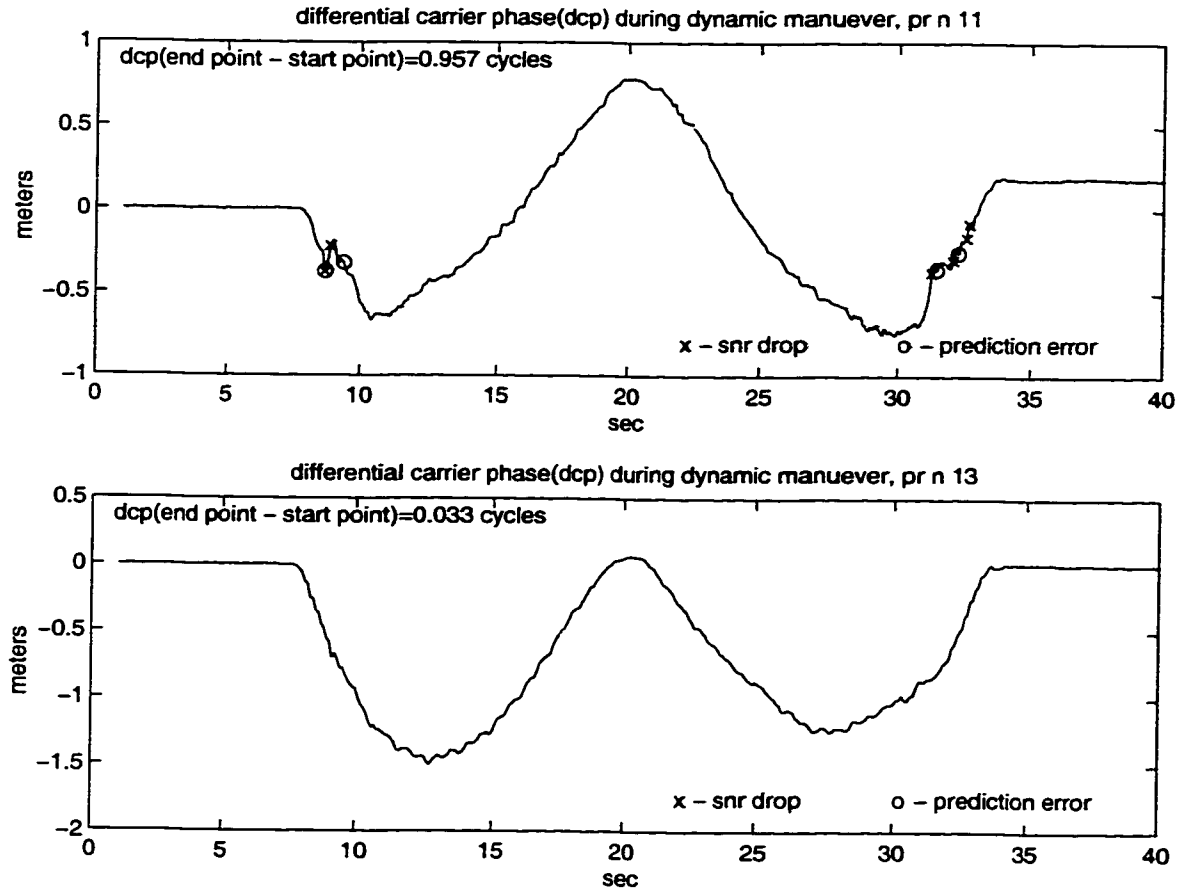


Fig. 3.9: Differential Carrier-Phase Plot Between Two Antennas Showing the Cycle Slip Detection Algorithms. There is a Suspected Cycle Slip at $t \cong 9$ sec. SNR Dips are Indicated by 'x' and Large Phase Prediction Errors are Indicated by 'o'. Note that there are no Cycle Slips in the Lower Plot for PRN 13.

conjunction with a knowledge of the instantaneous SNR, the invalid measurements can be more reliably detected and eliminated before performing the state estimation. In the event a valid measurement is flagged as invalid, it will also be dropped from the estimation. However, this should not present a major problem as the number of satellites visible is generally far more than the minimum required to perform the estimation [JCA99].

~

Chapter 4

Formation State Estimation

This chapter discusses the state estimation problem for both the general formation flying application and the blimp testbed. This includes a discussion of the coordinate systems and the GPS measurements. Two issues related to the GPS measurements are presented: the far constellation approximation, and the sample time error. Finally, the formation measurement equations are given, and the general solution to the estimation problem is described.

4.1 Coordinate Systems

Figure 4.1 shows the coordinate systems used for positioning in a formation flying cluster of vehicles. In principal, there are two separate systems specified. The first system, denoted by the unit triad (X_I, Y_I, Z_I) is used to indicate the position of the formation in some absolute sense. This frame will generally be fixed to the Earth, although whether it is a local East-North-Up (ENU) frame, or an Earth-Centered-Earth-Fixed (ECEF) frame is application dependent. The vector X_F specifies the position of the formation coordinate frame in the inertial frame. The “absolute”

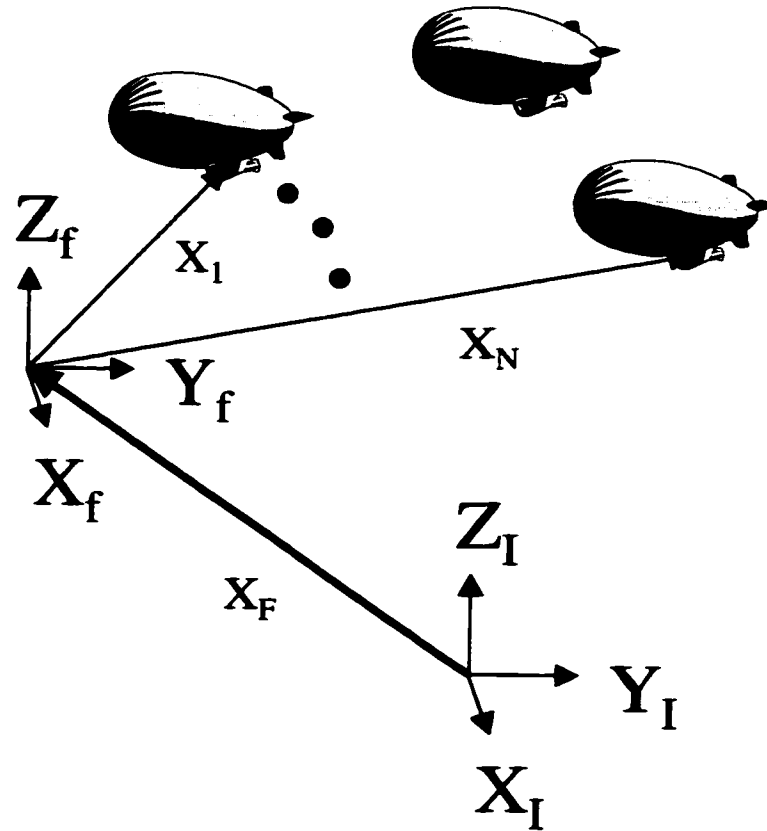


Fig. 4.1: Coordinate System for Formation.

formation location would, in general, not be developed using differential carrier-phase measurements, but instead would use standard pseudoranging techniques [GPS96]. This will result in a relatively coarse position estimate (100 m single-point accuracy with SA on). This could be improved using differential code measurements, such as those available from WAAS or other beacons [GPS96]. However, the absolute position is not of critical importance for the formation flying application because the relative positions determine how the vehicles interact with one another.

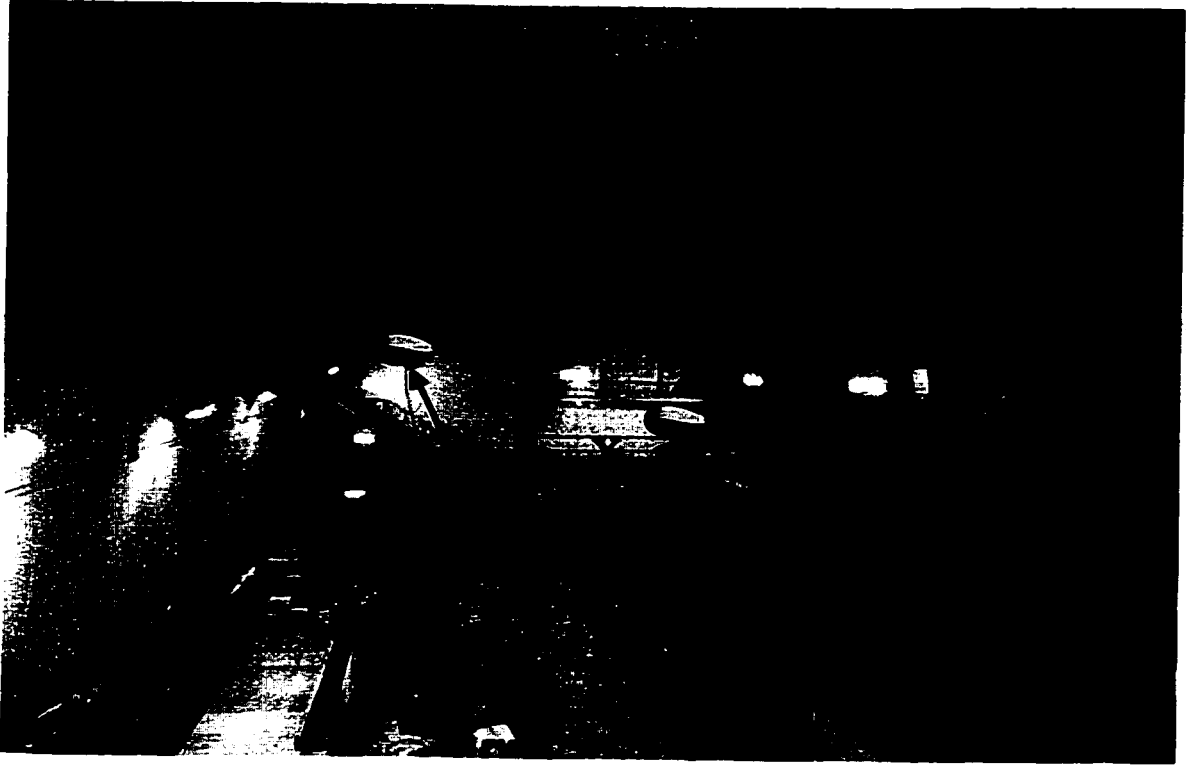


Fig. 4.2: Highbay Coordinate System.

Figure 4.1 also indicates the coordinate system used to specify the relative vehicle positions. This coordinate frame is effectively attached to the cluster of vehicles, and is given by the unit triad (X_f, Y_f, Z_f) . The formation state estimates used to specify the relative vehicle locations will be derived from differential carrier-phase measurements. The accuracy of the relative position states will then be in the 2–10 cm range, depending on the position dilution of precision (PDOP) [GPS96]. However, before differential carrier-phase measurements can be used, the carrier-phase biases must be solved for, which is discussed in greater detail in Chapter 5.

The coordinate systems specified in Figure 4.1 are for the general problem, wherein the cluster is outside, or in-orbit about the Earth. However, the blimp testbed operates primarily inside the highbay, and for the indoor flights a single coordinate system

was specified. Figure 4.2 shows the coordinate system used for the blimp testbed. The system is attached to the floor of the highbay, with the origin located at a brass plate permanently fixed to the floor. The blimp position vectors, X_1 , and X_2 are then specified absolutely in the building with respect to (X_f, Y_f, Z_f) .

4.2 GPS Measurements

4.2.1 Carrier-Phase Measurements

The GPS carrier-phase observable at antenna j of vehicle i (the antenna is at an arbitrary location on the vehicle) from transmitter k is given by:

$$\phi_{ijk} = |P_{ijk}| + \tau_{vi} + \tau_{tk} + l_{ijk} + l_{tk} + \lambda K_{ijk} + \nu_{ijk} + E_{ijk} \quad (4.1)$$

where

- ϕ_{ijk} = measured carrier phase at antenna j of vehicle i from transmitter k
- $|P_{ijk}|$ = distance from antenna j of vehicle i to transmitter k
- τ_{vi} = clock bias for receiver i
- τ_{tk} = clock bias for transmitter k
- λK_{ijk} = carrier-phase bias for measured phase at antenna j of vehicle i from transmitter k
- l_{ijk} = line bias from antenna j of vehicle i to the onboard receiver
- l_{tk} = line bias from satellite transmitter antenna to signal generator
- ν_{ijk} = receiver noise for the signal being tracked on antenna j of vehicle i from transmitter k

E_{ijk} = other error sources (i.e. Ionosphere, Troposphere, Ephemeris, Polarization, etc.)

4.2.2 Single Difference Carrier-Phase Measurements (Same Receiver)

The carrier-phase measurements from two separate antennas can be differenced in order to eliminate many of the common mode terms. When differencing measurements from antennas on the same receiver, the differential phase is:

$$\Delta\phi_{ijgk} = |P_{ijk}| - |P_{igk}| + l_{ijk} - l_{igk} + \lambda K_{ijgk} + \nu_{ijgk} \quad (4.2)$$

where

$\Delta\phi_{ijgk}$ = differential phase between antennas j , and g on vehicle i , using transmitter k

λK_{ijgk} = integer ambiguity for differential phase measurement between antennas j , and g on vehicle i , using transmitter k

The error source measurement term, E_{ijk} , was assumed to be a common mode component which was eliminated when the difference was made. However, this is not strictly true, as the effects due to polarization will vary from antenna to antenna if they are non-aligned [JCA298].

4.2.3 Single Difference Carrier-Phase Measurements (Different Receivers)

When differencing measurements from antennas on different receivers, the differential phase is:

$$\Delta\phi_{ijdgk} = |P_{ijk}| - |P_{dgk}| + l_{ijk} - l_{dgk} + \lambda K_{ijdgk} + \nu_{ijdgk} + \tau_{vi} - \tau_{vd} \quad (4.3)$$

where

$\Delta\phi_{ijdgk}$ = differential phase between antennas j on vehicle i , and g on vehicle d , using transmitter k

λK_{ijdgk} = integer ambiguity for differential phase measurement between antennas j on vehicle i , and g on vehicle d , using transmitter k

Note that the receiver clock bias terms are present in Eq. 4.3 because separate receivers are being used. Eq. 4.2 does not have a component due to the clock error as that difference was formed with the same receiver. Similar to Eq. 4.3, the error source term was assumed to be common mode. This will be the case for vehicles which are close together (a few km), so that the spatial decorrelation between the error terms associated with Ionosphere, Troposphere, Ephemeris, etc are negligible. Phase correction terms would need to be included for vehicles separated by large distances to account for the spatial decorrelation. There will be a component due to polarization which should be accounted for under general vehicle motions. This will be addressed in Chapter 6.

4.2.4 Double Difference Carrier-Phase Measurements

One method to account for the clock bias terms in Eq. 4.3 is to use double differences. In effect, two single differences measurements (using different transmitters) are themselves differenced. When the double difference is formed by using the measurements from the same two antennas, this will eliminate the line bias terms, as well as the clock bias terms when formed across different receivers.

The double difference measurement across two different receivers, using the same two antennas is given by:

$$\nabla \Delta \phi_{ijdgkl} = |P_{ijk}| - |P_{djk}| - |P_{ijl}| + |P_{djl}| + \lambda K_{ijdgkl} + \nu_{ijdgkl} \quad (4.4)$$

where

$$\begin{aligned} \nabla \Delta \phi_{ijdgkl} &= \text{double difference between antennas } j \text{ on vehicle } i, \\ &\quad \text{and } g \text{ on vehicle } d, \text{ using transmitter } k, \text{ and } l \\ \lambda K_{ijdgkl} &= \text{inter ambiguity for double difference between an-} \\ &\quad \text{tennas } j \text{ on vehicle } i, \text{ and } g \text{ on vehicle } d, \text{ using} \\ &\quad \text{transmitter } k, \text{ and } l \end{aligned}$$

4.3 Far Constellation Approximation

The signal generated by the transmitter will radiate away from the transmit antenna in a spherical wavefront as shown in Figure 4.3. An approximation to the differential carrier-phase measurements can be made when the transmitters are far away, as will be the case for any system which is using the NAVSTAR constellation.

Figure 4.3 shows the GPS transmitter and two antennas at which carrier-phase measurements are made. Assuming the clock bias is zero (as will be the case if the

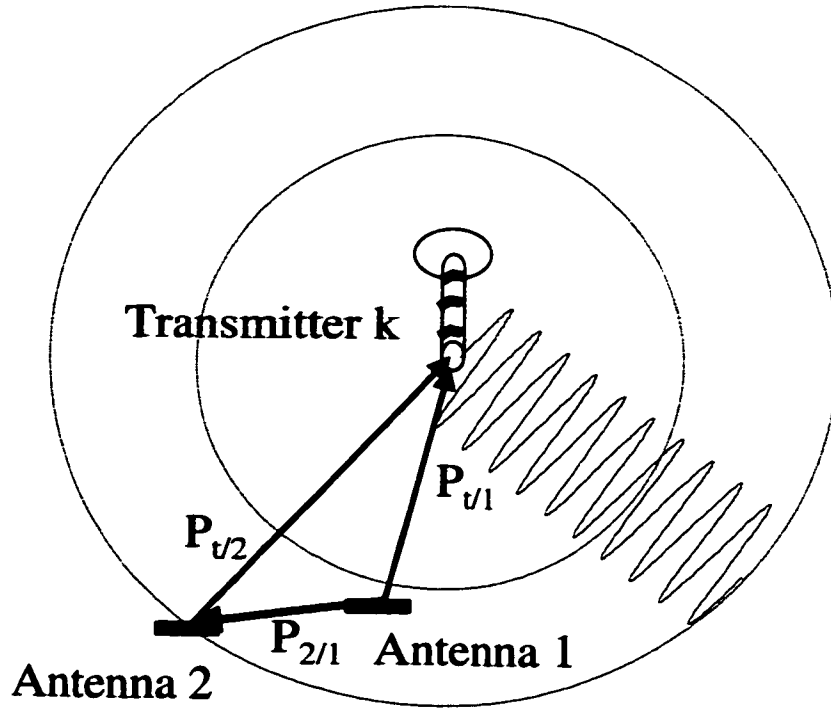


Fig. 4.3: Spherical Wavefronts of Transmitted GPS Signal

antennas are connected to the same receiver), the differential phase between antennas 1, and 2 from the transmitter is given by:

$$\Delta\phi = |P_{t/1}| - |P_{t/2}| + \beta + \nu \quad (4.5)$$

where

$P_{t/1}$ = position vector from antenna 1 to the transmitter

$P_{t/2}$ = position vector from antenna 2 to the transmitter

The distance function may be approximated by:

$$|P_{t/2}| - |P_{t/1}| \approx -P_{2/1} \cdot e_k \quad (4.6)$$

where $P_{2/1}$ is the position vector from antenna 1 to antenna 2, and

$$e_k = (P_{t/2} + P_{t/1}) / |P_{t/2} + P_{t/1}| \quad (4.7)$$

This linearized differential-carrier phase approximation is valid when

$$\frac{|P_{2/1}|^2}{2|P_{t/1}|} < \text{Error}_{max} \quad (4.8)$$

where Error_{max} is the magnitude of the receiver phase noise [HT97].

4.4 Sample Time Error

Eqs. 4.3, and 4.4 are created by differencing phase measurements between antennas on *different* receivers. Implicit in these equations is that the phases are latched in hardware at identical times. However, since separate receivers are being used, this is not the case, and there will be a phase error component that needs to be accounted for.

Consider Eq. 4.3, which is the single difference carrier-phase measurement between two separate receivers. The phases will, in general, be latched at different times on each receiver, designated by t , and t_0 . The differential phase is then given by

$$\Delta\phi_{ijdgk}(t, t_0) = \phi_{ijk}(t) - \phi_{dgk}(t_0) \quad (4.9)$$

In order to perform the state estimation, the differential phase needs to be corrected such that the phases at each receiver are aligned to the same time. The phase at time

t may be related to that at time t_0 by

$$\phi_{ijk}(t_0) = \phi_{ijk}(t) - \int_{t_0}^t \dot{\phi}_{ijk} dt \quad (4.10)$$

The differential phase with measurements aligned to t_0 may then be written as:

$$\Delta\phi_{ijdgk}(t_0, t_0) = \Delta\phi_{ijdgk}(t, t_0) - \int_{t_0}^t \dot{\phi}_{ijk} dt \quad (4.11)$$

which to first order may be expressed as

$$\Delta\phi_{ijdgk}(t_0, t_0) = \Delta\phi_{ijdgk}(t, t_0) - \dot{\phi}_{ijk}(t)\Delta t \quad (4.12)$$

where Δt is the sample time error between the two receivers, and

$$t = t_0 + \Delta t \quad (4.13)$$

Zimmerman estimated the phase rate, $\dot{\phi}_{ijk}(t)$, using a finite difference made from the phase measurements latched at t , and $t - t_s$, where t_s is the sample rate of the receiver. [KZ96]. However, the finite difference estimate will be subject to large errors depending on the system dynamics, and clock stabilities. An improved estimate should be obtained from the carrier phase tracking loops, which maintains a precise estimate of the phase rate at any given moment.

An alternative to extrapolating the phases is to continuously slew the latch time in hardware to a common time standard on all the receivers in the system. The software on the attitude receiver used in the blimp testbed was modified to do this at 1 Hz. The time standard when sufficient visibility to the NAVSTAR constellation is present (as when operating outside) is true GPS time. When operating in the highbay, this

time standard is generated from the navigation message on an arbitrarily designated pseudolite.

Immediately after the hardware slew, the receiver latch times will be aligned to better than 100 ns, which accounts for the pseudorange error, and the slight clock drift that will be observed just prior to the hardware latch. The same level of accuracy is obtained inside the highbay, since the difference in the signal time-of-flights to each of the blimps is small (< 30 ns).

The maximum observed doppler to the NAVSTAR satellites is on the order of 10 KHz for terrestrial applications, and 60 KHz while in orbit [GL97]. The maximum observed doppler to the pseudolites in the highbay is driven by their clock stability, and is better than 2 kHz for the pseudolites used in this testbed.

The phase error bound due to the sample time error is then

$$2 \text{ mm} \approx 60 \text{ KHz (doppler)} * 100 \text{ ns (sample time error)} * 0.19 \text{ m} \\ (\text{carrier wavelength}) * 2$$

which may be ignored as it is below the receiver phase noise. The factor of 2 accounts for the sample time error of both receivers. The phase errors associated with the clocks on each receiver are solved for as part of the clock bias term, τ . This bound is for the on-orbit application, where the observed doppler is highest. The phase errors are significantly smaller on Earth due to the reduced dopplers.

Continuously slewing the sample times in hardware offers two advantages compared to the phase extrapolation.

1. Less computation is required since the phase extrapolation to account for the sample time error is unnecessary.
2. The phase rates are not required to be passed between the vehicles in the system as part of the data message.

Another consideration is the sample time *drift* between hardware slews on each receiver. In particular, the clocks on the receivers used in the blimp testbed are stable to about 1 part in 10^6 . Therefore, between hardware slews, the true sample time could drift by as much as $1\text{e-}6$ sec/sec. Because of this, the phase error bound will grow if data is used at a higher rate than the hardware slew rate.

The hardware sample time slew was set at 1 Hz in the blimp testbed, but phase measurements were latched by the receivers at 10 Hz, and this is the rate the estimator ran at. Hence, the phase error bound will grow from the minimum value just after the hardware slew, to its maximum value just prior to the next. For the blimp application, this amounted to a maximum phase error bound of

$$1 \text{ mm} \approx 2 \text{ KHz (doppler)} * 1 \mu\text{sec (max sample time error)} * \\ 0.19 \text{ m (carrier wavelength)} * 2$$

which is on the order of the receiver phase noise. The maximum bound is about 4 mm when outside the highbay, since the dopplers to the satellites can be larger. For vehicles on-orbit, the phase error bound would grow to about 2 cm if data were used at 10 Hz, but the hardware sample time slew was only 1 Hz. However, for the space application, it is likely that the relative position estimation does not need to be updated at greater than 1 Hz. Regardless, the slew times can be increased to match the data rate to eliminate the effects of the sample time drift.

4.5 Formation Measurement Equations - General Problem

The GPS measurement equations may be broken into two separate components for the general formation flying application. The first set of measurements are derived by

forming differences between antennas internal to each vehicle. These are referred to as the intra-vehicle measurements. The second set of measurement components are derived by forming differences *between* each vehicle in the cluster. These are referred to as the inter-vehicle measurements.

4.5.1 Vehicle Attitude

The typical application will have visibility to the NAVSTAR satellites, and as such, a coarse absolute position estimate may be developed from standard pseudorange techniques [GPS96]. This will provide sufficiently accurate estimates of each satellite's line-of-sight (LOS) to compute the vehicle attitude. This allows the attitude to be computed independently of the *relative* positions of the vehicles within the cluster. The intra-vehicle single differences are formed using a maximal set of independent measurements as will be discussed in Chapter 6. These measurements can be written, for vehicle i , in the general vector form:

$$\Delta\Phi_i = f_i(\Psi_{ai}, \Theta_{ai}, \Phi_{ai}) + \beta_i + \nu_i \quad (4.14)$$

where

- $\Delta\Phi_i$ = vector of independent intra-vehicle single differences for vehicle i
- $\Psi_{ai}, \Theta_{ai}, \Phi_{ai}$ = vehicle Euler angles
- $f_i(\Psi_a, \Theta_a, \Phi_a)$ = function relating the vehicle Euler angles to the measured differential carrier-phases

β_i = vector of biases for corresponding set of differential phase measurements. These biases may include line biases, and as such are not necessarily integer.

Solutions to Eq. 4.14, as well as the attitude bias initialization problem are discussed in greater detail in Cohen [CC92].

4.5.2 Relative Positioning

The second major measurement component is derived by forming differences across the vehicles within the formation cluster. These measurements will be used to determine the *relative* position of the vehicles. Principally, these measurements will be derived from two sources: the NAVSTAR satellites, and onboard pseudolites (GPS transmitters). The onboard pseudolites serve two primary functions:

1. They provide an additional ranging signal that can be used to augment the measurements available from the NAVSTAR satellites. The main benefit of this is an improved GDOP, resulting in increased positioning accuracy. However, there are several applications (*e.g.* at GEO and in deep space) where on-board pseudolites are required since there is not sufficient visibility to the GPS satellites. Even in Low Earth Orbit (LEO), the NAVSTAR signals can be occluded by other structures if multiple vehicles are working close together. An example of this would be autonomous satellites working in close proximity to the Space Station.

2. They provide the means to initialize the carrier-phase biases associated with the inter-vehicle measurements. The onboard pseudolites enable *relative* vehicle motion to be used as an initialization technique, which can significantly decrease the time required to initialize for many applications. This subject will be addressed in Chapter 5.

Eq. 4.1 gives the measured carrier phase received at a given antenna from a specified transmitter. Single differences can then be formed across the vehicles within the formation using the signals from the NAVSTAR satellites. The bias terms that appear in these equations are a result of the ambiguity associated with measuring the GPS carrier-phase. (see Chapter 1). These bias terms must be accurately solved for before the relative position states may be estimated to centimeter-level accuracies.

Attaching the formation coordinate system (X_f, Y_f, Z_f) (Figure 4.1) to a *master* vehicle (designated as vehicle m), the measurements from the NAVSTAR constellation can then be written in vector form as

$$\Delta\phi_{mi}^s = G_i \begin{bmatrix} X_i \\ \tau_i \end{bmatrix} + \beta_{mi}^s + \nu_{mi}^s \quad (4.15)$$

where

$\Delta\phi_{mi}^s$ = differential carrier phase between vehicle m , and vehicle i using the NAVSTAR signals

$$G_i = \begin{bmatrix} los_1 & 1 \\ los_2 & 1 \\ \vdots & \vdots \\ los_n & 1 \end{bmatrix}$$

X_i = position of vehicle i relative to vehicle m

τ_i = relative clock bias between receiver on vehicle m , and vehicle i ,

β_{mi}^s = carrier-phase biases for the single-differences between vehicle m and i using the NAVSTAR signals.

ν_{mi}^s = carrier-phase noise for the single-differences between vehicle m and i using the NAVSTAR signals.

G_i is the traditional geometry matrix. The components los_i are the line-of-sights to the i^{th} NAVSTAR satellite in the formation coordinate frame. Depending on the orientation of the antennas on each vehicle, it is likely that only a sub-set of all the visible satellites are available on a particular antenna on each vehicle. For example, Pseudo-Random Numbers (PRN) 1-6 might be available on antenna 1, and PRN 7 may be available on antenna 2 on a specific vehicle. For this reason, the inter-vehicle single differences are likely to be formed using several antennas on a given vehicle in order to maximize the number of independent measurements. This is easily accounted for in the estimation, since the attitude for each vehicle will be known before solving for the relative positions. This technique is referred to as the “all-baseline-in-view” measurement formulation, and is discussed in more detail in Chapter 6.

For an N-vehicle formation, these measurements are combined into one equation as

$$\Delta\Phi = \begin{bmatrix} G_1 & & & 0 \\ & G_2 & & \\ & & \ddots & \\ 0 & & & G_{N-1} \end{bmatrix} \begin{bmatrix} X_1 \\ \tau_1 \\ \vdots \\ X_{N-1} \\ \tau_{N-1} \end{bmatrix} + \begin{bmatrix} \beta_{11}^s \\ \beta_{12}^s \\ \vdots \\ \beta_{N-1,N-1}^s \end{bmatrix} + \nu \quad (4.16)$$

$$\Delta\Phi = \hat{G}\hat{X} + \hat{\beta} + \nu \quad (4.17)$$

where it is assumed that vehicle m had visibility to all available satellites. In general this is not the case, and \hat{G} will have off-diagonal terms corresponding to the single differences that can be made between vehicles using NAVSTAR signals not available on the *master* vehicle. However, for simplicity the equations will be developed using this assumption.

If the k^{th} GPS satellite was not visible on vehicle m , but was visible on vehicles i and j , then the following single difference would be formed

$$\Delta\phi = \text{los}_k(X_j - X_i) + \tau_j - \tau_i + \beta + \nu \quad (4.18)$$

This measurement would be added to those using the *master* vehicle, and would appear in the off-diagonal elements of \hat{G} .

In addition to those signals generated by the NAVSTAR constellation, each vehicle could have an onboard pseudolite, which provides additional measurements. The transmitter on vehicle m can be used to form measurements that are given by

$$\Delta\phi^p_{mi} = d_{mi}(X_i) + \tau_i + \beta^p_{mi} + \nu^p_{mi} \quad (4.19)$$

where

- $\Delta\phi^p_{mi}$ = differential carrier phase between vehicle m , and vehicle i using the pseudolite signal generated on vehicle m
- $d_{mi}(X_i)$ = distance between vehicle m and vehicle i
- τ_i = relative clock bias between receiver on vehicle m and vehicle i ,
- β^p_{mi} = carrier-phase biases for the single-difference between vehicle m and i using the pseudolite on vehicle m

ν_{mi}^p = carrier-phase noise for the single-difference between vehicle m and i using the pseudolite on vehicle m

The pseudolite signal generated on vehicle m is assumed to have been measured on the vehicle itself. This can be accomplished by running the signal through a splitter to both the transmit antenna and the receiver.

The single difference formed between vehicles i and m , using the transmitter on vehicle i can be written as

$$\Delta\phi_{im}^p = d_{im}(X_i) - \tau_i + \beta_{im}^p + \nu_{im}^p \quad (4.20)$$

Additionally, measurements can be formed between vehicles i and j (using the transmitter on vehicle i), exclusive of vehicle m . These are written as

$$\Delta\phi_{ij}^p = d_{ij}(X_i, X_j) + \tau_j - \tau_i + \beta_{ij}^p + \nu_{ij}^p \quad (4.21)$$

In this case, the range and relative clock biases between the two vehicles are written in terms of their positions relative to vehicle m and the clock biases relative to vehicle m . The single difference made using the transmitter on vehicle j is derived by interchanging the indexes in Eq. 4.21. These differences are formed between all of the vehicles in the system in order to generate a maximal set of independent measurements. Note that for an N -vehicle formations, there are a total of $N \times (N - 1)$ independent inter-vehicle single differences that can be formed. If double differences were used, there would be a total of $N \times (N - 1)/2$ independent measurements (fewer measurements, but also fewer unknowns).

Similar to the attitude case, these measurements cannot be used to generate the cm-level relative position estimates until the biases are accurately determined. The determination of the relative position biases for the formation flying problem is the subject of Chapter 5.

4.6 Blimp Attitude and Position Coupling

When operating inside the highbay, the line-of-sights to each of the pseudolites in the room is highly dependent on the absolute location within the room. For example, a 10 ft position error could result in the computed line-of-sight being in error by as much as 15 deg. It is the line-of-sight dependence on the vehicle's positions within the cluster that couple the blimp attitudes and positions within the highbay. In effect, the precise absolute, as well as relative, positions are required for the indoor application. This coupling does not exist for the general case of a cluster using the NAVSTAR constellation.

4.7 Blimp Testbed Measurement Equations

The attitude and positions of each blimp are coupled when operating in the highbay, and as such all the states must be solved for simultaneously. The intra-vehicle single differences for each blimp are formulated using the available measurements, and are expressed in vector form as:

$$\Delta\Phi_i = h_i(X_i, \psi_{ai}, \theta_{ai}, \phi_{ai}) + \beta_i + \nu_i \quad (4.22)$$

where

$\Delta\Phi_i$	= intra-vehicle single differences for blimp i
$h_i(X_i, \psi_{ai}, \theta_{ai}, \phi_{ai})$	= kinematic function relating the i th blimp's position and attitude to the measured differential phase
β_i	= intra-vehicle single difference biases

Each blimp has a body frame attached to the gondola. The location of the antennas mounted on each blimp were surveyed in, and are specified in this frame. The function h_i is dependent on the location of each of the mounted antennas (assumed fixed in the body frame attached to the gondola), as well as the location of the fixed pseudolites within the room.

The inter-vehicle measurements may be formulated using either single differences or double differences. Double differences explicitly eliminate the relative clock bias at the cost of more bookkeeping. The choice of which method is somewhat arbitrary, but for this research double differences were used.

Because of the near-pseudolite constellation, the precise location within the room is required as explained in Section 4.6. For this reason, a reference station was placed within the highbay at a fixed location. Use of the reference station was required when only one blimp was operational. Because the attitude and position are coupled, the reference station may be omitted when two blimps are in use. However, because the coupling is weak, the absolute position solutions are degraded when the reference station is not used, resulting in degraded attitude solutions. A reference station is not required when operating outside with the NAVSTAR constellation because the absolute position may be obtained to sufficient accuracy with pseudorangeing.

Two sets of double differences are employed. One set is formed by differencing measurements between one blimp and the reference station. The other set is obtained by differencing measurements between the blimps themselves. These may be expressed as:

$$\nabla\Delta\Phi_{1ref} = h_{1ref}(X_1, \psi_{a1}, \theta_{a1}, \phi_{a1}) + \beta_{1ref} + \nu_{1ref} \quad (4.23)$$

$$\nabla\Delta\Phi_{21} = h_{21}(X_1, \psi_{a1}, \theta_{a1}, \phi_{a1}, X_2, \psi_{a2}, \theta_{a2}, \phi_{a2}) + \beta_{21} + \nu_{21} \quad (4.24)$$

Similar to the intra-vehicle difference equations, the kinematic functions h_{1ref} , and h_{21} are dependent on the antenna locations on the blimps, and the locations of the pseudolites within the room. These must be used to solve for all the states simultaneously, and are collected together into one vector equation of the form

$$\begin{bmatrix} \Delta\Phi_1 \\ \Delta\Phi_2 \\ \nabla\Delta\Phi_{1ref} \\ \nabla\Delta\Phi_{21} \end{bmatrix} = \begin{bmatrix} h_1 \\ h_2 \\ h_{1ref} \\ h_{21} \end{bmatrix} + \begin{bmatrix} \beta_1 \\ \beta_2 \\ \beta_{1ref} \\ \beta_{21} \end{bmatrix} + \nu \quad (4.25)$$

4.8 State Estimation

Eq. 4.17 and 4.25 are the measurement equations used in the state estimation for the formation flying application (both the blimp testbed inside the highbay, and the general application using the NAVSTAR constellation). These equations may be written in the general form

$$y = h(x) + \beta + \nu \quad (4.26)$$

where

- y = vector of measurements
- x = formation state vector
- $h(x)$ = function relating measurements to formation state

The measurement equation is non-linear for the blimp testbed when flying inside the highbay, and is linear for the general application outside when using the NAVSTAR constellation without on-board pseudolites. Assuming the biases are known, the state estimation may be performed using an Extended Kalman Filter (EKF) [AG74] when vehicle plant models are available. Alternatively, a simple least squares estimation may be used to solve for the state.

For the least squares estimate, Eq. 4.26 can be linearized about the best guesses of the current state, \hat{x} , to give

$$y_k \cong h_k(\hat{x}_k) + H_k(\hat{x}_k)\delta x_k + \beta + \nu_k \quad (4.27)$$

and

$$\rho_k = y - h_k(\hat{x}_k) - \beta \cong H_k(\hat{x}_k)\delta x_k + \nu_k \quad (4.28)$$

where

$$H_k = \text{Jacobian of } h \text{ evaluated at } \hat{x}$$

The weighted least squares solution is found by iterating on the solution of

$$\delta \hat{x} = (\tilde{H}_k^T R^{-1} \tilde{H}_k)^{-1} \tilde{H}_k^T R^{-1} \rho \quad (4.29)$$

where

$$\hat{x}_{\text{new}} = \hat{x}_{\text{old}} + \delta\hat{x} \quad (4.30)$$

The weighting matrix, R , may be taken to be the received signal SNRs, since the carrier phase noise increases with decreasing SNR.

~

Chapter 5

Carrier-Phase Bias Initialization

One of the main challenges in using CDGPS for the formation state estimation is computing the carrier-phase biases necessary to perform centimeter-level relative positioning. This chapter discusses the initialization of the biases using standard approaches, and using pseudolites onboard the vehicles within the formation. A measure of the bias observability for a cluster of vehicles is also derived. Finally, the computation of the exact optimal, as well as quasi-optimal initialization maneuvers are presented, along with some experimental results using these maneuvers.

5.1 Measurement Equations

The measurement equations that are available from both the NAVSTAR constellation, as well as the onboard pseudolites are presented again for reference. The bias terms that appear in these equations are a result of the ambiguity associated with measuring the GPS carrier-phase (see Chapter 1). These bias terms must be accurately solved for before the relative position states can be estimated to centimeter-level accuracies.

Attaching the formation coordinate system (X_f, Y_f, Z_f) (figure 4.1) to a *master* vehicle (designated as vehicle m), the measurements from the NAVSTAR constellation can then be written in vector form as (repeat of Eq. 4.15)

$$\Delta\phi_{mi}^s = G_i \begin{bmatrix} X_i \\ \tau_i \end{bmatrix} + \beta_{mi}^s + \nu_{mi}^s \quad (5.1)$$

where

$\Delta\phi_{mi}^s$ = differential carrier phase between vehicle m , and vehicle i using the NAVSTAR signals

$$G_i = \begin{bmatrix} los_1 & 1 \\ los_2 & 1 \\ \vdots & \vdots \\ los_n & 1 \end{bmatrix}$$

X_i = position of vehicle i relative to vehicle m

τ_i = relative clock bias between receiver on vehicle m , and vehicle i ,

β_{mi}^s = carrier-phase biases for the single-differences between vehicle m and i using the NAVSTAR signals.

ν_{mi}^s = carrier-phase noise for the single-differences between vehicle m and i using the NAVSTAR signals.

G_i is the traditional geometry matrix. The components los_i are the line-of-sights to the i^{th} NAVSTAR satellite in the formation coordinate frame.

For an N-vehicle formation, these measurements are combined into one equation as

$$\Delta\Phi = \begin{bmatrix} G_1 & & 0 \\ & G_2 & \\ & & \ddots \\ 0 & & & G_{N-1} \end{bmatrix} \begin{bmatrix} X_1 \\ \tau_1 \\ \vdots \\ X_{N-1} \\ \tau_{N-1} \end{bmatrix} + \begin{bmatrix} \beta^s_1 \\ \beta^s_2 \\ \vdots \\ \beta^s_{N-1} \end{bmatrix} + \nu \quad (5.2)$$

$$\Delta\Phi = \hat{G}\hat{X} + \hat{\beta} + \nu \quad (5.3)$$

where it is assumed that vehicle m had visibility to all available satellites. In general this is not the case, and \hat{G} will have off-diagonal terms corresponding to the single differences that can be made between vehicles using NAVSTAR signals not available on the *master* vehicle. However, for simplicity the equations will be developed using this assumption.

If the k^{th} GPS satellite was not visible on vehicle m , but was visible on vehicles i and j , then the following single difference would be formed

$$\Delta\phi = \log_k(X_j - X_i) + \tau_j - \tau_i + \beta + \nu \quad (5.4)$$

This measurement would be added to those using the *master* vehicle, and would appear in the off-diagonal elements of \hat{G} .

In addition to those signals generated by the NAVSTAR constellation, each vehicle could have an onboard pseudolite, which provides additional measurements. The

transmitter on vehicle m can be used to form measurements that are given by

$$\Delta\phi^p_{mi} = d_{mi}(X_i) + \tau_i + \beta^p_{mi} + \nu^p_{mi} \quad (5.5)$$

where

- $\Delta\phi^p_{mi}$ = differential carrier phase between vehicle m , and vehicle i using the pseudolite signal generated on vehicle m
- $d_{mi}(X_i)$ = distance between vehicle m and vehicle i
- τ_i = relative clock bias between receiver on vehicle m and vehicle i ,
- β^p_{mi} = carrier-phase biases for the single-difference between vehicle m and i using the pseudolite on vehicle m
- ν^p_{mi} = carrier-phase noise for the single-difference between vehicle m and i using the pseudolite on vehicle m

The pseudolite signal generated on vehicle m is assumed to have been measured on the vehicle itself. This can be accomplished by running the signal through a splitter to both the transmit antenna and the receiver.

The single difference formed between vehicles i and m , using the transmitter on vehicle i can be written as

$$\Delta\phi^p_{im} = d_{im}(X_i) - \tau_i + \beta^p_{im} + \nu^p_{im} \quad (5.6)$$

Additionally, measurements can be formed between vehicles i and j (using the transmitter on vehicle i), exclusive of vehicle m . These are written as

$$\Delta\phi^p_{ij} = d_{ij}(X_i, X_j) + \tau_j - \tau_i + \beta^p_{ij} + \nu^p_{ij} \quad (5.7)$$

In this case, the range and relative clock biases between the two vehicles are written in terms of their positions relative to vehicle m and the clock biases relative to vehicle m . The single difference made using the transmitter on vehicle j is derived by interchanging the indexes in Eq. 5.7. These differences are formed between all of the vehicles in the system in order to generate a maximal set of independent measurements. Note that for an N -vehicle formations, there are a total of $N \times (N - 1)$ independent inter-vehicle single differences that can be formed. If double differences were used, there would be a total of $N \times (N - 1)/2$ independent measurements (fewer measurements, but also fewer unknowns).

The measurement equations presented in this section are used to estimate the relative positions of the vehicles in the formation. However, the biases must be accurately solved for before cm-level relative position estimates can be obtained. The solution of the biases is presented in the following sections.

5.2 Initialization of the Relative Position Biases

In practice, there are two approaches to initializing the carrier-phase biases for the relative position problem [GPS96]. The first is to wait for the GPS satellites to move about in their orbits, resulting in line-of-sight changes between the NAVSTAR constellation and the formation itself. The advantage of this method is that the vehicles within the formation do not need to undergo any relative motion themselves. The disadvantage is that this will typically take too long for some applications [DL96]. A second approach, already used successfully in several applications, is to use a fixed pseudolite in the area of operation. For both the IBLIS [DL96], and autonomous tractor [MOC97] applications, a single vehicle underwent motion relative to the pseudolite

to allow for a rapid solution to the bias problem. Note, however, that the maneuvers were constrained to 2-D for the tractor problem, and were non-optimized in the IBLS application.

This approach is not practical for the formation flying problem, however, since it may be physically impossible to place a fixed pseudolite (*e.g.* on-orbit), and it significantly restricts the area of operation for the system. An alternative approach is to include onboard pseudolites, which will then allow relative motion between the vehicles in the cluster to be used to solve for the carrier-phase biases. This should allow for a rapid solution to the bias ambiguity problem without the restrictions of a fixed pseudolite. These two approaches (GPS satellite motion and onboard pseudolites) are discussed in more detail in the following sections.

5.3 GPS Satellite Motion

Eq. 5.2, and 5.3 show the general form of the measurement equation for an N-vehicle formation using the NAVSTAR constellation. The biases can then be solved for using a Kalman filtering technique similar to the one developed by Lawrence [DL96]. For this technique, define L as the left nullspace of \hat{G} . Multiplying both sides of Eq. 5.3 by L yields

$$L\Delta\Phi = L\hat{G}\hat{X} + L\hat{\beta} + L\nu \quad (5.8)$$

$$= L\hat{\beta} + L\nu \quad (5.9)$$

which can be written in the general form

$$z = H\hat{\beta} + \hat{\nu} \quad (5.10)$$

where $H = L$. The multiplication by L decouples the biases from the state, thus allowing the biases to be estimated *separately*. Given the estimate of the biases, a Kalman filter or a simple least squares algorithm can be run using Eq. 5.3 to estimate the position states. Eq. 5.10 is in the general form for a linear observation, and it can be used in the minimum variance measurement update [AG74]

$$K = P_N^- H^T [H P_N^- H^T + R]^{-1} \quad (5.11)$$

$$\hat{\beta}^+ = \hat{\beta}^- + K(z - H\hat{\beta}^-) \quad (5.12)$$

$$P_N^+ = [I - KH] P_N^- \quad (5.13)$$

where $R = E[\nu\nu^T]$, the covariance of the differential carrier-phase noise. The Kalman filter equations are propagated at the system measurement rate (typically 1-5 Hz). Eq. 5.12 provides an updated estimate of the floating point bias, β , and the corresponding covariances are given by P_N . As the GPS satellites move about in their orbits, the line-of-sights to the GPS constellation change, resulting in changes to the formation geometry matrix, \hat{G} . These line-of-sight changes provide the observability required to estimate the biases.

Note that the biases can also be updated using the differential code measurements that are available. In this case, a direct estimate of the biases is obtained (since the code measurements do not suffer from the integer ambiguity problem). The bias estimate using the code measurement is given by

$$\hat{\beta} = \Delta\phi - \Delta\rho \quad (5.14)$$

where $\Delta\rho$ is the differential code measurement. Since both the differential code measurements (Eq. 1.2), and differential carrier-phase measurements contain the range and clock bias terms, the resulting difference is the bias estimate.

The code update is then performed by setting

$$z = \Delta\phi - \Delta\rho \quad (5.15)$$

$$H = I \quad (5.16)$$

$$R = (\sigma_{\Delta\rho}^2 + \sigma_{\Delta\phi}^2)I \quad (5.17)$$

where $\sigma_{\Delta\rho}$ is the STD of the differential code measurement. Eq. 5.15 also provides the initial bias estimate to the filter. Note that the differential code error tends to be correlated over short periods [GPS96], so this update should be performed at rates comparable to the decorrelation rate.

Figure 5.1 shows a plot of the relative position bias-STD (maximum over all biases) vs. time for several simulated formations. The plot shows four different formations, one for a terrestrial application, and three others at various altitudes in Low Earth Orbit (LEO). Each formation was simulated to be in the Equatorial plane of the Earth, and there were no onboard pseudolites. The bias estimates improved as a result of the relative motion between the formation and the GPS satellites. Intuitively, due to its own velocity, the formation on-orbit has significantly more relative motion to the GPS constellation than the cluster on the ground. This results in much faster initialization times for a formation on-orbit, as compared to the terrestrial case. The brief spikes in the STD in each plot are a result of a new satellite being brought on-line as it becomes visible. In this simulation, the biases were initialized using the code-phase measurement, and as a result the bias STD was set equal to the differential

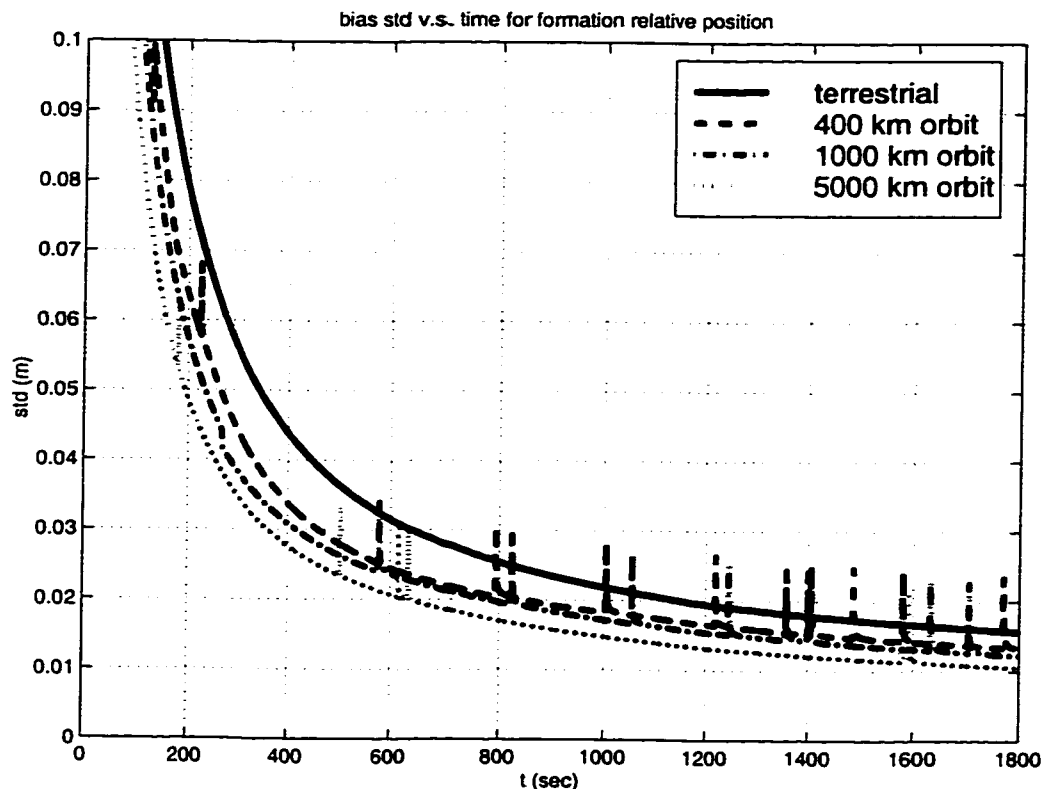


Fig. 5.1: Initialization using GPS Satellite Motion. The Formations were Simulated to be in the Equatorial Plane of the Earth. A GPS Almanac was used to Propagate the Orbits of the GPS Constellation. The Formations were Assumed to be in Circular Orbits. $\sigma_{carrier} = 0.5$ cm, $\sigma_{code} = 1.4$ m. The Kalman Filter was Propagated at 1 Hz.

code phase noise ($\sigma_{\Delta code} = 2$ m). As such, the spike was actually off the graph for one iteration (the spike was shortened in the plot for clarity). The Kalman filter improved the estimate of the newly acquired bias in the following iteration to the same level of accuracy as the others in the system. The frequency of the satellite hand-overs (indicated by the spikes) is quite a bit higher for the formation on-orbit due to its much higher velocity.

Figure 5.2 shows a flow graph for the simulation. The orbits of the GPS satellites, and vehicles were propagated using Kepler's equations. At each epoch, the line-of-sight (LOS) to each of the GPS satellites was computed, and the visibility was

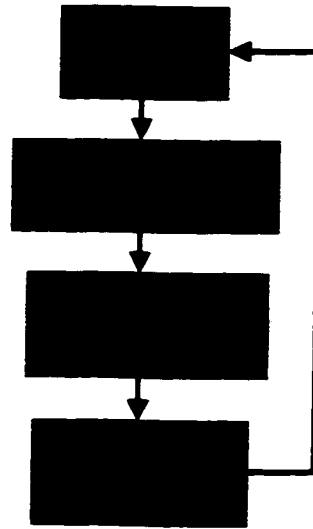


Fig. 5.2: Orbit Simulation Flow Chart. Estimation Update Rate was 1 Hz. $\sigma_{carrier} = 0.5$ cm, $\sigma_{code} = 1.4$ m, Visibility Mask Angle = 5° Above the Limb of the Earth.

Table 5.1: Bias Initialization Times (sec)

Terrestrial	400 km	1000 km	5000 km
1149	849	780	632

determined. The carrier and code updates were performed at 1 Hz. The simulation went from $t = 0$ sec to $t = 1800$ sec (30 min).

Table 5.1 summarizes the results of the simulation. The table lists the time it takes to initialize all of the biases with a STD of at most 2 cm, which will result in a reliable estimate. The terrestrial formation requires about 19 minutes, whereas the on-orbit formations only require about 10-13 minutes, depending on their altitude.

Many terrestrial applications will require the formation to be initialized quickly, and the 15-20 minutes it takes to wait for the GPS satellites to move about overhead may be too long. For example, an autonomous air-to-air refueling application will require a refueling tanker to service many aircraft in short periods of time. Note that, without onboard pseudolites, relative vehicle motions within the fleet would result in very

small changes in the line-of-sight to the NAVSTAR constellation (which is presumably very far away) and thus would not be a fuel-effective means of initializing the integers. If the L_2 GPS signal is available, the integers could be estimated more rapidly by using wide-laning techniques [GPS96]. However, the L_2 signal is not available to most receivers, as it is an encrypted signal for use by the military.

5.4 Formation NDOP

As discussed, one approach that can be used to significantly reduce the initialization time is to include onboard pseudolites. The relative motion between the vehicles in the cluster will then allow the biases to be initialized very rapidly. Additionally, any system that is operating with onboard pseudolites that does not have visibility to the NAVSTAR satellites (*i.e.* a deep space constellation) would require relative motion in order to initialize the biases quickly.

Note that there are a number of issues related to using pseudolites onboard a vehicle. In particular, antenna design and placement, near/far issues [CS97], signal visibility, and robustness must be addressed. Corazzini has incorporated pseudolites on the robots in the 2-D testbed [TC98], and her research has addressed many of these problems.

In order to analyze the relative motions that the vehicles within a formation will undergo, some measure of the quality of the maneuver must be developed. In this case, a key parameter is the bias observability (*e.g.* how well can the biases be estimated given the prescribed vehicle motions). This measure can be quantified by the *formation NDOP*, which acts as a scaling between the measurement noise and the resulting bias covariance. The development here extends the derivation of the NDOP

for the single vehicle case found in [DL96] to the multi-vehicle case with onboard pseudolites.

To formulate the formation NDOP, the vector equations, Eqs. 5.1, 5.5, 5.6, and 5.7 are collected together. Note that it is impossible to compute the individual biases exactly because the clock biases, τ_i , enter into each of the equations in the same way. However, it is possible to compute the difference in the biases, and that is all that is required for the solution of the relative positions. To proceed, we group an arbitrary satellite bias, β_{1mi}^s , with the clock bias, τ_i , and rewrite Eqs. 5.1, 5.5, 5.6, and 5.7 as

$$\begin{aligned} \Delta\phi_{mi}^s &= \begin{bmatrix} G & \bar{I} \end{bmatrix} \begin{bmatrix} X_i \\ \tau_i + \beta_{mi}^{s1} \\ \beta_{mi}^{s2} - \beta_{mi}^{s1} \\ \vdots \\ \beta_{mi}^{sn} - \beta_{mi}^{s1} \end{bmatrix} + \nu_{mi}^s \\ &= \begin{bmatrix} G & \bar{I} \end{bmatrix} \begin{bmatrix} X_i \\ \tilde{\tau}_i \\ \tilde{\beta}_{mi}^s \end{bmatrix} + \nu_{mi}^s \end{aligned} \quad (5.18)$$

$$\Delta\phi_{mi}^p = d_{mi}(X_i) + \tilde{\tau}_i + \tilde{\beta}_{mi}^p + \nu_{mi}^p \quad (5.19)$$

$$\Delta\phi_{im}^p = d_{im}(X_i) - \tilde{\tau}_i + \tilde{\beta}_{im}^p + \nu_{im}^p \quad (5.20)$$

$$\Delta\phi_{ij}^p = d_{ij}(X_i, X_j) + \tilde{\tau}_i - \tilde{\tau}_j + \tilde{\beta}_{ij}^p + \nu_{ij}^p \quad (5.21)$$

where

$$\tilde{\tau}_i = \tau_i + \beta_{mi}^{s1} \quad (5.22)$$

$$\tilde{\beta}_{mi}^s = \begin{bmatrix} \beta^{s_2}_{mi} - \beta^{s_1}_{mi} \\ \vdots \\ \beta^{s_n}_{mi} - \beta^{s_1}_{mi} \end{bmatrix}, \quad \bar{I} = \begin{bmatrix} \bar{0} \\ I \end{bmatrix} \quad (5.23)$$

$$\tilde{\beta}_{mi}^p = \beta^p_{mi} - \beta^{s_1}_{mi}, \quad \tilde{\beta}_{ij}^p = \beta^p_{ij} - \beta^{s_1}_{mi} - \beta^{s_1}_{mj} \quad (5.24)$$

I is the $n - 1 \times n - 1$ identity matrix, where n is the number of visible NAVSTAR satellites, and $\bar{0}$ is a row of zeros.

Define μ as the state vector consisting of the relative position states, and clock biases for all the vehicles in the cluster

$$\mu = \begin{bmatrix} X_1 \\ \bar{\tau}_1 \\ \vdots \\ X_{N-1} \\ \bar{\tau}_{N-1} \end{bmatrix} \quad (5.25)$$

Then, Eqs. 5.18 - 5.21 are evaluated for all the vehicles in the formation to generate a set of independent measurements that are combined into the general form $y = h(\mu) + \beta + \nu$. In this case, h is a vector function consisting of all the available measurements derived from the NAVSTAR constellation and onboard pseudolites. The formation geometry matrix at some epoch, \hat{G}_k , is then

$$\hat{G}_k = \left. \frac{\partial h(\mu)}{\partial \mu} \right|_{t_k} = \begin{bmatrix} G_1 & & 0 \\ & \ddots & \\ 0 & & G_{N-1} \\ & \frac{\partial \Delta \Phi_{ij}}{\partial \mu} & \end{bmatrix}_k \quad (5.26)$$

where

$\Delta\Phi_{ij}$ = stacked vector of independent difference (single or double) equations using the onboard pseudolites across all the vehicles, including vehicle m

The general, linearized measurement equation is then written as

$$\Delta\Phi_k = \hat{G}_k\mu + \hat{I}\beta + \nu_k \quad (5.27)$$

where

$$\hat{I} = \begin{bmatrix} \bar{I} & & 0 \\ & \ddots & \\ & & \bar{I} \\ 0 & & \bar{I} \end{bmatrix} \quad (5.28)$$

\bar{I} is the $p \times p$ identity matrix, where p is the number of biases associated with the pseudolite measurements. The formation NDOP is computed over q epochs during the initialization maneuver. Then, for $k = 1, \dots, q$, define L_k as the left nullspace of \hat{G}_k . Multiplying Eq. 5.27 by L_k , and stacking over all epochs $k = 1, \dots, q$ yields

$$\bar{z} = \begin{pmatrix} z_1 \\ z_2 \\ \vdots \\ z_q \end{pmatrix} = \bar{L}\hat{I}\beta + \bar{\nu} \quad (5.29)$$

where

$$\bar{L} = \begin{bmatrix} L_1 \\ L_2 \\ \vdots \\ L_q \end{bmatrix} \quad (5.30)$$

As before, Eq. 5.29 can be used to solve for $\hat{\beta}$ in a least squares sense as

$$\hat{\beta} = (\hat{I}^T \bar{L}^T \bar{L} \hat{I})^{-1} \hat{I}^T \bar{L}^T \bar{z} \quad (5.31)$$

Hence, assuming uncorrelated measurement noise, the estimate error, $\tilde{\beta}$, covariance is

$$E [\tilde{\beta} \tilde{\beta}^T] = (\hat{I}^T \bar{L}^T \bar{L} \hat{I})^{-1} \sigma_{carrier}^2 \quad (5.32)$$

Using Eq. 5.32, the formation NDOP is defined in an analogous manner to PDOP and GDOP [GPS96], and is the scaling between measurement noise (STD σ) and the 1- σ bias estimate.

$$NDOP = \sqrt{\text{trace}(\hat{I}^T \bar{L}^T \bar{L} \hat{I})^{-1}} \quad (5.33)$$

Therefore, the smaller NDOP, the more accurate the bias estimate will be. Note that it was assumed in the derivation of Eq. 5.26 that vehicle m had visibility to all the GPS satellites visible to the other vehicles. If this is not the case, the block diagonal portion of the matrix would have to be modified to include the off-diagonal terms corresponding to the single differences that can be made exclusive of vehicle m (see Eq. 5.4).

5.5 Optimal Bias Initialization Maneuvers

The motivation to put onboard pseudolites on the vehicles in the cluster is to enable the biases to be initialized more quickly than would be otherwise possible. Pseudolite augmentation is necessary for any application in which satellite motion alone takes too long and fixed pseudolites are impractical. As shown in the previous section, the resulting bias observability for any initialization maneuver can be evaluated using Eq. 5.33. In the application of Eq. 5.33, it will be assumed that the lines-of-sight to all the NAVSTAR satellites remain essentially constant. The assumption is good in most cases, as the observability is primarily driven by the relative vehicle motion, and the maneuver will, by definition, occur in a short time period relative to the scale of large GPS satellite line-of-sight changes. If large LOS changes to the GPS satellites have occurred, then the relative position biases could be solved for without any vehicle motion.

In general, if relative vehicle motion is required to initialize the biases, then this naturally leads to the question of what are the “best” maneuvers to perform. The optimization here is typically based on minimizing the amount of time for the maneuver, or the amount of fuel used. Constraints must also be included to account for limited actuator authority and collision avoidance. The formulation of the optimal control, minimum time maneuver is given by

$$\min T_f$$

subject to

$$\begin{aligned}
 \dot{x}_i &= f_i(x, u, t) && - \text{vehicle dynamics} \\
 \psi(x(t_f)) &= 0 && - \text{terminal relative position/velocity constraints} \\
 \|p_i(t) - p_j(t)\| &> d && - \text{minimum separation between vehicles } i \text{ and } j \\
 NDOP &< C && - \text{desired bias observability after maneuver} \\
 \|u_i\| &< u_{\max} && - \text{actuator constraints}
 \end{aligned}$$

where

T_f = time of initialization maneuver

x_i = state of vehicle i in (X_f, Y_f, Z_f) frame

p_i = position of the i th vehicle

d = minimum separation between vehicles

C = minimum desired NDOP

It is not possible to solve the optimal control problem analytically. However, the problem can be solved numerically using inverse dynamic programming [BA99]. Essentially, the problem is converted into a nonlinear programming problem that can be solved using a number of readily available software packages, such as Matlab [MAT]. The parameters in the optimization are the key states of the vehicles, and the optimal control is then computed from the solution of these states. For example, the equation of motion for a double integrator plant [SH94] is

$$\dot{x} = v \tag{5.34}$$

$$\dot{v} = a \tag{5.35}$$

The parameter vector to the optimization would be points on the velocity history $v(t)$. The position can be obtained by integrating $v(t)$, and the control, $a(t)$, can be obtained by differentiating $v(t)$.

There are several constraints listed in the problem formulation above. Of principle concern is the constraint on the formation NDOP. The satisfaction of that constraint will guarantee sufficient visibility of the biases. The constraint on minimum separation distances between the vehicles is driven by two factors. The first, of course, is the fact that the vehicles cannot be allowed to collide without catastrophic consequences. Another issue is the near/far problem resulting from the onboard pseudolites [CS97]. As the vehicles move about one another, the varying separation distances will also result in fluctuations in the received power levels at the receive antennas. It is possible for a nearby pseudolite to essentially drown-out the signals from the NAVSTAR satellites. This effect can be partially mitigated by using pulsed pseudolites, wherein the transmitted signal is pulsed at some prescribed duty cycle [CS97].

A reasonable value for the formation NDOP constraint, C , can be selected based on the desired positioning accuracy. The RMS position error is given by

$$PositionError = PDOP \times \sigma \quad (5.36)$$

under the assumption of uncorrelated, zero mean measurement errors with common RMS value σ [GPS96]. Making the same assumptions on the bias estimate errors, the RMS position error is then given by

$$PositionError = PDOP \times \bar{\sigma} \quad (5.37)$$

where

$$\bar{\sigma}^2 = \sigma_{bias}^2 + \sigma_{carrier}^2 \quad (5.38)$$

Using Eq. 5.32 and 5.33, σ_{bias}^2 is approximated as

$$\sigma_{bias}^2 \approx \frac{NDOP^2}{n_b} \sigma_{carrier}^2 \quad (5.39)$$

where n_b = number of biases

In this case, the measurement noise is a function of the resulting “bias noise”, and carrier-phase noise. The NDOP constraint, C , can be selected given the desired value for the RMS position error and the formation PDOP. As in the usual GPS positioning problem, the PDOP will vary as the satellites move about in their orbits, and as the vehicles move relative to one another (because of the onboard pseudolites). Given this variation, the PDOP may be evaluated using the positions of the GPS satellites, and vehicles at the start of the optimization.

Figure 5.3 shows a flow chart for the algorithm. The various parameters for the problem are determined in the formulation. These include the desired NDOP constraint, as well as constraints on minimum vehicle separation, etc. Since the carrier-phase data may only be collected at discrete times, and the control is implemented at a fixed sample rate, the total time of the maneuver is determined by the number of times steps, N , as $T_f = N \times t_s$, where t_s is the sample period. The optimization iterates on N (using bisection) until the minimum integer value is determined which still satisfies the NDOP constraint. The initial conditions for the optimization are generated using the quasi-optimal algorithm described in Section 5.7.

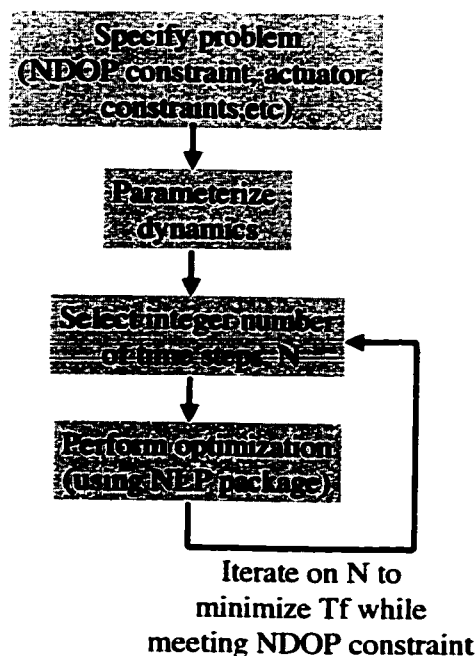


Fig. 5.3: Algorithm Flow Chart.

A sample problem was selected to demonstrate the optimization. The problem specifics (i.e. assumed GPS constellation, actuator constraints, starting configuration, etc.) are given in Appendix A.

Figure 5.4 shows a plot of the resulting LOS's between three vehicles as they undergo the optimized initialization maneuver. The plot is given in polar coordinates. The azimuth is shown in 45° increments, going from 0 - 360° . The elevation is $+90^\circ$ in the center, and -90° at the far edge, with increments of 20° . The "x"'s shown in the plot indicate the starting positions of the vehicles. For the optimization shown, there were constraints on the separation distances between the vehicles, actuator input, and final relative velocities. For simplicity, each vehicle was modeled as a rigid body. There were 7 GPS satellites commonly visible to each vehicle, as well as the onboard pseudolites on each vehicle. The optimization took well over an hour to compute when running on a Pentium Pro 200 computer using Matlab.

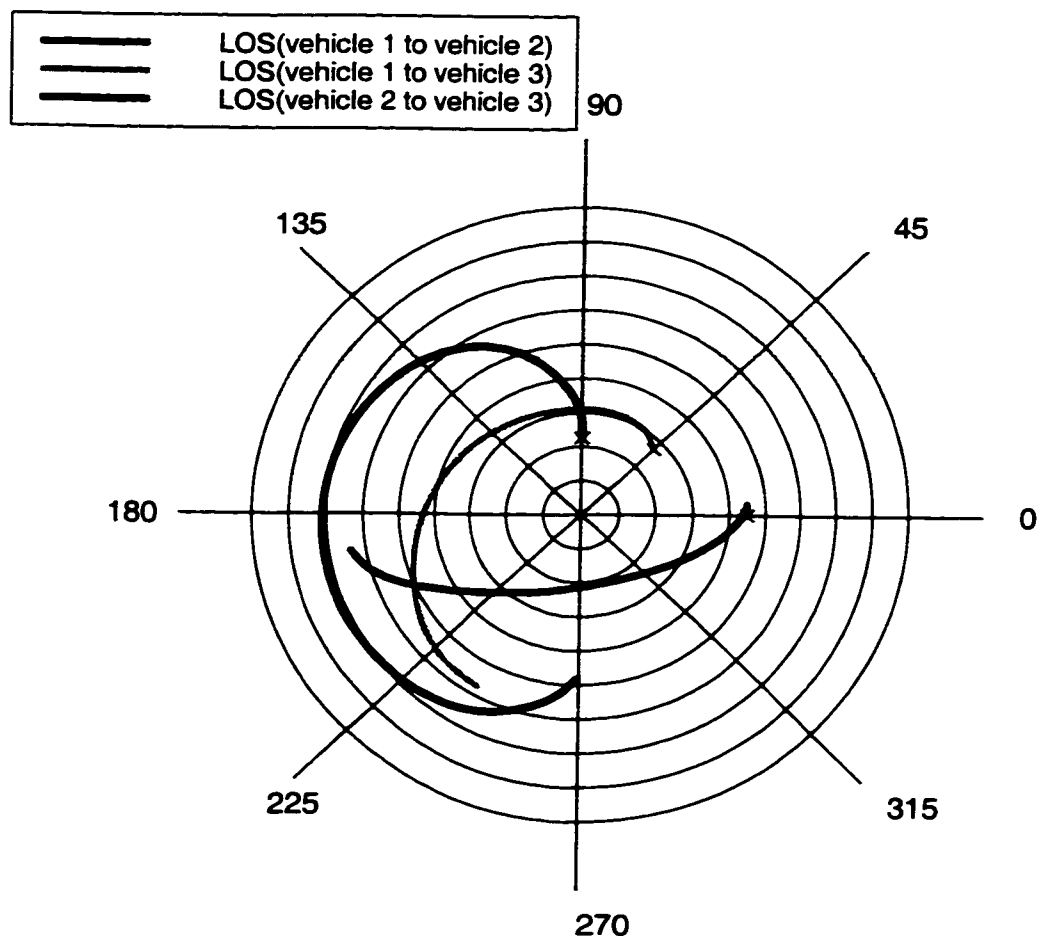


Fig. 5.4: LOS's between Vehicles for the Optimal Initialization Maneuver. The Azimuth is Shown in 45° Increments. The Elevation is $+90^\circ$ in the Center, and -90° at the Far Edge, with Increments of 20° .

Figures 5.5, and 5.6 show the 2-D projections of the same maneuvers. The o's are placed at 1 second intervals along the trajectories, and the vehicle start positions are at the x's located near 't = 0 sec' in the plot.

This optimal solution was compared to 5000 Monte Carlo simulations using the same starting configuration and problem constraints. In the Monte Carlo runs, each vehicle's path was a randomly oriented line in 3-space. Two angles (azimuth, and elevation) are required to specify the orientation of each path, and these angles were randomly generated. If the separation constraint would have been violated along

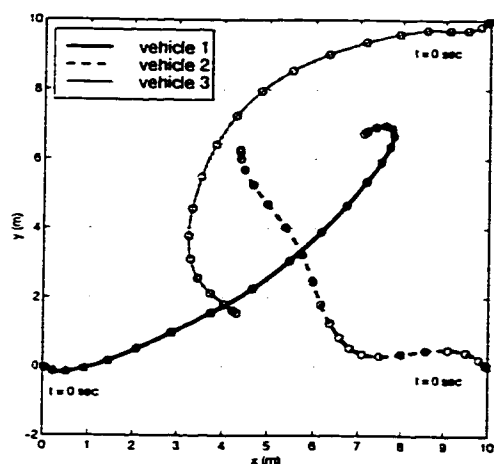


Fig. 5.5: Plot of X-Y Positions of Vehicles During Maneuvers. The Start Conditions Indicated by the 'x' Near 't=0 sec'. The 'o's are Placed at 1 Second Intervals.

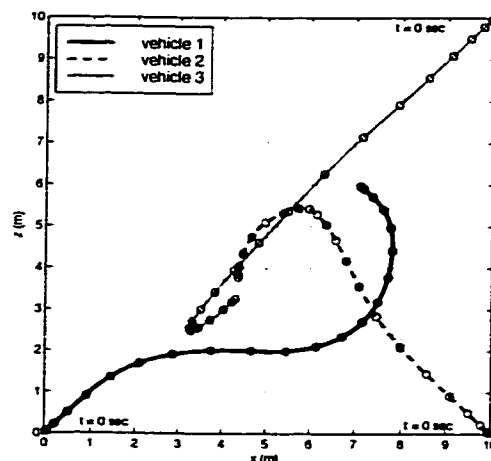


Fig. 5.6: Plot of X-Z Positions of Vehicles During Maneuvers. The Start Conditions Indicated by the 'x' Near 't=0 sec'. The 'o's are Placed at 1 Second Intervals.

these paths, a new set of randomly chosen angles was used. Each vehicle moved the maximal distance in the time interval calculated from the optimal solution. This resulted in the vehicles using a maximal thrust (max fuel) for the entire duration of the maneuver. The average NDOP for the Monte Carlo runs was in excess of 700 times larger than the optimal solution. Many of these maneuvers resulted in very limited observability. The best of 5000 Monte Carlo run had an NDOP that was 2.8 times larger than the optimal. The significant improvement that can be obtained using the optimal solution over non-optimal solutions provides additional motivation to formulate and solve this problem.

Figure 5.7 shows a typical LOS history from the Monte Carlo runs. Clearly visible in the plot is that the LOS change between the vehicles is not as large as in the optimized case. The large LOS change visible in the optimized solution, as compared

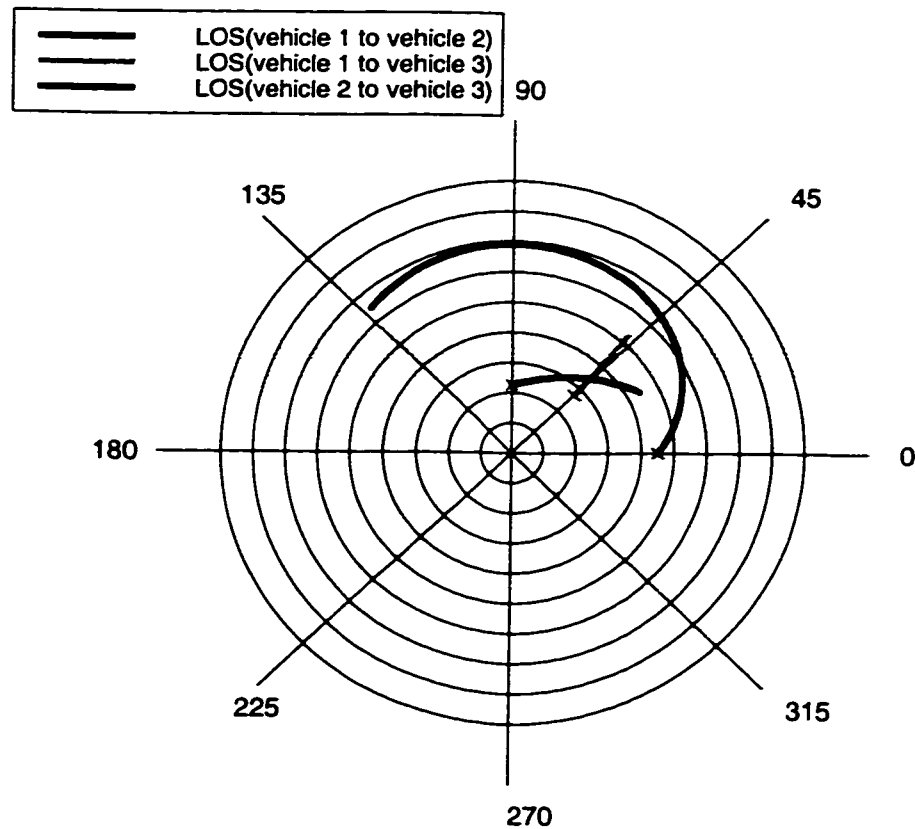


Fig. 5.7: LOS Between Vehicles for a Typical Monte Carlo Simulation. The Azimuth is Shown in 45° Increments. The Elevation is $+90^\circ$ in the Center, and -90° at the Far Edge, with Increments of 20° .

to the Monte Carlo run (sub-optimal) forms the basis for the quasi-optimal algorithm discussed in Section 5.7.

In calculating the optimal maneuver, and computing the resulting formation NDOP, it is implicitly assumed that the exact positions of the vehicles within the formation are known. This, of course, is not the case because centimeter-level positioning is not available until after the biases have been solved for – which is the point of undergoing the optimal maneuvers in the first place. The vehicles in the formation cannot undergo the exact optimal trajectories, but they can use the sensing available prior to initializing to attempt to perform a maneuver that is as close as possible to

the one desired. Also note that it is only the relative positions of the vehicles that matter, not their absolute positions. The sensing available includes:

1. Differential carrier-phase measurements provide very precise (< 1 deg) vehicle attitude (both relative and absolute) estimates [GPS96].
2. Pseudorange and carrier-phase rates provide absolute velocity measurements accurate to ≈ 0.4 m/s [VEL].
3. Differential carrier-phase rate measurements can be used to provide very precise (mm/s) relative velocity estimates without knowledge of the biases [MP96].
4. Differential code measurements do not require knowledge of the carrier-phase biases, and will be immediately available. It is also possible to use smoothed differential code measurements. This will provide meter-level relative position sensing during the initialization maneuver.
5. Differential carrier-phase measurements from the NAVSTAR satellites provide centimeter-level relative position *changes* (over the time scale of the maneuver, since the lines-of-sight to the NAVSTAR constellation remain essentially constant).

Coupling the available GPS sensing with the known vehicle models should allow the system to undergo maneuvers very close to the ones that have been designed. Of course, after any initialization maneuver has been completed, an estimate of the bias covariance will be available. If the covariance constraint was not met due to positioning errors during the maneuver, then further relative motion can be initiated. The sensing accuracies will degrade the initialization maneuver, but not substantially. The main point of the optimization is to generate trajectories that are “good” maneuvers to do – the Monte Carlo simulations indicate that it is easy to generate poor motions that will be costly in terms of time and fuel.

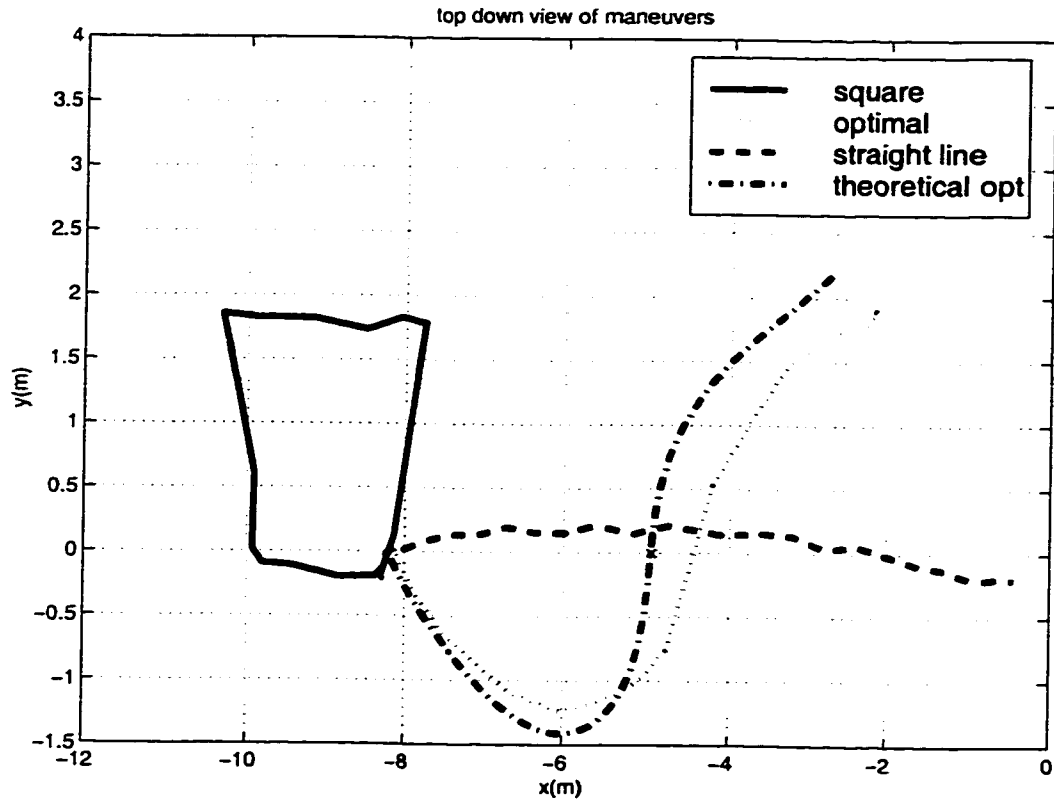


Fig. 5.8: Experimental Maneuvers in the Highbay for a Single Blimp Traversing Across the GPS Workspace. There were 8 Pseudolites Arrayed Around the Room, as well as a Pseudolite Placed on the Floor (Indicated in the Plot by the 'x' at $x \approx -5$ m, $y \approx 0$ m). The 'Theoretical Opt' Maneuver was Derived Mathematically, While the Other Maneuvers were Actual Trajectories by the Blimp

5.6 Experimental Initialization Maneuvers

An experiment was developed to test an optimized initialization maneuver, and compare it to several other non-optimal maneuvers. The ultimate objective is to have onboard transmitters on each vehicle and to demonstrate optimized initialization maneuvers. However, the current vehicles do not have the transmitters incorporated due to time, cost, and payload weight restriction constraints. The continuation of the formation flying project will be using RC trucks, since pseudolites can be easily incorporated onto these vehicles (see Chapter 8).

In order to develop an experimental demonstration, a fixed pseudolite was placed on the floor of the highbay to simulate another vehicle in the system (note that only relative motions are necessary to initialize, so this is a reasonable approximation of the system described in the previous section). Several 3-D initialization maneuvers within the highbay were generated for a single (movable) blimp, including the optimized initialization maneuver. For purposes of a fair comparison, each maneuver started at the same location in the highbay, and was constrained to be the same duration in the total distance traveled. In this case, each maneuver was 8 m long. The optimized maneuver was designed to minimize the resulting NDOP over the constrained path length.

Three maneuvers were performed: 1) The optimized maneuver (which was subjected to errors due to the sensing limitations described in the previous section); 2) An “intuitive” maneuver, which was a straight line fly-over of the ground based pseudolite; and 3) A “square” maneuver, which had the same cost (i.e. path length) as the other maneuvers.

Figure 5.8 shows a top down view of the three experimental maneuvers, and the theoretical optimum. The carrier-phase measurements from the onboard GPS receiver were collected while the blimp was in motion. The “x” visible in the plot (near $x = -5$, $y = 0$) is the location of the additional pseudolite placed on the floor of the highbay. There is a third dimension that is not shown in the figure, for the sake of clarity.

Table 5.2 summarizes the results of the 3 experimental maneuvers, and the theoretical optimum. A batch least squares algorithm was used to process the carrier-phase measurements collected during the maneuvers. The listed NDOP was computed from the resulting covariance. The true bias values were known since the blimp started

Table 5.2: Initialization Maneuver Statistics

Square Maneuver		Straight Line		Optimized Maneuver		Theoretical Maneuver	
NDOP	STD (cm)	NDOP	STD (cm)	NDOP	STD (cm)	NDOP	STD (cm)
7.4	15.3	4.0	7.4	2.1	5.0	1.7	4.25

at a known point within the highbay, and the experimental bias STD was calculated from post-processed data. The values of the NDOP and STD for the theoretical optimum are those resulting from the solution to the optimal problem. The value of the theoretical STD is given assuming a differential carrier-phase noise level of 2.5 cm (this value is consistent with the high levels of multipath associated with working indoors).

The data indicate that the optimized maneuver performed nearly as well as the theoretical optimum, despite the meter-level errors between the two that would be expected using the available sensing. The intuitive, straight line fly-over, performed twice as worse (as indicated by the NDOP), and the square maneuver did substantially worse. These results show the significant improvements that can be achieved by using properly designed trajectories, as opposed to poorly designed and even “intuitively” designed initialization maneuvers. Of course, it would be very difficult to even develop these intuitive solutions for a formation with a large number of vehicles.

5.7 Quasi-Optimal Initialization Maneuvers

One disadvantage of using the exact optimal control formulation is the computational effort required to calculate the maneuver. This is a result of the large scale of the problem, even for a modest number of vehicles, and the fact that it is not possible to

compute analytic gradients for the formation NDOP. As a result, it is not possible to compute the exact answer in real-time on currently available computers. In order to develop a solution that can be computed in real-time, several quasi-optimal algorithms were investigated. These simpler formulations allow a trade-off between run-time and accuracy.

5.7.1 Dynamic Formulation

One simple formulation is based on an observation that is true for the general initialization problem: LOS changes between vehicles and nearby pseudolites improve the bias initialization. Define

Δlos_{ij}^k = change in line-of-sight between vehicles i and j from epoch $k-1$ to k

The line-of-sight change between vehicles i and j from epoch $k-1$ to k is then computed as

$$\Delta\text{los}_{ij}^k = \arccos \frac{(P_i^{k-1} - P_j^{k-1})^T (P_i^k - P_j^k)}{\|P_i^{k-1} - P_j^{k-1}\| \|P_i^k - P_j^k\|} \quad (5.40)$$

where

P_i^k = position of vehicle i at epoch k (*i.e.* time $t = t_k$)

The objective can be quantified mathematically as

$$\max_{\mathbf{u}_k} \sum_{i,j, i>j} \Delta\text{los}_{ij}, \quad k = 1, \dots, q \quad (5.41)$$

subject to

$$\begin{aligned} \dot{x}_i &= f_i(x, u, t) && \text{-- dynamics} \\ NDOP &< C && \text{-- desired bias observability after maneuver} \\ \|u_i\| &< u_{\max} && \text{-- actuator constraints} \end{aligned}$$

where $i, j = 1, 2, \dots, n_v$ (n_v = number of vehicles), q = minimum number of epochs required to meet the NDOP constraint and

$$\bar{u}_k = \begin{bmatrix} u_1 \\ u_2 \\ \vdots \\ u_{n_v} \end{bmatrix} \quad (5.42)$$

The control at each epoch k , \bar{u}_k , is chosen to maximize the line-of-sight changes between the vehicles at that epoch, subject to actuator and dynamic constraints. The NDOP constraint is checked at every epoch, and the optimization is terminated once it is met. Note that the vehicle separation constraints are not directly part of the optimization as formulated above.

In the event that the separation constraint is violated, a separate optimization problem is run to minimize the perturbations to the control, $\Delta\bar{u}_k$, necessary to avoid the constraint violation. This may be formulated as

$$\min_{\Delta\bar{u}_k} \sum_k \|\Delta\bar{u}_k\| \quad (5.43)$$

subject to

$$\|p_i(t) - p_j(t)\| > d \quad - \text{minimum separation between vehicles } i \text{ and } j$$

Once the observability constraint is met, the relative positions of the vehicles will be known to cm-level accuracy. At this point, any additional state constraints (i.e. final relative positions or velocities) may be imposed by having the vehicles maneuver into the desired configuration. The optimization based on the LOS (Eq. 5.41) solves for the control at every epoch, without consideration of the future control history. Because of this, the process is not computationally demanding, and can be run in real-time for simple plants. Note that the vehicle separation constraints are unlikely to be violated when Eq. 5.41 is solved, because there is no LOS change when the vehicles move directly towards one another (i.e. the LOS change between two vehicles is *minimized* when they move directly towards one another). However, the separation constraint is imposed by solving Eq. 5.43 when necessary.

Another possible algorithm is based on replacing the cost function in Eq. 5.41 with

$$\min_{\bar{u}_k} NDOP \tag{5.44}$$

In this case, instead of maximizing the LOS changes at each epoch, the control is chosen to maximize the decrease in NDOP at every epoch. This formulation proceeds in the same manner as above.

5.7.2 Way-Point Formulation

A significant disadvantage of both the exact optimal, and quasi-optimal algorithms given in the previous section is that they become intractable for complex plants.

Additionally, it may not be reasonable or even desirable to send low-level control commands to every vehicle in the system.

A practical approach that overcomes these limitations is to generate “way-points” for the vehicles within the formation. A way-point is defined as a point in space to which the vehicle is directed. A series of way-points then determine the basic trajectory. Each vehicle maneuvers through its assigned way-points during the initialization process. This offers several advantages:

1. The initialization algorithm only sends high-level commands (i.e. move to the next way-point) to each vehicle. The actual control inputs are computed by the vehicle controllers.
2. The way-points can be quickly computed by the path planner.

The algorithm is similar to the quasi-optimal formulation in the previous section, in that a series of way-points are generated in order to maximize the LOS change between the vehicles during the initialization maneuver.

Define

W_i^k = k th way-point for vehicle i , way-point W_i^0 is the estimated starting location of vehicle i .

Δlos_{ij}^k = change in line-of-sight between vehicles i and j as they maneuver from W_i^{k-1} to W_i^k , and from W_j^{k-1} to W_j^k , respectively

The line-of-sight change between the vehicles i and j is then computed as

$$\Delta \text{los}_{ij}^k = \arccos \frac{(W_i^{k-1} - W_j^{k-1})^T (W_i^k - W_j^k)}{\|W_i^{k-1} - W_j^{k-1}\| \|W_i^k - W_j^k\|} \quad (5.45)$$

The vehicle dynamics are important to the problem because the *relative* positions of each vehicle during the entire course of the maneuver determine the resulting

NDOP, as well as their separations. In order to simplify the problem, two reasonable approximations to the dynamics can be made. The approximations are:

1. The average speed, $S_{avg_i}^k$, of each vehicle between way-points can be specified based on the known vehicle models.
2. The ability of vehicle i to maneuver can be simply modeled by constraining the azimuth (az_i^k), and elevation (el_i^k) angle change between adjacent legs in the trajectory. A leg is the path formed between two consecutive way-points, W^{k-1} and W^k . For example, vehicle i starts the maneuver at way-point W_i^0 (by definition), and then moves to the first way-point, W_i^1 . The first leg is the straight line path between W_i^0 and W_i^1 . The azimuth (az_i^k) and elevation (el_i^k) angles associated with the leg formed by W_i^{k-1} and W_i^k are computed as

$$az_i^k = \arctan 2 \left(los2_i^k, los1_i^k \right) \quad (5.46)$$

$$el_i^k = \arcsin \left(los3_i^k \right) \quad (5.47)$$

where

$$\begin{bmatrix} los1_i^k \\ los2_i^k \\ los3_i^k \end{bmatrix} = \frac{(W_i^k - W_i^{k-1})}{\|W_i^k - W_i^{k-1}\|} \quad (5.48)$$

The second approximation allows parameters to be selected in order to constrain the placement of the way-points in a reasonable way. For example, if the two legs formed by W_i^{k-1} , W_i^k , and W_i^{k+1} are parallel, then the vehicle would continue in a straight line after traversing through W_i^k . However, if the two legs formed by W_i^{k-1} , W_i^k , and W_i^{k+1} were perpendicular, the vehicle would have to begin making a sharp turn after traversing through W_i^k . Tightening the bounds on changes in az_i^k ,

and el_i^k will effectively smooth out the trajectories. In the degenerate case of $el_i^k = 0$, $k = 1, 2, \dots, N$ the trajectory would be constrained to the 2-D case (i.e. ground vehicles).

The change in azimuth and elevation angle between adjacent legs is given by

$$\Delta el_i^k = |el_i^k - el_i^{k-1}| \quad (5.49)$$

$$\Delta az_i^k = |az_i^k - az_i^{k-1}| \quad (5.50)$$

The total duration of the initialization maneuver, t_{init} , is given by

$$t_{init} = N \times t_{leg} \quad (5.51)$$

where N is the number of way-points, and t_{leg} is time of traversal between consecutive way-points, W^{k-1} to W^k .

The assumption here is that each vehicle moves from W^{k-1} to W^k in the same time, t_{leg} . This does not impose a constraint, because the distances between way-points will vary from vehicle to vehicle depending on the vehicle's average speed as it traverses the trajectory.

Define the following

$S_{avg_i}^k$ = average speed of vehicle i as it traverses from W_i^{k-1} to W_i^k ,

t_{min} = minimum allowable time of traversal from W_i^{k-1} to W_i^k ,

$\Delta az_i^k_{max}$ = maximum allowable change in azimuth angle, Δaz_i^k ,

$\Delta el_i^k_{max}$ = maximum allowable change in elevation angle, Δel_i^k

The parameters $S_{avg_i}^k$, t_{min} , $\Delta az_i^k_{max}$, and $\Delta el_i^k_{max}$ are specified at the start of the optimization. The parameter t_{min} is a constraint on t_{leg} , and impacts how close the

adjacent way-points are too close to one another. For example, in the blimp testbed, the speed of each vehicle can be maintained at a maximum of about 0.1 m/s when performing maneuvers. In this case, for $t_{leg} \approx 5$ sec, the way-points would only be separated by 0.5 m. In practice, it is not reasonable to have a large number of way-points clustered closely together. Instead, a smaller number of way-points, separated by larger distances should be used. This constraint has the practical effect of bounding the number of way-points in the solution of the quasi-optimization.

The optimization solves for the way-points for each vehicle in order to minimize t_{init} (the initialization maneuver time). The algorithm is described as follows.

Step 1: Select the problem parameters, $S_{avg_i}^k$, t_{min} , C (NDOP constraint), d (separation constraint between vehicles), Δaz_i^k , and Δel_i^k

Step 2: Select a value for t_{leg} , set $N = 1$,

Step 3: Solve the following problem for W_i^N , given W_i^z ($z = 1, 2, \dots, N-1$), $i, j = 1, 2, \dots, n_v$ (n_v = number of vehicles),

$$\max_{W_i^N} \sum_{i,j,i>j} \Delta \text{los}_{ij}^N \quad (5.52)$$

subject to

$$\|W_i^N - W_i^{N-1}\| = S_{avg_i}^N \times t_{leg} \quad - \text{way-point constraint}$$

$$\|p_i(t) - p_j(t)\| > d \quad - \text{separation constraint}$$

$$\Delta az_i^N < \Delta az_i^N_{\max}, \quad - \text{dynamic constraint}$$

$$\Delta el_i^N < \Delta el_i^N_{\max}, \quad - \text{dynamic constraint}$$

The formulation solves for the way-points that maximize the line-of-sight change between the vehicles while meeting the constraints.

Step 3a: If the problem in step 3 is infeasible (which is possible if a collision is impossible to avoid), set $W_i^N = W_i^{N-1} + \bar{u}_i \times S_{avg_i}^N$, $i = 1, 2, \dots, n_v$, and solve

$$\max_{\bar{W}_i^k} LOS_{new} \quad (5.53)$$

subject to

$$\begin{aligned} \|\bar{W}_i^k - \bar{W}_i^{k-1}\| &= S_{avg_i}^k \times t_{leg} && \text{- way-point constraint} \\ \|p_i(t) - p_j(t)\| &> d && \text{- separation constraint} \\ \Delta az_i^k &< \Delta az_{i \max}^k, && \text{- dynamic constraint} \\ \Delta el_i^k &< \Delta el_{i \max}^k, && \text{- dynamic constraint} \end{aligned}$$

where

$$\bar{u}_i = \frac{W_i^{N-1} - W_i^{N-2}}{\|W_i^{N-1} - W_i^{N-2}\|} \quad (5.54)$$

$$\bar{W}_i^k = W_i^k + \bar{W}_i^k \quad (5.55)$$

$$LOS_{new}(\bar{W}_i^k) = \sum_{k=1}^N \sum_{i,j,i>j} \Delta los_{ij}^N \quad (5.56)$$

The perturbations, \bar{W}_i^k , to the current set of way-points, W_i^k , are determined so that the separation constraint is met. The cost is the line-of-sight change using the new set of way-points. In effect, the way-points are perturbed in order to met the imposed vehicle separation constraint.

Step 4: Calculate the NDOP for the maneuvers given the set of way-points.

Step 5: If $NDOP > C$, set $N=N+1$. The current set of way-points (W_i^k , $i = 1, 2, \dots, n_v$, $k = 1, 2, \dots, N-1$) are kept. Go to step 3. If $NDOP < C$, go to step 6.

Step 6: Determine the value of t_{init} . The initialization time will depend on the value of t_{leg} , as well as N . If a locally minimum value of t_{init} has been found, stop.

Table 5.3: Quasi-Optimal Initialization

t_{leg}/t_{opt}	N	cost(rad)	NDOP/ C	t_{init}/t_{opt}
0.48	4	17.6	0.98	1.92
0.58	3	20.7	0.95	1.74
0.67	3	14.4	0.86	2.01
0.76	3	18.2	0.80	2.28
0.86	2	16.7	0.93	1.72
0.95	3	27.9	0.66	2.85

Otherwise, iterate on t_{leg} (bisection can be used, or set $t_{leg} = t_{leg} + \lambda$, where λ is a selectable parameter), and go back to Step 2.

The algorithm will determine the minimum number of way-points, N , such that the NDOP constraint is met for a given value of t_{leg} . The value of t_{leg} is also iterated on, such that the minimum value of t_{init} is determined.

The same problem described in Section 5.5 was solved using the quasi-optimal algorithm. The problem specifics are given in Appendix A. Table 5.3 summarizes the results of the iterations on t_{leg} . Each iteration took a couple of minutes in Matlab on a Pentium Pro computer, but could be made to run substantially faster with properly optimized C code. The table shows the following

1. The values of t_{leg} used (in units of the exact optimal time solution, t_{opt}).
2. The number of way-points required, N , to reduce the NDOP below the constraint, C .
3. The cost, which is the change in lines-of-sights among the vehicles.
4. The calculated NDOP, based on $S_{avg_i}^k$, and W_i^k .
5. The resulting initialization time, t_{init} .

The quasi-optimal solution results in a maneuver which should take about 1.7 times longer than the true optimum. Note that the resulting bias visibility (parameterized by NDOP) is not necessarily proportional to the cost. In particular, it is possible for a maneuver to have a better NDOP, even though the line-of-sight change among the vehicles was smaller than another maneuver. However, the LOS change does provide a good measure of the observability, and it is computed quite easily. The optimum times are somewhat insensitive to t_{leg} . For this reason, a single value of t_{leg} could be used to generate the solution for implementation in real-time.

The problem formulation is highly nonlinear, and the solutions shown in the table are local optimum. As with most nonlinear optimization problems, there is no guarantee that the global optimum will be found (unless the problem is convex). The solutions are dependent on the initial guess. A good initial guess for the first set of way-points can be derived by having the vehicles move towards each other.

Figure 5.9 shows a comparison of all three quasi-optimal algorithms with the exact optimal formulation for the problem described in Section 5.5. It is important to have the optimal solution in order to make a comparison and validate the quasi-optimal algorithms. The plot is normalized time (normalized to the optimal time solution) vs. normalized NDOP (normalized to the NDOP constraint, C). In this case, the value of (1,1) represents the optimal solution. Figures 5.10, and 5.11 show the 2D projections of the way-point maneuver, and Figure 5.12 is a plot of the LOS change among the vehicles.

Figure 5.9 shows the NDOP as a function of time as the vehicles performed their prescribed maneuvers. As expected, the quasi-optimal algorithms did not perform as well as the exact solution. However, the way-point algorithm did substantially better than the other quasi-optimal algorithms, and as discussed earlier, way-points are a

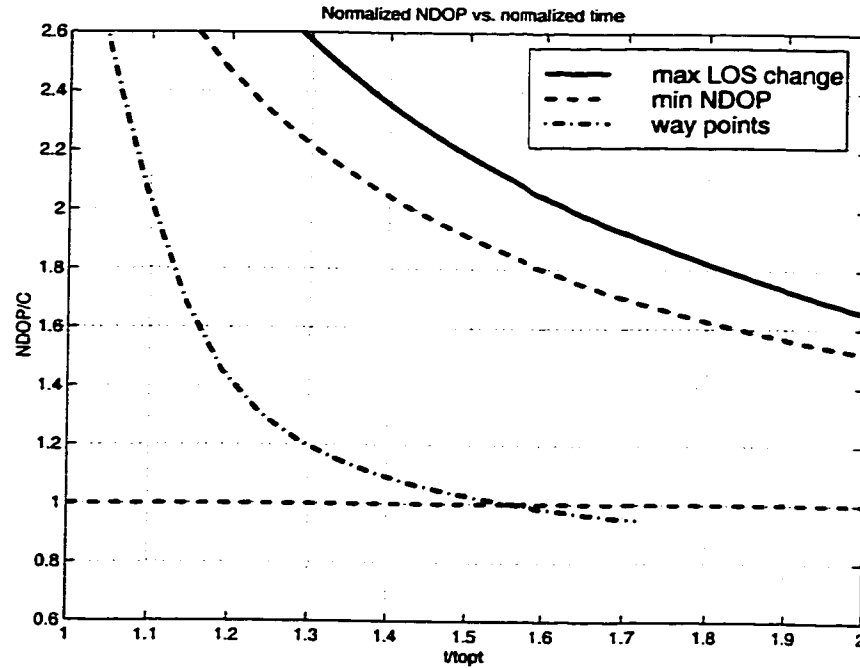


Fig. 5.9: Algorithm Comparison Plotted as Time Normalized by the Optimal Time vs NDOP Normalized by the Constraint Value. (1,1) Corresponds to the Optimal Solution.

more practical solution to the problem. Note that the way-point maneuver exceeded the NDOP constraint as the vehicles traversed between way-points, and actually performed slightly better than the algorithm predicted. If the NDOP constraint had not been met when the vehicles reached their final destinations, another set of way-points would be added in order to initiate further relative motion.

In order to implement the algorithm, the vehicles in the cluster must make use of all the GPS sensing available (Section 5.5). The way-points are specified in (X_I, Y_I, Z_I) , but only their *relative* positions are important. The heading, and speed of each vehicle can be accurately determined in absolute coordinates, which will allow the vehicles to follow their assigned routes. However, whether or not each vehicle reaches its prescribed way-point is not important. The transition of each vehicle from

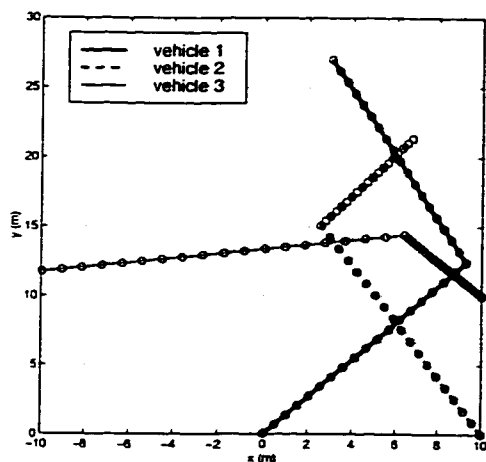


Fig. 5.10: Plot of X-Y Positions of Vehicles During Maneuvers. The Start Conditions Indicated by the 'x' Near 't=0 sec'. The 'o's are Placed at 1 Second Intervals.

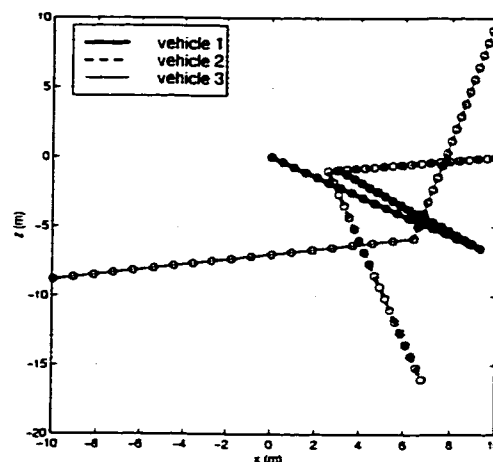


Fig. 5.11: Plot of X-Z Positions of Vehicles During Maneuvers. The Start Conditions Indicated by the 'x' Near 't=0 sec'. The 'o's are Placed at 1 Second Intervals.

one leg to another is based on the desired *relative* position of each vehicle (which is determined by the relative positions of the way-points).

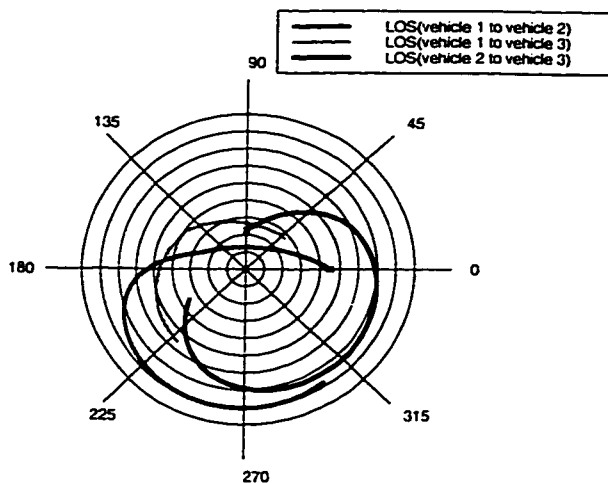


Fig. 5.12: LOS's Between Vehicles for the Way-Point Initialization Maneuver. The Azimuth is Shown in 45° Increments. The Elevation is +90° in the Center, and -90° at the Far Edge, with Increments of 20°.

~

Chapter 6

Formation Flying Algorithms

Several new algorithms for use in a formation flying application are presented. In particular, the effects of the polarization of the GPS signal were analyzed for the blimp testbed, and a method to account for this term, along with a convergence proof is presented. The “all-baselines-in-view” measurement formulation, which was developed and implemented experimentally on the blimp testbed to increase system robustness, is given. Finally, a concept termed “pseudolite aided attitude” (PAA) is described. PAA will allow a vehicle to determine its attitude with only two working antennas, and will therefor increase the robustness of the attitude estimation.

6.1 Polarization

6.1.1 Magnitude

The electric field of the GPS signal is circularly polarized [CB82], and will result in an additional term in the general carrier-phase measurement equation 4.1. This term cancels out in the difference equations when the satellites are in the far field, and the

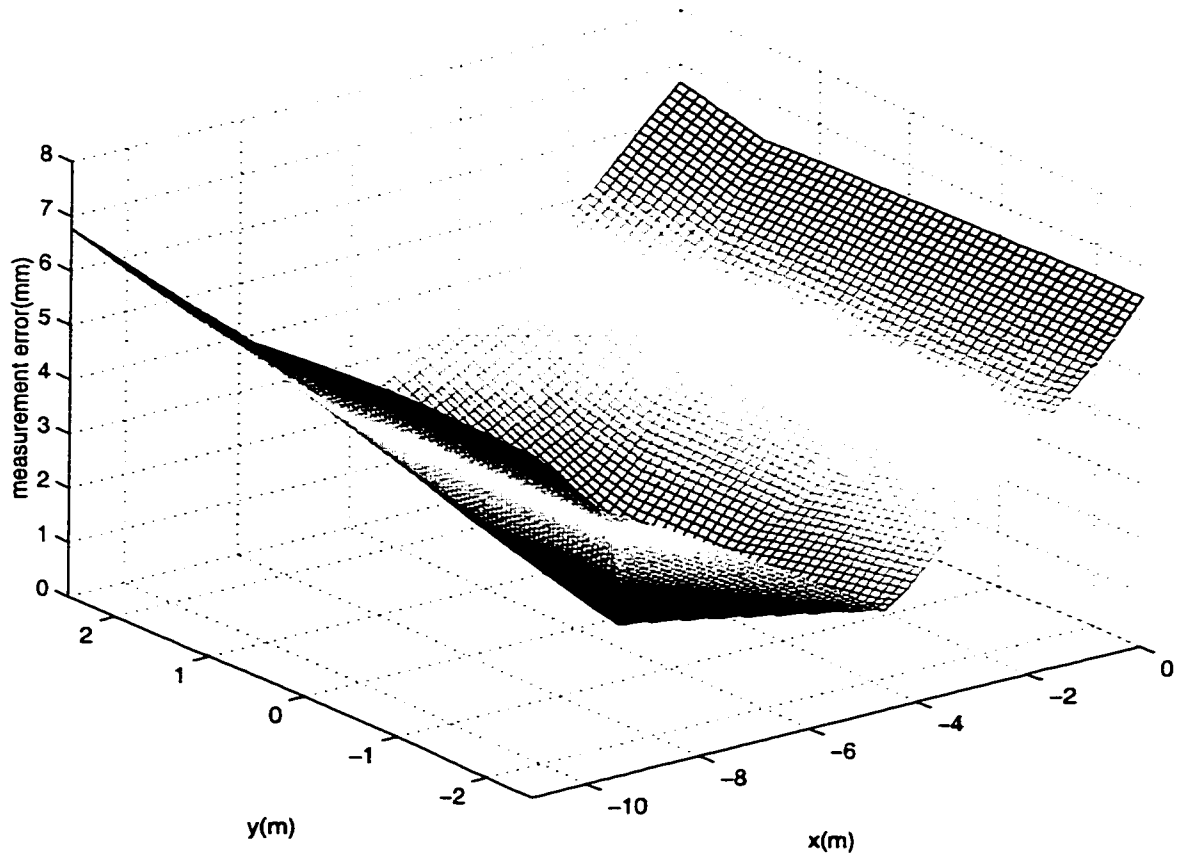


Fig. 6.1: Maximum Polarization Component to the Double Difference Carrier-Phase Measurements within the Highbay GPS workspace. The Polarization Component was Computed from the Model Given in Adams [JCA99], and was Evaluated Over the Workspace at Grid-Points Separated by 0.1 m.

bore-sites of all the antennas in the system are parallel [DL96]. However, this is not true for the non-aligned antenna case [JCA99] and the formation flying application, since the line-of-sights to the GPS satellites in the antenna frames will vary from vehicle to vehicle (*i.e* the bore-sites are not parallel). A model of the polarization, and its effect on the measured carrier phase can be derived based on the known line-of-sights to the transmitters, and the antenna orientation [JCA99,JW91]. A complete description of the polarization error source may be found in Adams [JCA99].

In the case of general vehicle motions, the polarization component of the measured carrier-phase is large enough that it needs to be accounted for in the state estimate [JCA99]. However, the blimp vehicles are constrained to operate within a relatively small GPS workspace within the highbay. Further, the roll and pitch of each vehicle remains small throughout the standard maneuvers. For this reason, the maximum measurement error that results from ignoring the polarization is small (see Figure 6.1) when the blimps are in actual operation. Figure 6.1 is a plot of the maximum double difference carrier-phase measurement error that results from neglecting polarization within the workspace. The error was evaluated over an $11 \text{ m} \times 5 \text{ m}$ box on the workspace floor within the highbay. An altitude of 2 meters was assumed, which was the nominal height of the blimps during operation. A meter-level change in altitude results in an insignificant change in the polarization magnitudes. The results in Fig 6.1 indicate that the maximum error relative to the center of the workspace is bounded by 7-8 mm, and is smaller than that for most of the experimental maneuvers. Note that the error is actually smaller than that observed in the 2-D testbed [KZ96]. This is because the perturbations in the line-of-sights to the pseudolites are larger in the 2-D testbed, primarily because the vehicles are so close to the pseudolites. The polarization component was not incorporated into the real-time estimator, as it is on the same order as the receiver phase noise.

Figure 6.2 shows a simulation of the relative position error over the course of a large scale maneuver (i.e. the maneuver would have been outside GPS workspace, resulting in larger measurement errors) within the highbay during which the effects of polarization were ignored in the state estimation. The maneuver consisted of a blimp traversing one loop of a helix (radius 10 m) around a stationary vehicle. The blimp started and ended at the same absolute X, and Y coordinate, but gained 3 meters

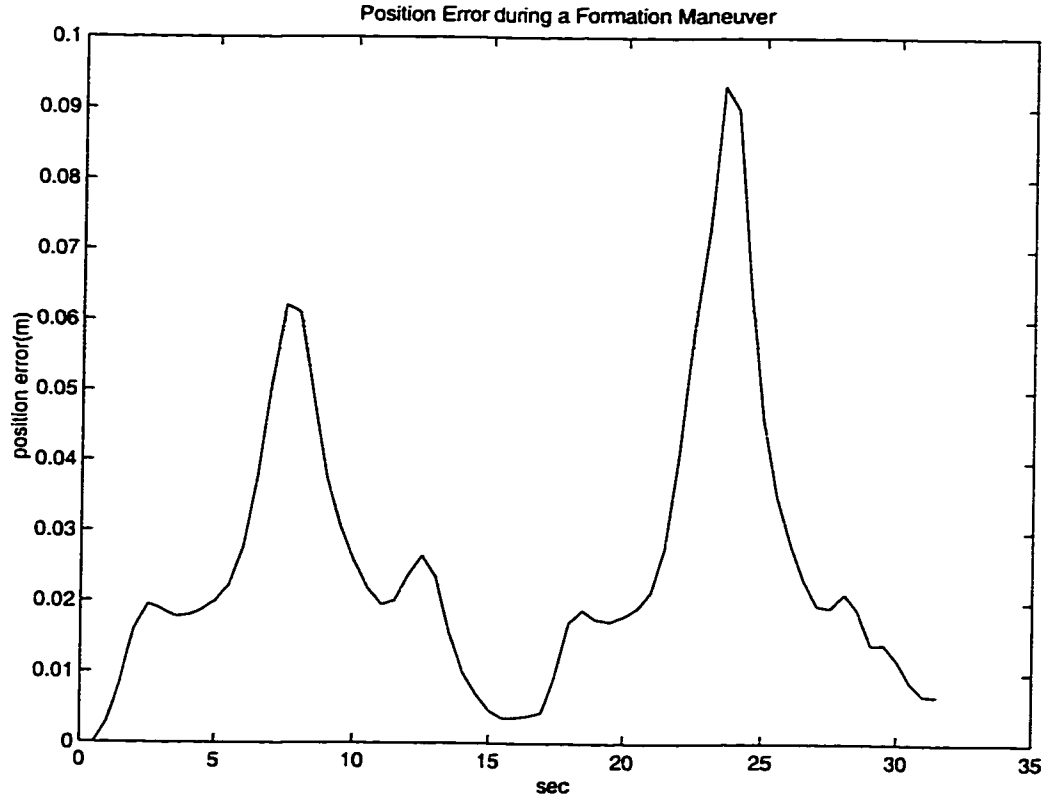


Fig. 6.2: Predicted Blimp Position Error Due to Polarization Effects.

in altitude. In the simulated motion, the errors in position were large enough that the polarization should be taken into account. This will be the case for the general formation flying problem as well.

6.1.2 State Solution Incorporating Polarization Term

The state estimate, incorporating the effects of polarization, can be estimated as follows. The general measurement equation, Eq. 4.26, is first rewritten as

$$y = h(x) + \nu = h_p(x) + h_d(x) + \nu \quad (6.1)$$

where $h(x)$ is the general measurement vector, $h_d(x)$ is the portion of the differential carrier-phase measurement due to distance, and $h_p(x)$ is the portion of the measurement due to polarization. It is assumed that the biases are known, and therefore arbitrarily set to zero. A gradient search algorithm, or more sophisticated methods such as an EKF, can be used to solve for the state.

The gradient search proceeds as follows. Linearize Eq. 6.1 about some guess \hat{x}

$$\rho = y - (h_p(\hat{x}) + h_d(\hat{x})) = H(\hat{x})\delta x + \nu \quad (6.2)$$

where $H = H_p + H_d = \partial h_p / \partial x + \partial h_d / \partial x$ is the Jacobian. The solution is found by iterating

$$\delta x = (H^T H)^{-1} H^T \rho \quad (6.3)$$

$$x_{\text{new}} = x_{\text{old}} + \delta x \quad (6.4)$$

Although this approach works, the calculation of $H_p = \partial h_p / \partial x$ is very computationally demanding, and the analytic expressions for the Jacobian are difficult to compute [JCA99].

An alternative approach¹ is based on the observation that $\|H_p\| < \|H_d\|$. Intuitively, the descent direction is primarily determined by the Jacobian of the distance dependent term, h_d . Thus, instead of computing H_p , an alternative is essentially to calibrate the polarization effect out of the measurement.

$$y - h_p(\hat{x}) = h_d(x) + \nu \quad (6.5)$$

¹Joint work with Carl Adams [JCA99]

The state is then determined iteratively by solving

$$\begin{bmatrix} y - h_p(\hat{x}) \end{bmatrix} - h_d(\hat{x}) = \hat{\rho} = H_d \delta x \quad (6.6)$$

$$\delta x = (H_d^T H_d)^{-1} H_d^T \hat{\rho} \quad (6.7)$$

$$x_{\text{new}} = x_{\text{old}} + \delta x \quad (6.8)$$

Simulations on the formation flying testbed show that this revised algorithm converges quickly (typically in 2–3 iterations), and it avoids the expense of storing and computing H_p . Note the difference between the iterations given by Eq. 6.3 and 6.7. Eq. 6.3 contains the Jacobian for the polarization term, whereas it is neglected in Eq. 6.7. In effect, only the dominant term is retained.

A derivation of the sufficient conditions for stability of a gradient descent search wherein a portion of the Jacobian is neglected when computing the descent direction is derived as follows. In regards to the polarization problem, the Jacobian of the polarization model ($H_p = \partial h_p / \partial x$) is neglected, and it is instead calibrated out of the total measurement. To proceed, define

$$y(x) = y_d(x) + y_p(x) = h_d(x) + h_p(x) \quad (6.9)$$

where $y_d(x)$ is that portion of the measurement due to distance, and $y_p(x)$ is that portion of the measurement due to polarization. The bias is assumed known, and arbitrarily set to zero.

The Taylor Series expansion of $y_d(x) = h_d(x)$ and $y_p(x) = h_p(x)$ about some point \hat{x} is

$$y_d(x) = y_d(\hat{x}) + \Delta y_d = h_d(\hat{x}) + H_d(\hat{x}) \Delta x + \mathcal{O}(\Delta x) \Delta x = h_d(\hat{x}) + \overline{H_d} \Delta x \quad (6.10)$$

$$y_p(x) = y_p(\hat{x}) + \Delta y_p = h_p(\hat{x}) + H_p(\hat{x})\Delta x + \mathcal{O}(\Delta x)\Delta x = h_p(\hat{x}) + \overline{H}_p\Delta x \quad (6.11)$$

where $H_d = \partial h_d / \partial x$ and $H_p = \partial h_p / \partial x$. Using just the expansion of the distance component of the measurement, $y_d(x)$, the least squares solution is

$$\Delta x = ([H_d + \mathcal{O}(\Delta x)]^T [H_d + \mathcal{O}(\Delta x)])^{-1} [H_d + \mathcal{O}(\Delta x)]^T \Delta y_d = (\overline{H}_d^T \overline{H}_d)^{-1} \overline{H}_d^T \Delta y_d \quad (6.12)$$

Let \hat{x}_i denote the estimated state at the i th iteration, and x_1 the truth state. We now perform the calibration step, so that

$$\Delta y_i = y(x_1) - [y_d(\hat{x}_i) + y_p(\hat{x}_i)] = \Delta y_{di} + \Delta y_{pi} \quad (6.13)$$

In this case, the updated estimate is given by the following, where $\overline{\Delta x_i}$ is the change in the state estimate computed at the i th iteration

$$\hat{x}_{i+1} = \hat{x}_i + \overline{\Delta x_i} = \hat{x}_i + (\overline{H}_d^T \overline{H}_d)^{-1} \overline{H}_d^T \Delta y_i \quad (6.14)$$

$$= \hat{x}_i + (\overline{H}_d^T \overline{H}_d)^{-1} \overline{H}_d^T (\Delta y_{di} + \Delta y_{pi}) \quad (6.15)$$

Then,

$$\Delta x_{i+1} = x_1 - \hat{x}_{i+1} = x_1 - \hat{x}_i - (\overline{H}_d^T \overline{H}_d)^{-1} \overline{H}_d^T (\Delta y_{di} + \Delta y_{pi}) \quad (6.16)$$

$$= \Delta x_i - (\overline{H}_d^T \overline{H}_d)^{-1} \overline{H}_d^T (\Delta y_{di} + \Delta y_{pi}) \quad (6.17)$$

The estimation converges if the sequence $\|\Delta x_i\|$ converges, and this convergence can be demonstrated if $\|\Delta x_i\| > \|\Delta x_{i+1}\|$, $\forall i > n$. This condition is equivalent to

requiring that

$$\|\Delta x_i\| > \|\Delta x_i - (\overline{H_d^T H_d})^{-1} \overline{H_d^T} (\Delta y_{di} + \Delta y_{pi})\|, \quad \forall i > n \quad (6.18)$$

for some n . Now, using Eqs. 6.12 and 6.13, this condition can be rewritten as

$$\|\Delta x_i\| > \|(\overline{H_d^T H_d})^{-1} \overline{H_d^T} \Delta y_{pi}\| \quad (6.19)$$

Using Eq. 6.11, then Eq. 6.19 becomes

$$\|\Delta x_i\| > \|(\overline{H_d^T H_d})^{-1} \overline{H_d^T} \overline{H_p} \Delta x_i\| \quad (6.20)$$

using standard properties of the norm, the sufficient condition then becomes

$$\|\Delta x_i\| > \|(\overline{H_d^T H_d})^{-1} \overline{H_d^T} \overline{H_p}\| \cdot \|\Delta x_i\| \quad (6.21)$$

or, if

$$\|(\overline{H_d^T H_d})^{-1} \overline{H_d^T} \overline{H_p}\| < 1 \quad (6.22)$$

Then, in the limit, as $\Delta x_i \rightarrow 0$, the sufficient condition becomes

$$\|(H_d^T H_d)^{-1} H_d^T H_p\| < 1 \quad (6.23)$$

At any point where Eq. 6.23 is satisfied, there is a region about that point where the algorithm will be stable. The conditions on H_d and H_p are always met when the antenna baselines are more than a few centimeters [JCA99]. The difficulty remains, of course, to obtain an initial estimate that ensures that Δx_1 will be sufficiently small.

6.2 All-Baseline-in-View

One approach to the measurement formulation based on defining a “master” antenna on each vehicle in the formation was developed and implemented on the 2D testbed by Zimmerman [KZ96]. This formulation was based on double differences, but can be applied to single differences without modification. In that approach, the differences between the vehicles in the formulation were based on the signals that were available on the “master” antenna only. The principle advantage of this approach is that the necessary bookkeeping is greatly simplified, especially for the system implemented with double differences. The principle disadvantage of this approach is that there is no guarantee that all the signals will be present on the specified master antenna. In fact, the 2D testbed suffered from signal outages on the master antennas at an alarming rate [TC99]. This resulted in difficulty maintaining a sufficient number of independent measurements with which to compute the relative positions. As a result, the system robustness is quite poor, and the 2D testbed has difficulty operating over extended periods of time.

In order to mitigate the effects of multipath and improve the system robustness, an “all-baseline-in-view” formulation was implemented for both the vehicle attitude and relative positioning problem on the blimp testbed. Figure 6.3 shows a top down view of the antenna arrays for two vehicles. Each vehicle has three antennas, labeled 1–3, but the specific number or numbering is not important. The measurement formulation is separated into two components: i) attitude and ii) relative positioning.

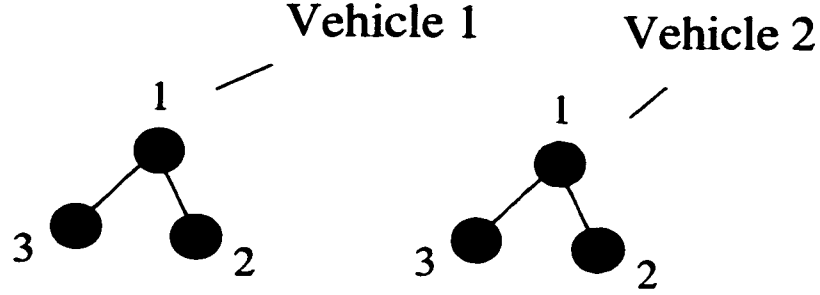


Fig. 6.3: Top Down View of Antenna Arrays

6.2.1 Attitude

For the system shown in Figure 6.3, each vehicle is arbitrarily designated as having a “master” antenna (labeled antenna 1). The principle baselines are then formed using the “master” antenna and the other antennas on the vehicle. For the three antenna system shown in the figure, these are represented by the antenna pairs (1,2), and (1,3). For an N antenna array, there will be $N-1$ principle baselines. The secondary baselines are formed using the antenna pairs exclusive of the master antenna. For the example in Figure 6.3 this baseline is formed from the antenna pair (2,3). For an N antenna system the number of secondary baselines is given by

$$\binom{N-1}{2} \quad (6.24)$$

which accounts for all possible baselines exclusive of the master antenna. Using Eq. 4.1, single differences are formed across the principle baselines of vehicle i using the commonly visible GPS signals (Eq. 4.2)

$$\Delta\phi_{i12k} = |P_{i1k}| - |P_{i2k}| + \beta_{i12k} + \nu_{i12k} \quad (6.25)$$

$$\Delta\phi_{i13k} = |P_{i1k}| - |P_{i3k}| + \beta_{i13k} + \nu_{i13k} \quad (6.26)$$

After the measurements are formed across the principle baselines, the measurements made using the secondary baselines are added to the total system measurement formulation if they are independent of the previously included baseline measurements. This ensures that the maximum possible number of independent measurements are included in the attitude formulation.

6.2.2 Relative Positioning

Similar to the attitude problem, each vehicle in the formation is designated as having a “master” antenna (labeled antenna 1), and one of the vehicles in the formation is designated as the “master” vehicle (labeled m). The antennas exclusive of the “master” on each vehicle are designated as secondary antennas. The principle baselines for the formation are those between *vehicle* m and *vehicle* i , and the secondary baselines are those made between the other vehicles, exclusive of vehicle m . Again, similar to the attitude problem, for an N vehicle formation the total number of secondary baselines is given by

$$\binom{N-1}{2} \quad (6.27)$$

For the relative position problem, single differences are formed between the principle baselines using the available signals. The differences are made using the “master” antenna on each vehicle, unless the signal is not present, at which point secondary antennas on the given vehicle are be used. The difference between antenna j on vehicle i , and antenna e on vehicle f using transmitter signal k is given by (Eq. 4.3)

$$\Delta\phi_{ijfek} = |P_{ijk}| - |P_{fek}| + \beta_{ijfek} + \tau_{vi} - \tau_{vf} + \nu_{ijfek} \quad (6.28)$$

After the measurements across the principle formation baselines are formed, the measurements using the secondary baselines are included in the estimation if they are independent of the previously included measurements. This ensures that the maximal number of independent measurements are available, regardless of which antenna is used on each vehicle. Note that this formulation requires knowledge of each vehicle's attitude, since it is possible that the inter-vehicle single differences between any two vehicles will be formed using various antenna pairs. This couples the solution of the relative position problem to the attitude, but attitude decouples from the relative position problem.

This one-way coupling does not present a difficulty because the attitude biases are much simpler to compute as a result of the known baseline constraints between the antennas on each vehicle. As such, we can assume that the attitude on each vehicle will be known prior to solving for the relative position of the vehicles in the formation.

6.3 Measurement Vector Re-formulation

As discussed in Section 6.2, the particular antennas being used to form the differences in Eq. 4.17 and Eq. 4.25 will vary as measurements are lost and re-acquired on the antennas within the system. This results in the measurement vector being dynamically modified from epoch to epoch, as the baselines being used in the system change.

Figure 6.4 shows the number of valid measurements in the system for a single blimp performing maneuvers within the highbay. There is a maximum of 23 measurements possible, which correspond to a maximum of 16 intra-vehicle single differences and 7 double differences. Whenever signals are lost on individual antennas within the

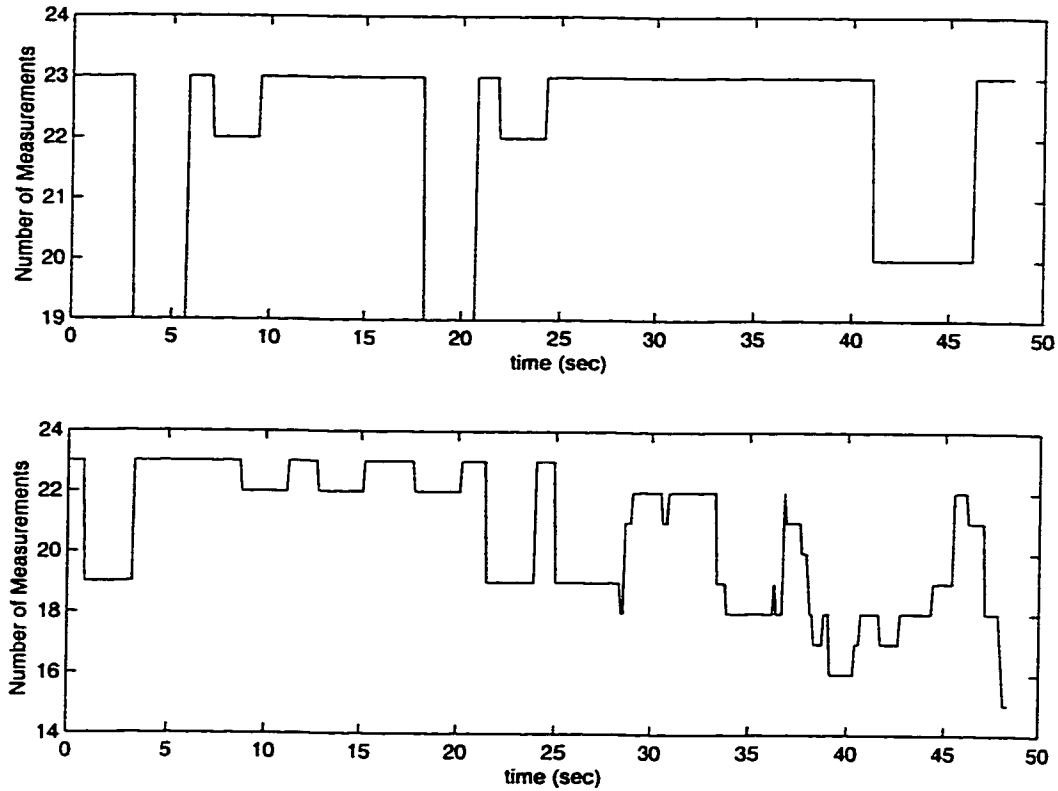


Fig. 6.4: Number of Valid Measurements During a Blimp Flight.

system, the total number of valid will measurements drop, and the measurement vector is reformulated to use the other baselines in the system in order to increase the number of independent measurements to the maximum possible (*i.e.* “all-baseline in view” formulation). The top plot in the figure is for a quasi-stationary maneuver (small motions), and the bottom plot is for a large scale maneuver within the highbay workspace. Note that the large scale maneuver results in significantly more variation in the number of available measurements because of the high multipath environment (see Chapter 2).

For the two vehicle configuration shown in Figure 6.3 there are a total of $9S$ possible inter-vehicle single differences that could be formed when there are S signals

commonly visible to all of the antennas. Of these measurements, only S are independent (assuming the intra-vehicle single differences are available as part of the attitude problem). The total number of possible signals for an N vehicle system, where each vehicle has M antennas is given by

$$S \binom{N}{2} M^2 \quad (6.29)$$

of these, the number of independent measurements (assuming common visibility) is $S(N - 1)M$. For example, for $N = 5$, $M = 4$, and $S = 8$, there are a total of 1280 possible inter-vehicle single differences, of which 128 are independent.

Depending on the problem size, it may not be prudent to maintain a running estimate of the biases associated with every possible measurement that could be formed. Instead, the estimator should only update the bias estimates corresponding to the current set of independent measurements that are being used. If a new measurement is brought on-line, the initial bias estimate for that measurement can be formed based on the formation state estimate using the other measurements that are already available. This approach was implemented in the blimp testbed as part of the general estimation problem.

6.4 Pseudolite Aided Attitude

“Pseudolite Aided Attitude” is a concept unique to the formation flying application. The basic idea is that a signal generated by an onboard pseudolite, and measured on *another* vehicle in the formation can be used to aid in the calculation of the relative attitude of the vehicles. This measurement can be used to improve the relative

attitude solution between vehicles within the formation in general, but may also be used to solve for the full, three-angle attitude for a vehicle with measurements only available across a single baseline. This situation could occur if there are only two antennas on a given vehicle, whether by design or malfunction, and also in the case of occlusion that could occur for some applications.

To analyze this approach, consider the system shown in Figure 6.5. In this case, there is a vehicle with two antennas (labeled 1, 2), and an onboard pseudolite. In addition there is another vehicle in the system with a single antenna shown (labeled m). A number of measurements can be formed using both the NAVSTAR satellites and the onboard pseudolite. These measurements are given by

$$\Delta\phi_{m1}^s = G \begin{bmatrix} \frac{X_A}{I} \\ \tau \end{bmatrix} + \beta_{m1}^s + \nu_{m1}^s \quad (6.30)$$

$$\Delta\phi_{12}^s = \tilde{G}T_{I/B}(\Psi, \Theta) \frac{X_B}{B} + \beta_{12}^s + \nu_{12}^s \quad (6.31)$$

$$\Delta\phi^p = \left| \frac{X_A}{I} + T_{I/B}(\Psi, \Theta, \Phi) \frac{X_{PB}}{B} \right| + \tau + \beta^p + \nu^p \quad (6.32)$$

where

$\Delta\phi_{m1}^s$ = single differences across antennas m , and 1 using the NAVSTAR satellites

$\Delta\phi_{12}^s$ = single differences across antennas 1, and 2 using the NAVSTAR satellites

$\Delta\phi^p$ = single differences across antennas 1, and m using the pseudolite

Ψ, Θ, Φ = Euler angles

τ = clock bias between the two vehicles

$\frac{X_A}{I}$ = position of antenna 1 relative to antenna m in inertial frame, I

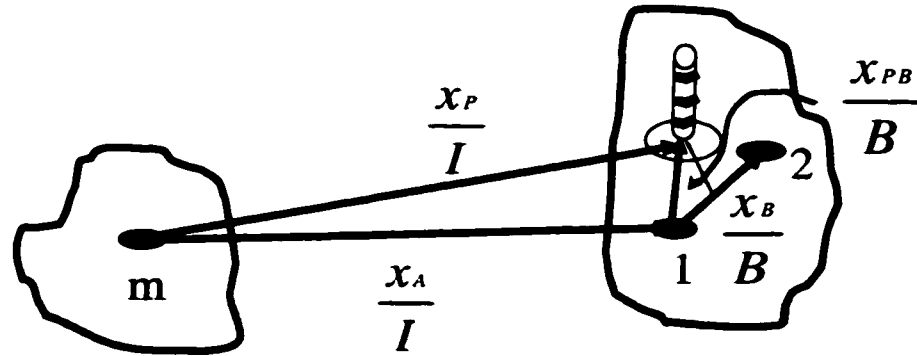


Fig. 6.5: Pseudolite Aided Attitude - Dual Antenna System

$\frac{x_B}{B}$ = position of antenna 2 relative to antenna 1 in Body frame, B

$\frac{x_{PB}}{B}$ = position of pseudolite relative to antenna 1 in Body frame, B

$T_{I/B}$ = transformation matrix from body coordinate system to inertial system

G = traditional GPS geometry matrix

\tilde{G} = traditional GPS geometry matrix with the last column deleted (there is no clock bias between measurements collected on the same receiver)

β = carrier-phase bias corresponding to each measurement

ν = carrier-phase noise corresponding to each measurement

The body coordinate system is connected to the vehicle. Note that, in this case, the measurements from the far constellation (Eqs. 6.30 and 6.31) can be used to solve for only two of the Euler angles, Ψ , and Θ . The rotation about the baseline between antennas 1 and 2 on the body is unobservable without the additional measurement provided by the pseudolite. The clock bias, τ , is present in Eq. 6.32, but will be solved for as part of the relative positioning problem between the two vehicles.

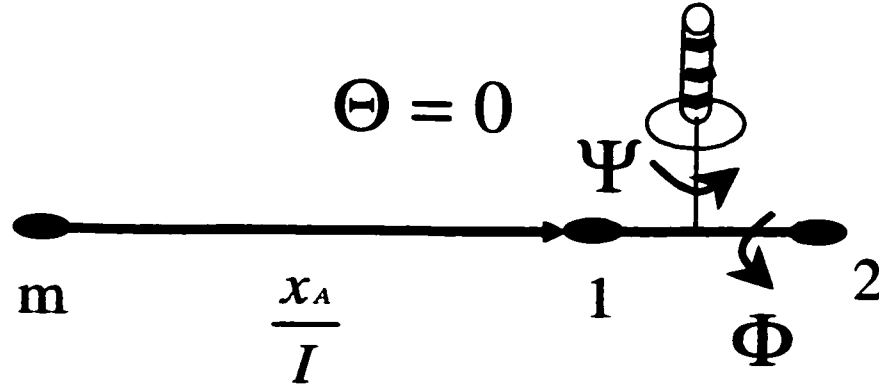


Fig. 6.6: Pseudolite Aided Attitude - Dual Antenna System. Φ is the rotation about the axis formed by the antenna baseline. Ψ is the rotation about an axis perpendicular to the antenna baseline axis, and passing through the pseudolite. Θ is the rotation about the axis perpendicular to the other two.

In general, Eqs. 6.30, 6.31, and 6.32 can be used to solve for all three Euler angles of the given vehicle. However, for the orientation given in Figure 6.6, a singularity exists wherein the sensitivity of the measured differential-carrier phase from the pseudolite to roll angle motions is 0. In particular, for the orientation shown, Φ is unobservable because motions about the roll axis do not result in any change to the measured carrier-phase from the pseudolite. This singularity will be eliminated if more than two vehicles are in the system as long as all the vehicles, including the one with the pseudolite, are not positioned along a single line in space.

Figure 6.7 gives a plot of the sensitivity of the measured carrier-phase signal from the pseudolite to roll angle motions for the system shown in Figure 6.6. This quantity is computed as

$$\text{sensitivity} = \frac{\partial \Delta \phi^p}{\partial \Phi} \quad (6.33)$$

The sensitivity plotted in Figure 6.7 has been normalized by the distance of the pseudolite perpendicular to the baseline (denoted by l) between antennas 1 and 2. A measured differential carrier-phase noise of 0.5 cm was assumed. For a roll accuracy

of better than 1° , the sensitivity constraint must satisfy

$$\text{sensitivity} > 1/l \quad (6.34)$$

If the condition given by Eq. 6.34 is met, then an attitude change of 1° will result in the measured carrier-phase from the pseudolite exceeding the receiver phase noise (*i.e.* the motion will be observable in the measurement). For the singular case of $\Psi = 0$, the distance from the pseudolite to antenna m will not change at all (see Figure 6.6), and hence the sensitivity is 0. For the degenerate case of $l = 0$, the pseudolite phase center is located directly on the axis connecting antenna 1 and 2. Intuitively, any rotation about the baseline results in no motion of the pseudolite in space, and the measured carrier-phase will not vary with the roll angle. If $l = 1$ m, for example, then any configuration with a sensitivity > 1 will result in the attitude being observable to better than 1° . Note that the singular configuration will vary with Θ .

In summary, the "pseudolite aided attitude" concept is a technique wherein the measurements from an onboard pseudolite are used not only for relative positioning, but also as an aid in attitude determination. For the general case, the measurements from the onboard pseudolites couple the attitude between the vehicles in the formation, and improve the relative attitude dilution of precision (ADOP). Additionally, the concept can be used to provide a measure of system robustness in the event of antenna failure, or occlusion, since only a single baseline is required to determine the full three angle attitude estimate of a vehicle.

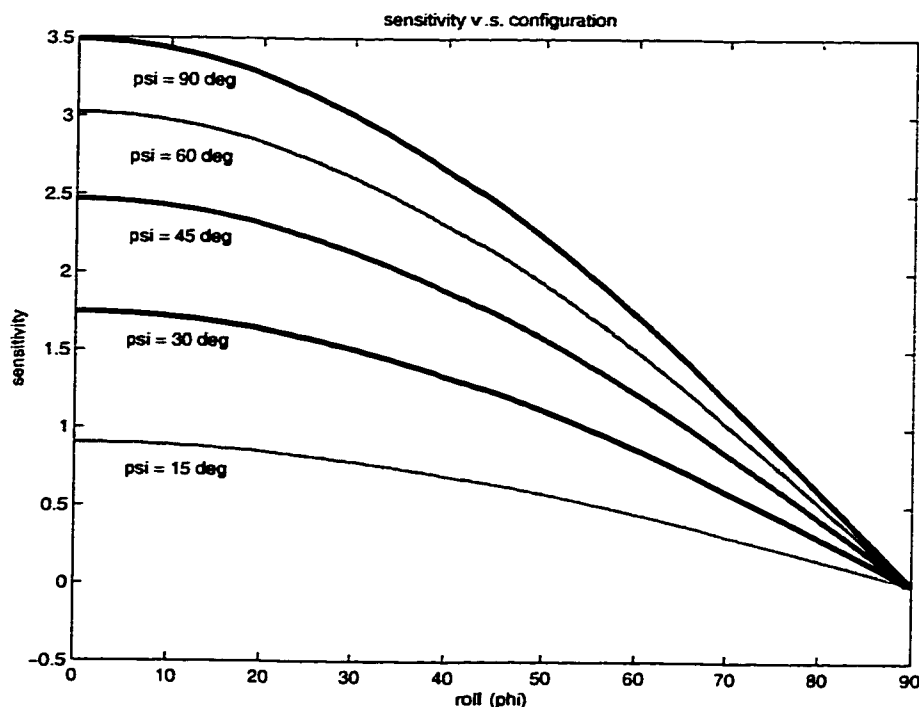


Fig. 6.7: Sensitivity of Pseudolite Aided Attitude - Dual Antenna System. The sensitivity is normalized to the baseline length, l (in meters).

6.5 Summary

This chapter presented a number of algorithms for the general formation flying application. These algorithms are used to increase the robustness of the state estimation, as well as handle the effects of the polarization of the GPS signal. The “all-baseline-in-view” algorithm was implemented experimentally in order to allow the system to operate for extended periods of time. In fact, the duration of the blimp flights was driven by the life of the batteries on each vehicle.

~

Chapter 7

Experimental Results

Several flight tests were conducted to demonstrate the performance of the integrated GPS system. These experiments were designed to exhibit key features of the GPS sensors and the algorithms required for formation flying vehicles. This chapter presents results for a number of test flights. The experiments included:

1. Demonstration of an autonomous take off and landing of a single vehicle (inside).
2. Demonstration of two vehicles performing autonomous maneuvers while maintaining formation (both inside and outside).
3. Demonstration of a single vehicle performing a large scale, circular maneuver (inside).
4. Demonstration of a single vehicle station keeping (outside).

7.1 Single Blimp Maneuvers

7.1.1 Indoor Auto Landing Test

The automatic landing tests were developed as a comprehensive demonstration of the entire system, including the GPS sensors, and the estimation and control algorithms (the LQR controllers on the blimps were implemented by Park [DP98]). These experimental results demonstrate the robust performance of the state estimation and control of a single vehicle, which is a key step towards formation flight. Note that the relative position sensing accuracies that are obtained for the two blimps in formation are the same as those demonstrated in the auto landing tests, since the auto landing tests measure the position sensing error relative to another GPS antenna (the reference station) in the system. The measurements between the GPS antennas in the system determine the relative positioning accuracy, as described in Chapter 4.

At the start of the auto landing sequence, a blimp was placed on a randomly located platform. A command to land on another platform was then sent to the vehicle. The platform (dimensions 1.17 m \times 0.64 m) was placed at a known point, 1.22 m (4 ft) from the ground level. The location of the landing site was provided to the blimp prior to take-off. The blimp took-off vertically from the first platform, and then set a heading towards the landing point. The blimp maintained a constant altitude and heading during most of the transit, except during the take-off and landing. A typical 3-D autonomous flight trajectory is shown in Figure 7.1. The flight path is shown in more detail in Figure 7.2, and is discussed below.

Figure 7.2 shows the time history plot of the horizontal and vertical position estimates from the GPS sensor while performing an autonomous take-off and landing sequence. The altitude was set at 0.68 m above the landing platform. Note that after

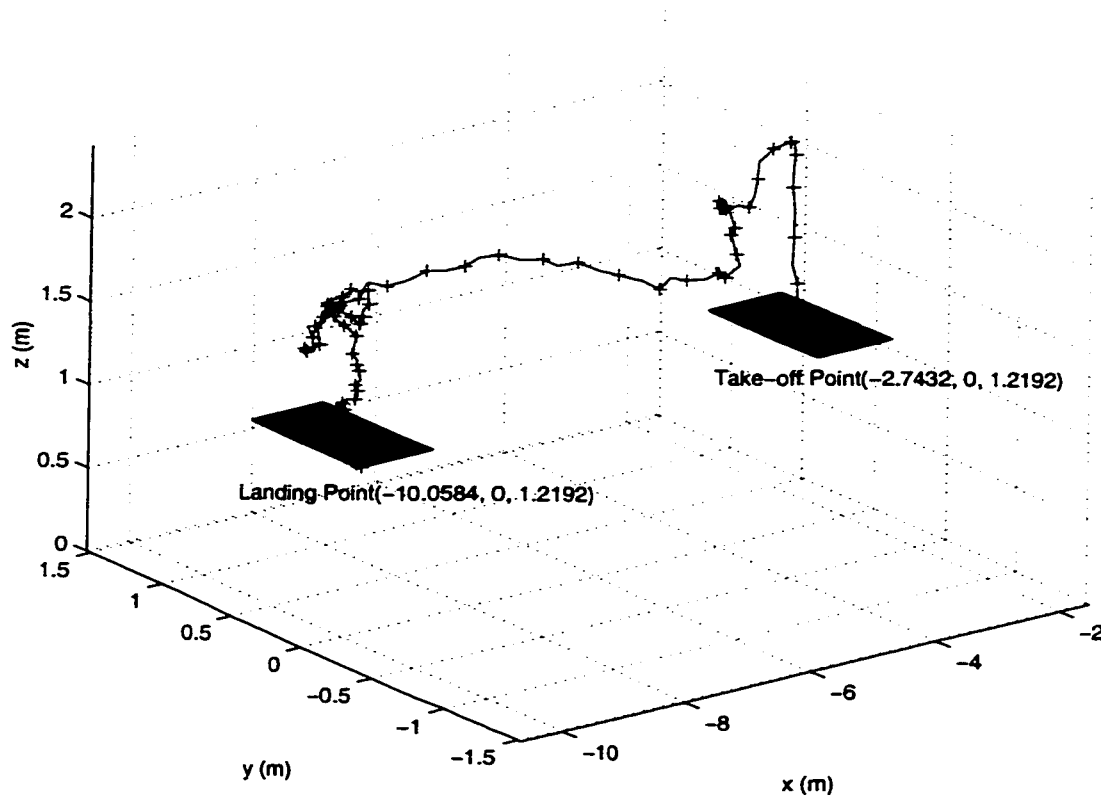


Fig. 7.1: 3-D Plot of Auto Landing Flight Path

approximately 50 seconds, when the vehicle had settled over the landing platform, the blimp started the landing sequence by initiating a descent of 5 cm/sec while holding the horizontal position. The decent sequence is easily visible in the plot of the altitude. There is a slight variation in the blimp altitude while it was moving between the platforms (from $t = 10$ sec to $t = 50$ sec). This variation was on the order of a few centimeters, and was a result of the disturbances that the vehicle is subjected to. Additionally, there is a transient in the Y direction, beginning at take-off, which settles as the vehicle maneuvers to the landing platform. This was a result of the vehicle controller [DP98]. The experiments indicate that the GPS sensing was working quite well, as the blimp vehicle was able to traverse across a large part of the highbay floor successfully.

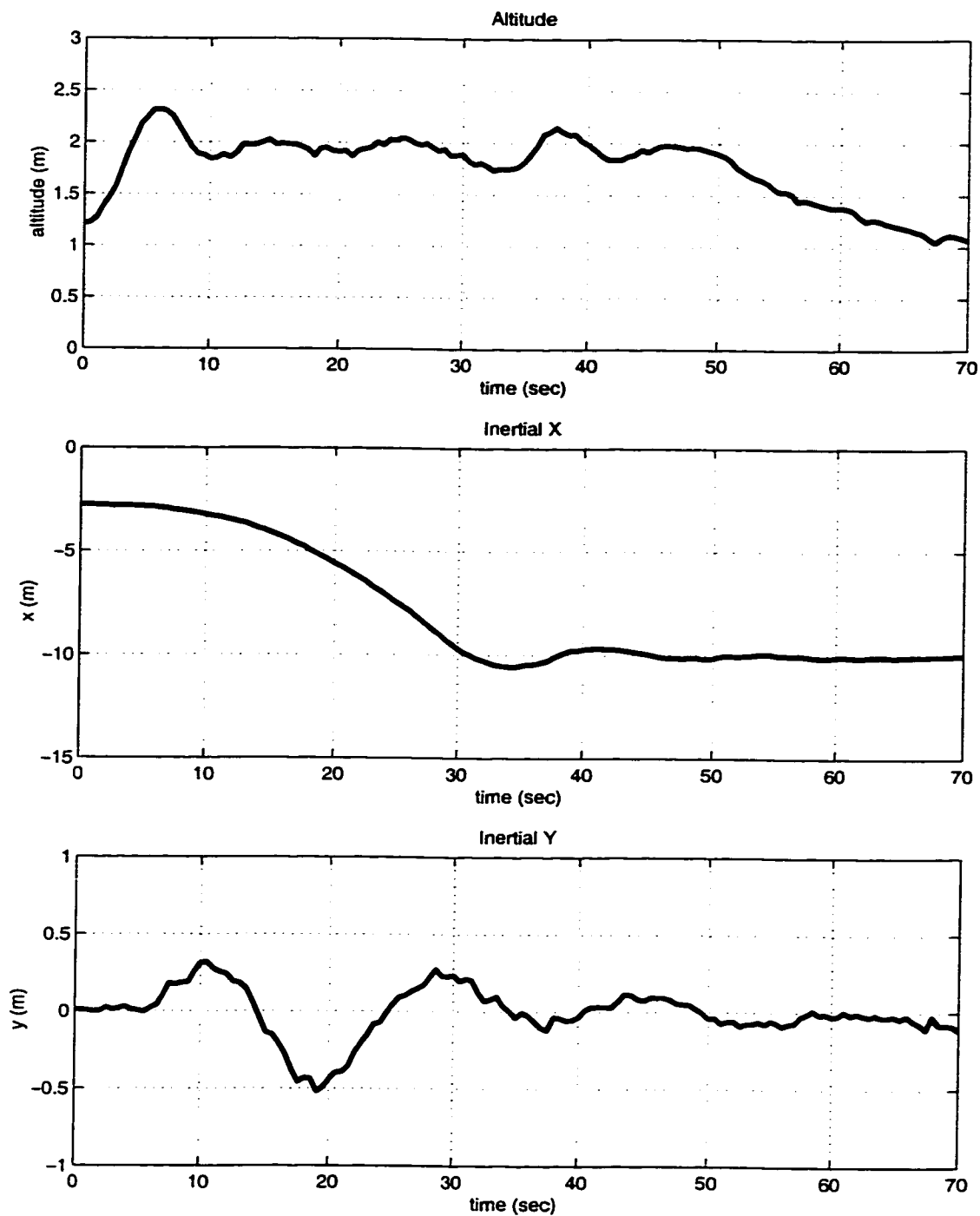


Fig. 7.2: Vertical and Horizontal Flight Paths for an Auto Landing Sequence of a Single Blimp Traversing Across the Indoor Laboratory.

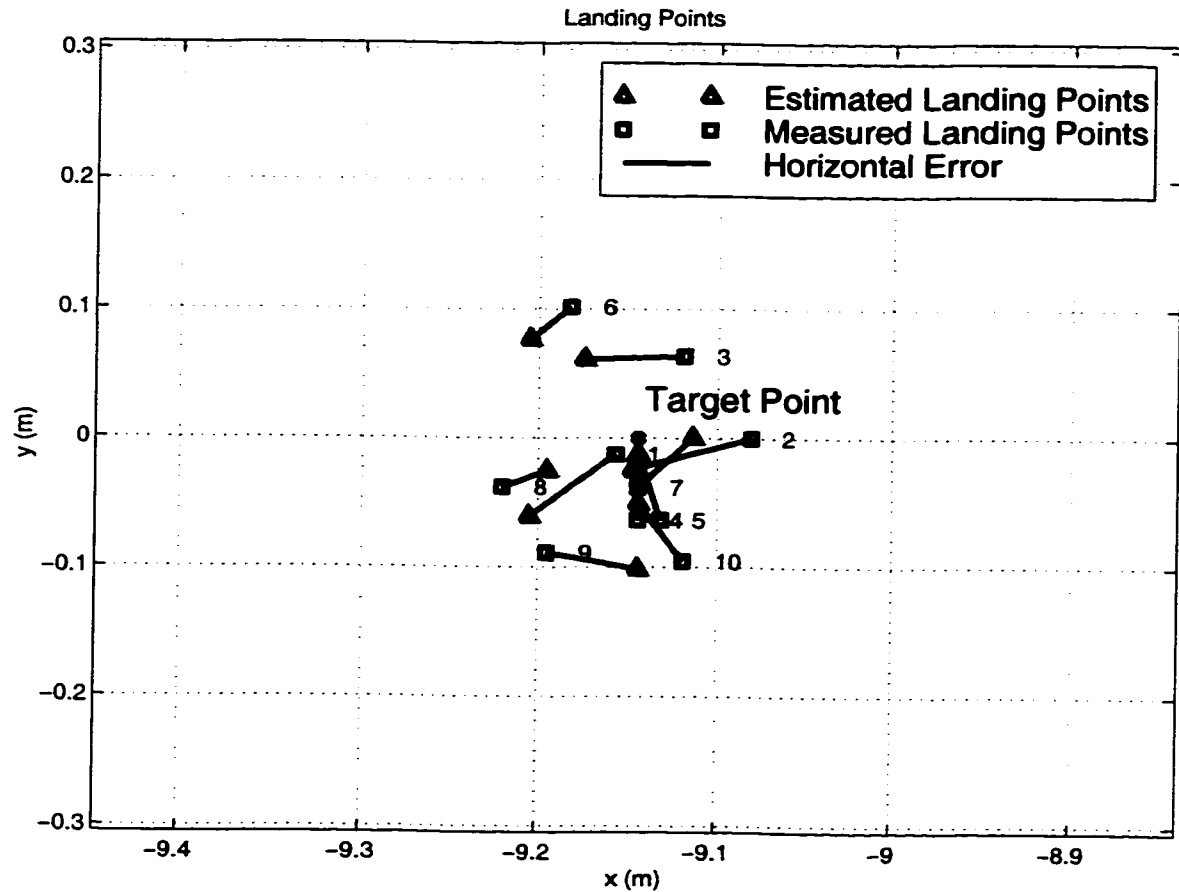


Fig. 7.3: Measured and Estimated Landing Points

No truth sensor is available to validate the state estimation during flight, so the accuracy of the GPS estimator may only be verified at the landing point. The landing points were measured by a ruler once the blimp finished the descent sequence, and the accuracy of this manual measurement is on the order of 2 mm. Figure 7.3 shows the 10 horizontal landing points as measured on the landing platform and estimated by GPS sensor, respectively. Tables 7.1, and 7.2 summarize the errors for 10 autonomous landings.

The measured and estimated landing points are summarized in Table 7.1. Note that the target landing point was $X = -9.14$ m (-30.0 ft) and $Y = 0.0$ m in these

Table 7.1: Results of 10 Auto Landings.

Horizontal Landing Point	X		Y		Distance from Target	
	Mean	STD	Mean	STD	Mean	STD
Measured (m)	-9.152	0.040	-0.024	0.064	0.070	0.028
Estimated (m)	-9.164	0.031	-0.015	0.052	0.055	0.034

Table 7.2: Estimation Error in Landing Points.

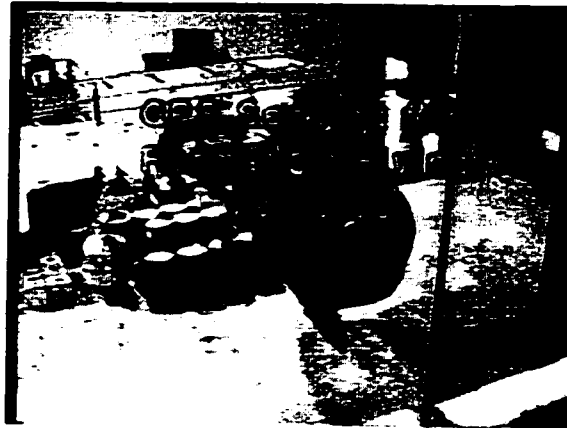
Horizontal Estimation Error (m)	X error		Y error		Distance error	
	Mean	STD	Mean	STD	Mean	STD
Estimate - Measurement	-0.012	0.040	0.006	0.034	0.049	0.015

experiments. Table 7.1 shows that the estimated and measured landing points are tightly clustered (standard deviation less than 7 cm for both).

Table 7.2 gives the landing errors in terms of the inertial X and Y coordinates. The horizontal distance between the estimated and measured landing points is also shown. The average value of the horizontal estimation error (distance error) was only 0.049 m. Considering the HDOP value of 1.25 and multipath effects in the testbed, horizontal errors of 5 cm can be expected based on carrier phase measurement noise levels. The VDOP in the testbed (5.03) is four times larger than the HDOP. This, combined with large multipath error, can cause relatively large errors in the vertical position estimate. This error can be seen in Figure 7.1 and Figure 7.2, as demonstrated by the fact that the vertical position estimate was approximately 12 cm below the height of the actual landing platform (1.22 m high) at the conclusion of the flight.

The auto landing tests capture an extremely successful demonstration of precise vehicle estimation and control, and show the cm-level positioning accuracies that are being obtained.

Figure. 7.4, and 7.5 show a video sequence for another autonomous take-off and landing of a single blimp. The entire duration of the maneuver was approximately 100 seconds. Clearly visible is the initial take-off sequence ($t=0, 8, 17$ sec). In this case, the vehicle took off from the floor, and was initially oriented perpendicular to the desired flight path to the landing platform. The blimp traversed across the highbay floor ($t=25, 33, 42, 50, 58, 66$ sec) until it reached the landing area. From $t=66$ seconds to $t=99$ seconds, the blimp was in a decent mode onto the top of the landing platform.



AutoLanding, $t=0$ sec



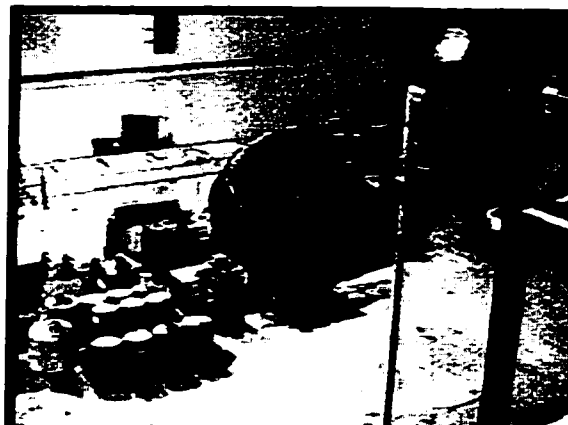
AutoLanding, $t=8$ sec



AutoLanding, $t=17$ sec



AutoLanding, $t=25$ sec



AutoLanding, $t=33$ sec



AutoLanding, $t=42$ sec

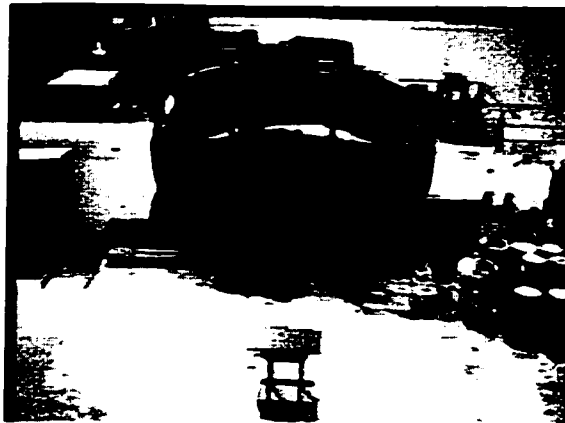
Fig. 7.4: Autonomous Auto Landing - Part I



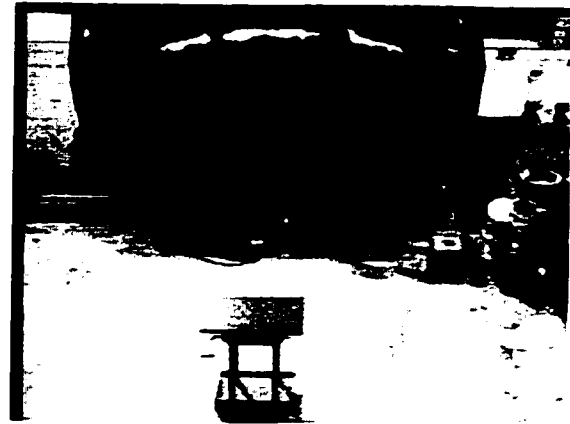
AutoLanding, $t=50$ sec



AutoLanding, $t=58$ sec



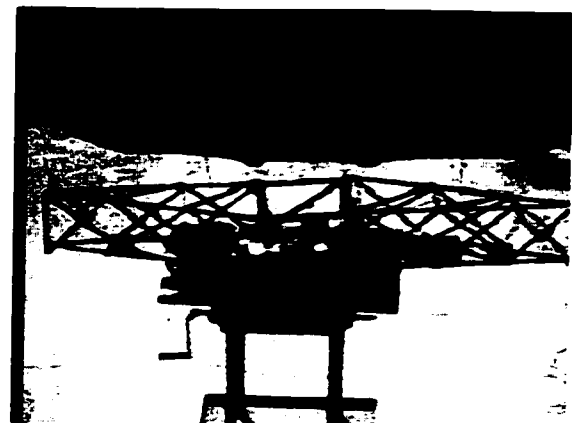
AutoLanding, $t=66$ sec



AutoLanding, $t=75$ sec



AutoLanding, $t=83$ sec



AutoLanding, $t=99$ sec

Fig. 7.5: Autonomous Auto Landing - Part II

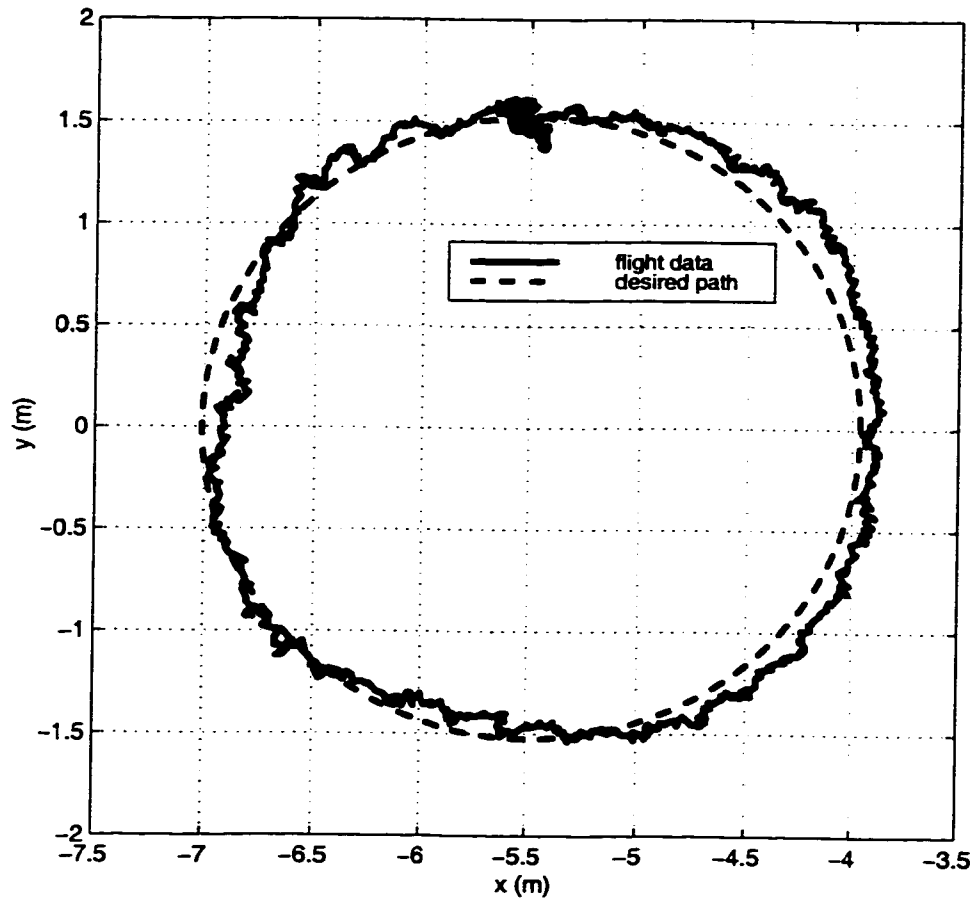


Fig. 7.6: X-Y Plot of a Circular Blimp Flight Inside the Highbay

7.1.2 Indoor Circular Flight

Another large-scale maneuver of a single blimp was performed inside the highbay to further demonstrate the robustness of the GPS sensing and estimation. These maneuvers result in GPS signals being constantly lost and re-acquired on the antennas on the vehicle. In order to perform the state estimation reliably, the frequent signal loss must be handled as described in Chapter 6.

Figure 7.6 shows a top down view of a large circular blimp flight path inside the highbay. Shown in the figure are the actual flight path (from the GPS sensor), as well as the desired flight path. The plot indicates that the horizontal error was quite

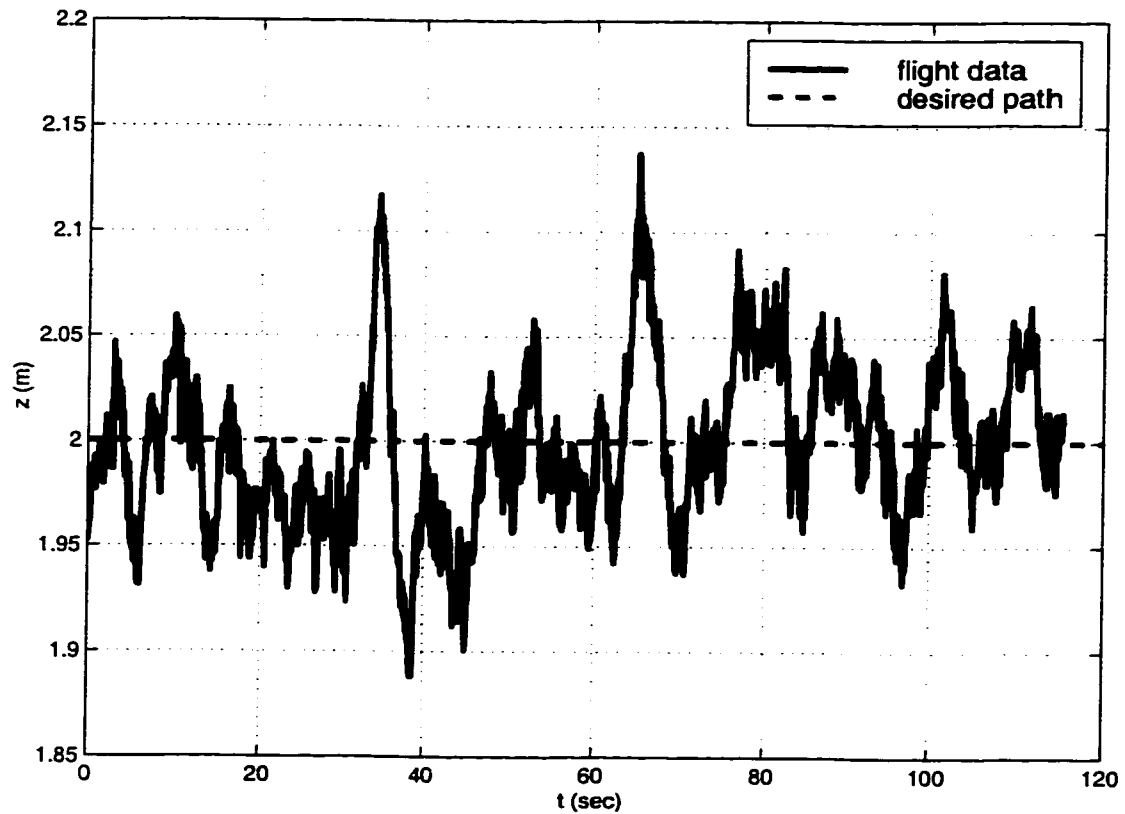


Fig. 7.7: Altitude Plot of a Circular Blimp Flight Inside the Highbay

small (see Table 7.3) over the entire maneuver. The blimp returned to the same starting location ($X = -5.5$ m, $Y = 1.5$ m), after approximately 120 seconds. The start location is visible in the plot as a large clump of data, as the vehicle station kept at that point once the maneuver was complete.

Figure 7.7 shows the altitude of the blimp during the entire maneuver. The desired altitude was 2 m. There is a low frequency oscillation visible, which is most likely due to the response of the RC motors used on the blimp. The two spikes in the altitude (≈ 10 cm errors) were the result of a disturbance, and may have had to do with the fact that the blimp flew over a one meter high granite table at that point in the

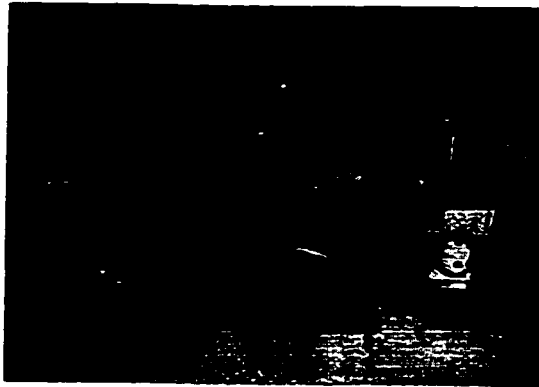
Table 7.3: Flight Error for Circular Maneuver

Horizontal Error (m)		Altitude Error (m)	
Mean	STD	Mean	STD
0.021	0.075	0.002	0.039

maneuver. However, small errors are to be expected as the blimps are difficult to model and control exactly.

Table 7.3 summarizes the results of the maneuver. The horizontal error is the horizontal distance from the vehicle location (as determined by GPS) to the nominal (commanded) flight path. The mean value of the horizontal error (0.021 m) was positive, and indicates that the average blimp position was slightly outside the circle. The blimp had to accelerate during the entire maneuver (as it was in a circle), and this contributed to the horizontal error.

Figures 7.8 and 7.9 show a video sequence of a typical circular flight. The radius of the circular path was approximately 8.5 ft, and the duration of this particular maneuver was 90 seconds. The blimp started and ended at the same location ($t=0$, 90 sec) in space after traversing the path. Note that this maneuver required a complex coordination of the various actuators that would likely be impossible for a human pilot to do by hand.



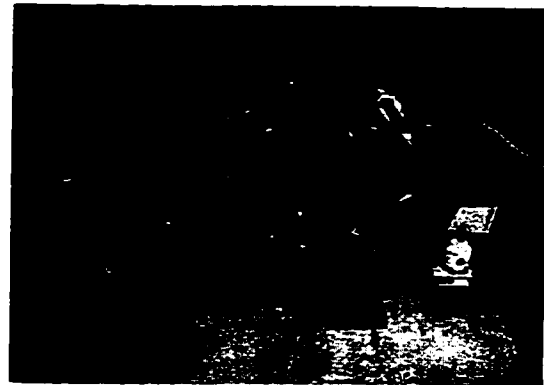
Circular Motion, $t=0$ sec



Circular Motion, $t=8$ sec



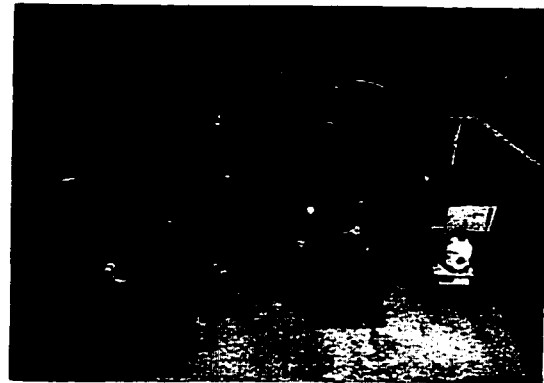
Circular Motion, $t=20$ sec



Circular Motion, $t=30$ sec



Circular Motion, $t=35$ sec

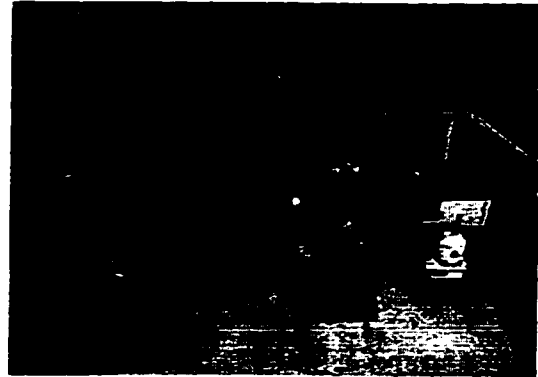


Circular Motion, $t=44$ sec

Fig. 7.8: Circular Motion of a Single Blimp - Part I



Circular Motion, $t = 50$ sec



Circular Motion, $t = 58$ sec



Circular Motion, $t = 66$ sec



Circular Motion, $t = 75$ sec



Circular Motion, $t = 83$ sec



Circular Motion, $t = 90$ sec

Fig. 7.9: Circular Motion of a Single Blimp - Part II

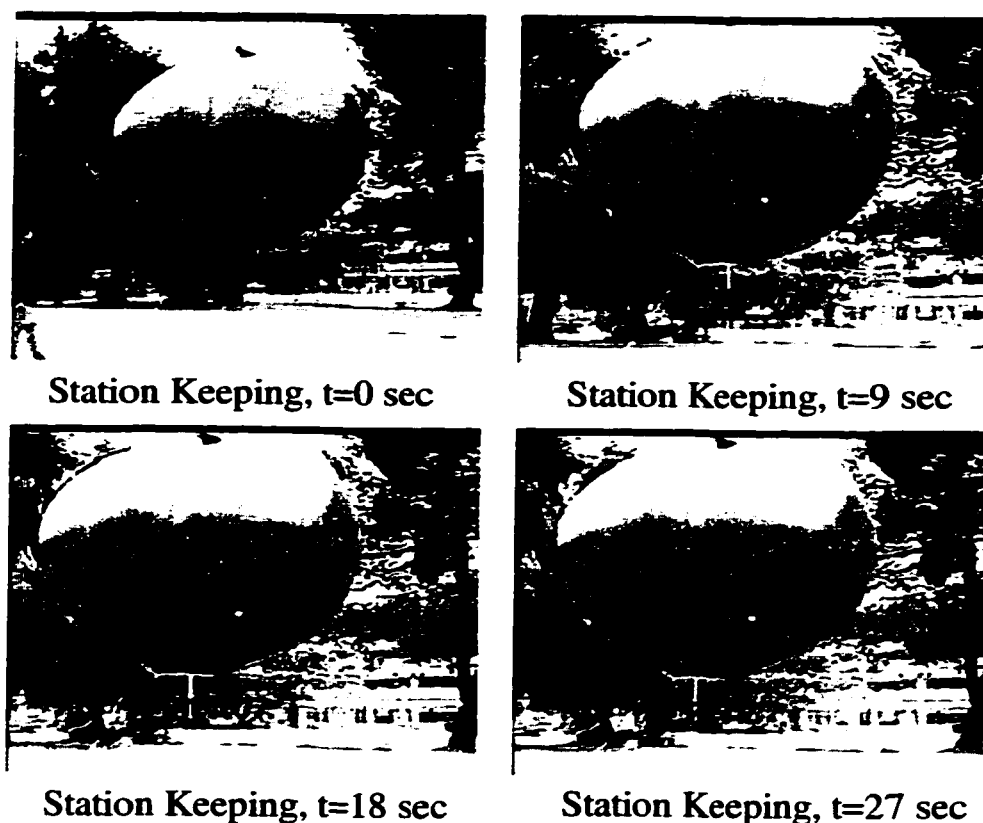


Fig. 7.10: A Single Blimp Station-Keeping Outside

7.1.3 Outdoor Station-Keeping

The blimps made several flights outside using the NAVSTAR constellation. The sensing is actually easier outside due to the fact that the transmitters are in the far field (see Chapter 4), and the multipath is less severe. The most significant challenge is the impact of the environment on the blimp, as even slight breezes can saturate the RC motors, causing the blimp to be blown along with the wind in a uncontrollable manner. The purpose of the outside tests were to show that the sensing algorithms can be transitioned from indoors to outside with minimal effort.

Figure 7.10 shows a video sequence of a single blimp station-keeping outside on a grass field located on Stanford campus. The blimp was commanded to maintain the

same relative position (to a fixed reference station) for the duration of the maneuver. Despite the impact of the environment, the blimp was able to station keep successfully. Thereby confirming that we can formation fly outside with the NAVSTAR satellites.

7.2 Formation Flight Test

7.2.1 Formation Flight Indoors

An experiment was performed with the two vehicles to demonstrate the complete 3D formation flying capability. The vehicles were arranged to fly in a line formation, and were initialized at random orientations and distances apart. The maneuvers for the formation were a complicated combination of changes in the horizontal position, altitude, and yaw angle. During these maneuvers, the controller attempted to maintain the initial relative X and Y distances between the two blimps while also maintaining an identical altitude and yaw angle. The follower vehicle (Blimp-1) autonomously reacted to changes in the lead vehicle's (Blimp-2) position and attitude.

In the results shown here, the blimps started 7.3 m apart in X and 0 ft apart in Y . The altitudes were approximately 0.3 m apart. The heading angles were both 0° . The 3D position and orientation data was taken from the GPS sensors for 100 seconds. The leader vehicle was manually moved approximately 0.91 m (3 ft) forward and then 0.91 m (3 ft) backward. Additionally, it was moved in a full 180° yaw motion (two 90° steps) and underwent a change in vertical height.

Figures 7.11, 7.12 and 7.13 show the time histories for the X , Z , and Ψ (yaw angle) states for the two vehicles. A time lag in the response of the follower vehicle (Blimp-1) is evident in the data, due to its dynamics when it reacted to the state errors. This lag may be reduced by implementing a feedforward control architecture.

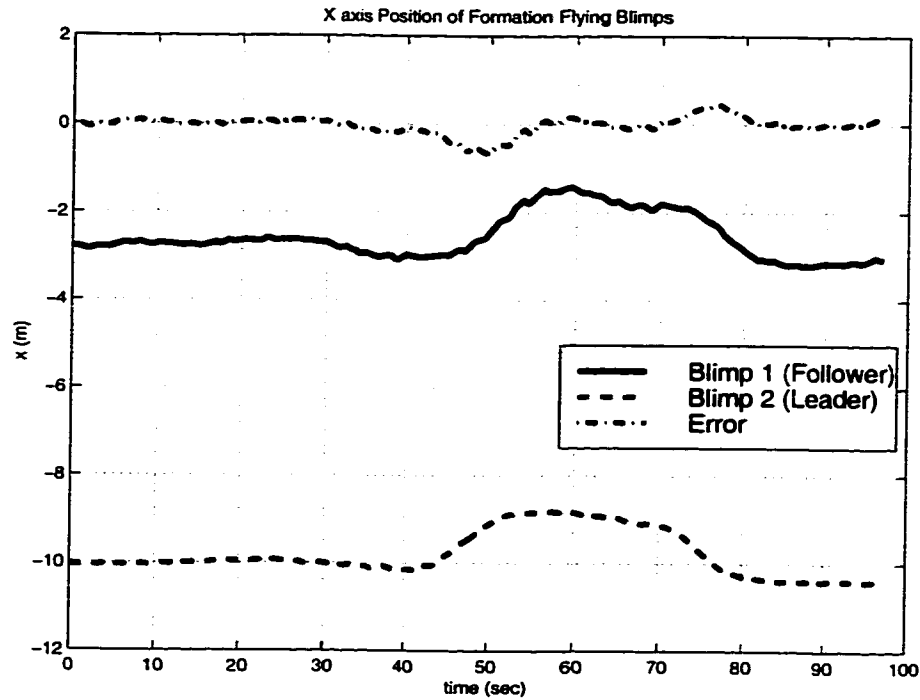


Fig. 7.11: X Axis Position of Formation Flying Blimps

The system errors are represented by the differences in the altitude, yaw angle, and the horizontal displacement (current blimp X and Y position minus the initial X and Y position) of the two vehicles. These errors are shown in Figures 7.11, 7.12 and 7.13.

Note that the follower blimp successfully stayed in formation with the leader blimp during the entire maneuver. The blimp vehicles have the most control authority in the yaw state, and this is evident in the yaw error as it stayed quite small during the whole flight. The transients in the errors (a result of the vehicle motion) returned to a steady state value of 0 when the leader blimp stopped its motion. The position error between the vehicles within a formation will be a function of the dynamics of all the vehicles. These tests demonstrated that precise, 3D formation flying is possible with GPS sensing.

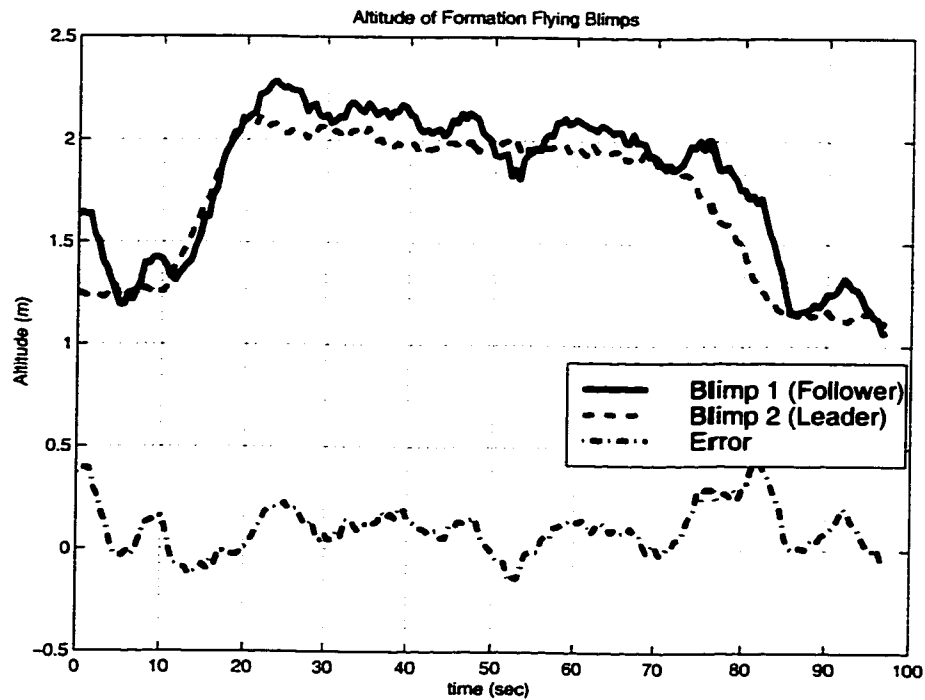


Fig. 7.12: Altitude of Formation Flying Blimps.

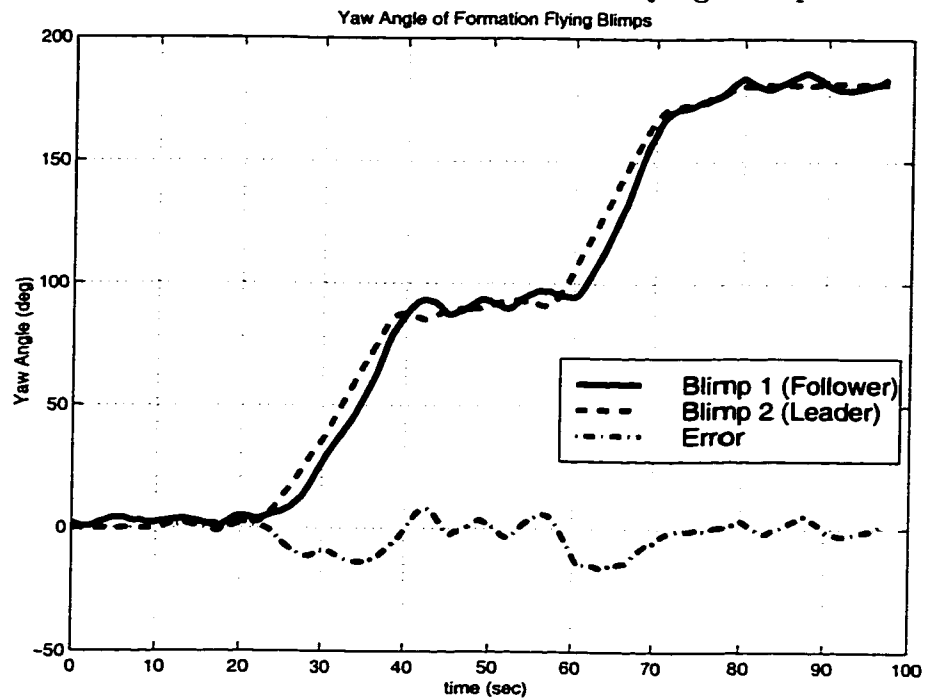
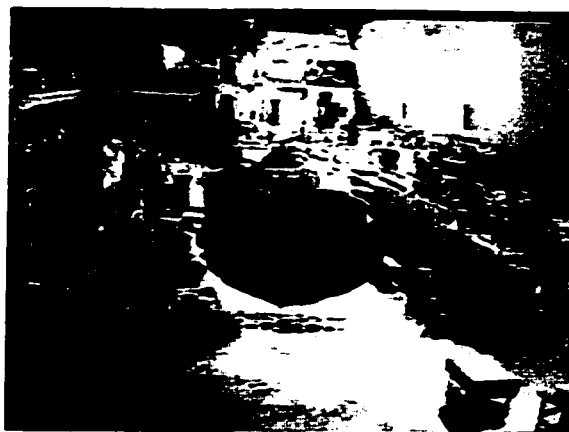
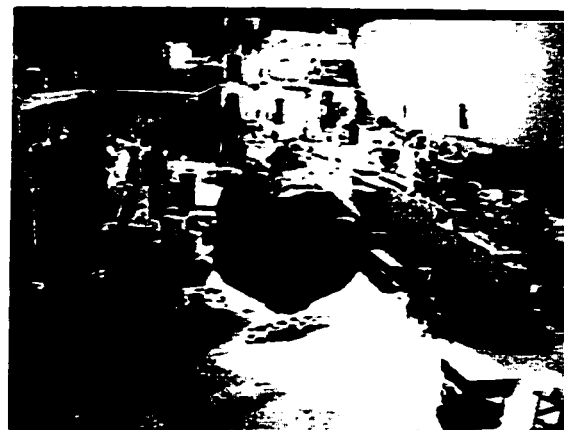


Fig. 7.13: Yaw Angle of Formation Flying Blimps.

Figures 7.14, 7.15 and 7.16 show another formation flight inside the highbay where both vehicles were autonomously controlled. The vehicles were commanded to maintain the same relative positions and attitude during the entire sequence of maneuvers. The blimps started out facing the east wall of the highbay ($t = 0$ sec), and were commanded to make a series of slew maneuvers in order to face the north wall ($t = 12, 24, 36$ sec). At this point ($t = 48$ sec), the blimps were given commands to translate upwards by 2 meters ($t = 60, 72, 84$ sec). Once they reached their new altitude, a series of heading commands were sent in order to bring the vehicles back to an eastward facing ($t = 96, 108, 120$ sec). The blimps then translated east by 1 meter ($t = 132$ sec), and then translated westward by 2 meters ($t = 144, 160$ sec). The entire duration of this formation flight was 167 seconds.



Formation Flight, $t=0$ sec



Formation Flight, $t=12$ sec



Formation Flight, $t=24$ sec



Formation Flight, $t=36$ sec



Formation Flight, $t=48$ sec



Formation Flight, $t=60$ sec

Fig. 7.14: Indoor Formation Flight - Part I



Formation Flight, $t=72$ sec



Formation Flight, $t=84$ sec



Formation Flight, $t=96$ sec



Formation Flight, $t=108$ sec



Formation Flight, $t=120$ sec



Formation Flight, $t=132$ sec

Fig. 7.15: Indoor Formation Flight - Part II

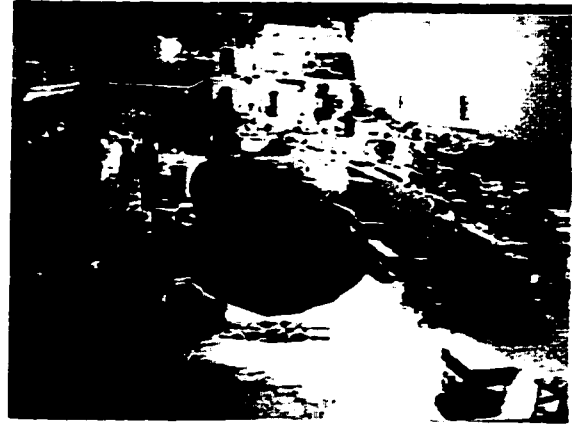
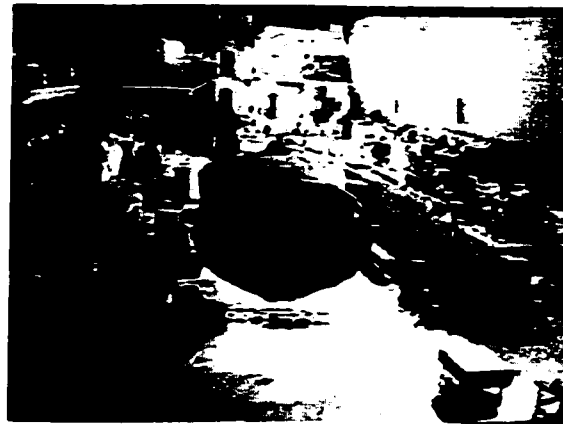
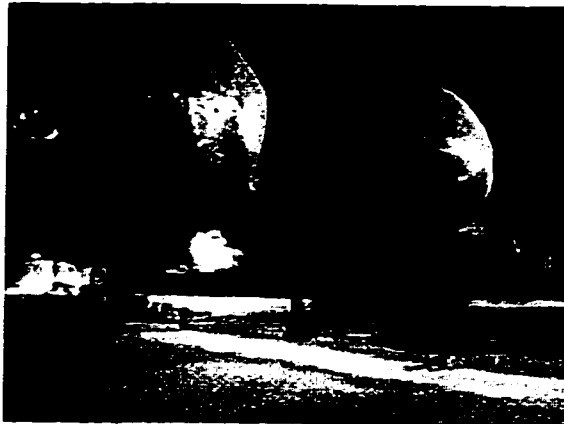
Formation Flight, $t=144$ secFormation Flight, $t=160$ secFormation Flight, $t=167$ sec

Fig. 7.16: Indoor Formation Flight - Part III

7.2.2 Outdoor Formation Flight

Figures 7.17 and 7.18 show an outdoor formation flight that took place at the Engineering Quad on Stanford campus. The blimps were commanded to maintain the same relative position and heading during the entire maneuver. They started at the same heading ($t=0$ sec), and were commanded to perform a slew to a new heading ($t=14$ sec). At this point, they were commanded to return to their original heading angle ($t=21$ sec). The vehicles were then commanded to maintain their positions

and hold station. Due to the slight wind that was present, the entire formation was subjected to rather large disturbances (for small, lighter-than-air vehicles) and the entire formation translated away from the camera ($t=28$ sec). However, clearly visible in the photos ($t=28, 35, 42, 47$ sec) is that the blimps maintained their *relative* positions and headings nicely.



Formation Flight, $t=0$ sec



Formation Flight, $t=7$ sec



Formation Flight, $t=14$ sec



Formation Flight, $t=21$ sec

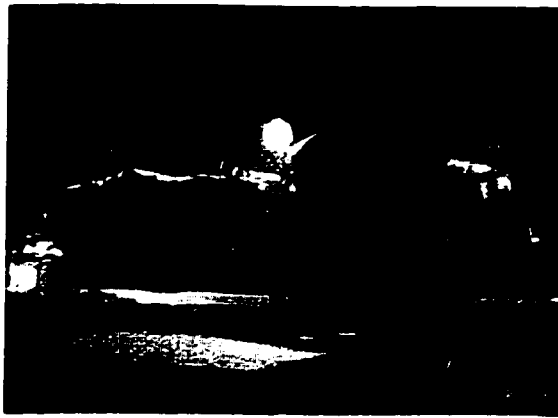


Formation Flight, $t=28$ sec



Formation Flight, $t=35$ sec

Fig. 7.17: Outdoor Formation Flight - Part I



Formation Flight, $t=42$ sec



Formation Flight, $t=47$ sec

Fig. 7.18: Outdoor Formation Flight - Part II

~

Chapter 8

Conclusions

This chapter provides a summary of the theoretical and experimental contributions developed during the course of this research. Additionally, issues related to transitioning a formation from the indoor testbed to operations in-orbit about the Earth are addressed. Finally, future areas of formation flying research are explored.

8.1 Summary of Contributions

The objective of this thesis was to demonstrate that carrier-phase GPS provides a robust relative navigation sensor for 3-D, formation flying vehicles. The following contributions were made as part of this research:

8.1.1 Demonstrated Robust, 3-D Formation Flight

Precise, 3-D formation flight using only GPS sensing was demonstrated in an experimental laboratory. To this end, a unique testbed consisting of two lighter-than-air

vehicles (blimps) was constructed. An estimator was implemented on a real-time operating system, and centimeter-level relative positioning, as well as precise, relative attitude was obtained. The results were validated both inside the laboratory, and outside using the NAVSTAR constellation.

8.1.2 GPS Receiver Development

A key limitation in GPS related research is access to appropriate receiver hardware. This is especially true for the formation flying application, where multiple (low power, low cost, with code access) devices will be required. Extensive hardware and software modifications were made to an available single antenna board, and an **expandable, cheap, open architecture, attitude capable** receiver was developed. This receiver has since formed the basis for several other projects, to include the SSDL Orion Missions, the Mars Exploration Project, the Non-Aligned Antenna Experiment, and the next generation formation flying experiment (multi-truck testbed).

8.1.3 Carrier-phase Bias Initialization

One of the main challenges in CDGPS estimation is the solution of the carrier-phase biases, which are required in order to navigate to centimeter-level accuracy. In order to rapidly solve for these biases, onboard pseudolite augmentation was proposed, which allows the relative vehicle motion to be used as an initialization technique. A measure of the bias observability for a formation of vehicles was defined, and several path-planning algorithms for initialization were developed. This includes the exact optimal control solution, as well as several quasi-optimal algorithms.

8.1.4 Estimation Robustness

Robustness is an important issue for any system. This is especially true for space-borne formations, since onboard sensing problems will need to be fixed either remotely, or would require a manned-space launch. The measured carrier-phase can suffer from cycle-slips (extra or missing carrier cycles), especially at low SNRs. Additionally, the signals being tracked on the antennas on each vehicle can vary over short time scales due to general vehicle motion. Two algorithms were developed which address the robustness issue. The first is the “all baseline in view” measurement formulation, which accounts for the rapid loss and acquisition of signals on individual antennas on a vehicle. The second is a method to detect measurement errors caused by cycle slips. These algorithms can be used to increase the robustness of the state estimation.

8.1.5 General Formation Flying Issues

The circular polarization of the GPS signal introduces another component to the measurement vector which must be accounted for in the general formation flying application. This was analyzed for the blimp testbed, and a simple method to account for this effect was introduced. A convergence proof for the algorithm was also developed.

In addition to being used as an initialization tool, onboard pseudolites may be used as an additional ranging signal as part of the general state estimation problem. To this end, a concept called “Pseudolite Aided Attitude” was proposed. The basic idea of which is that a vehicle’s attitude may be computed by using the measurements available on another vehicle from its own onboard pseudolite. The concept can be used to increase the system robustness, since the vehicle attitude estimate can be determined even in the event of an antenna failure.

8.2 Transitioning from an Indoor Testbed to LEO

The blimp testbed operated inside a large building using a pseudo-constellation, and outside using the NAVSTAR satellites. However, it is important to note how this work relates to operations in a Low Earth Orbit. The following discusses some of the key differences between the indoor/outdoor and LEO environments and the impact of these differences on the Orion mission - a planned space-based formation flying experiment being developed at Stanford.

Motion: Spacecraft in a low Earth orbit environment will generally experience very different motion than most terrestrial vehicles. The significant relative motion between the NAVSTAR satellites and LEO spacecraft will result in a large Doppler shift of the received RF signals. As discussed in Lightsey [GL97], these large Doppler shifts significantly increase the frequency range that must be searched to acquire and lock onto the GPS signals. These changes impact the selection of the integer initialization approach.

The LEO spacecraft may also rotate at rates and in directions that are not common to terrestrial vehicles, resulting in an issue of how to keep the NAVSTAR satellites in view of the vehicle antennas. This can be resolved using many (non-aligned) antennas to increase the sky coverage [JCA99].

Environment: The differences in operating environments will have several important impacts. For example, we would expect much less multipath in LEO. Multipath is reflected GPS signal interference which degrades the performance of the sensor. Additionally, the large temperature fluctuations characteristic of the space environment will change the GPS line biases, which could degrade the sensing performance. Design of the spacecraft, including placement of antennas to minimize multipath and thermal control, will be required to resolve these issues.

Initialization: The approach to determining position and attitude on start-up will also change in the LEO environment. The first issue is the increased Doppler shifts. Without any modification, the time required to acquire a particular satellite's signal could be longer than the total time the satellite is in view, potentially resulting in the situation that a position solution is never acquired. This problem can be remedied by including an orbit propagator (also required for the dynamic state estimator). This propagator would estimate the satellite's position and velocity, as well as estimate the NAVSTAR satellite's position and velocity (based on the last recorded almanac data). With this information, the frequency search space would be greatly decreased, thus reducing the time to acquire the GPS satellites [GL97]. Additionally, nearby spacecraft will undergo natural relative motion (as governed by Hill's equations). This relative motion can be used to initialize the biases for the onboard pseudolites.

8.3 Future Work

There are a number of additional research projects in the area of formation flying vehicles that can be explored. The large number of vehicles in a formation offers research opportunities in the areas of distributed control and estimation, path planning, and high level task management. The self-constellation problem (onboard transceivers, no GPS) presents numerous topics related to the self-constellation estimation and initialization problems, near/far problems, self-organizing task planning and mission management. Indeed, many of the issues related to operating a formation will not even become apparent until these future testbeds are built. This future work can be broken into the following areas:



Fig. 8.1: RC Trucks Being Built for an Outside Formation Flying Testbed.

8.3.1 Outdoor Formation Flying Testbed

The blimp vehicles have made a couple of flights outside using the NAVSTAR constellation (see Chapter 7). However, it is apparent that the current vehicles are not suitable for long term research outdoors. The vehicles are only capable of flying outside during the best weather, and on the most calm days. Even then, the disturbances from the slight breezes that are always present can easily saturate the actuators. Another problem is that the helium inside the blimps expands when heated up by the sun, changing the net buoyancy over very short time-scales. These problems, along with the payload weight restrictions and the difficulty moving them outside, make blimps a poor choice for an “outside formation flying testbed”.

A better testbed may be constructed using commercially available RC trucks. These trucks offer a number of advantages:

1. Very cheap to construct and operate. Most RC trucks can be purchased at a local hobby store for anywhere from \$200-\$400.
2. The trucks may be assembled in less than a day, are very durable, and are easy to repair.
3. There is no significant weight restriction. The trucks can easily support 20 lbs of payload. Also, since there is only one RC motor (as opposed to 5 on the blimps), the number of batteries required to operate the vehicle is small. Three batteries should provide enough power to operate it continuously for about one hour.
4. The trucks are small enough that they are easy to port outside, and may be operated under most weather conditions.
5. Although the trucks are not capable of flying, an obstacle course built from ramps could be easily made to allow vertical motions. This will allow testing in 3-D.

Construction of a multi-truck testbed has recently begun. This testbed will be using the same receivers developed for the blimp testbed, as well as a large portion of the software. Figure 8.1 shows some of the RC trucks currently built. Visible on each truck are two antennas which will be used to generate a two-angle attitude solution (which is sufficient, since the roll motion will be constrained to be effectively zero). One of the trucks will also have a pseudolite onboard, as well as a DGPS receiver. This testbed will extend the work on done with the blimps by incorporating more vehicles, and the additional GPS equipment. The outside testbed will then be capable of the following:

1. The absolute formation location will be better than 10 m because the navigation solution will have access to the RTCM message from available beacons.

2. Course relative positioning will be available using differential code. The code measurements inside the highbay suffered from too much multi-path (see chapter 2).
3. The onboard pseudolite will allow the integers to be solved for quite rapidly by having the trucks undergo relative motions. This will allow the relative truck locations to be estimated to cm-level accuracies.

8.3.2 Self-Constellation

Although most formation flying systems will use the NAVSTAR constellation to provide some ranging measurements, there are some applications where this is not possible or even desirable. For example, a deep space formation of spacecraft will not have visibility to the GPS satellites, and will have to incorporate onboard transceivers in order to estimate their relative locations. Even in LEO, a formation of satellites operated by the military, or U.S. intelligence agencies may be specifically designed to operate without access to the GPS constellation in the event the system becomes unavailable.

The multi-truck testbed described in Section 8.3.1 could be used as a self-constellation testbed. In this case, each vehicle would be augmented with its own pseudolite in order to provide ranging measurements between the vehicles within the cluster. With enough trucks in the system, there are enough inter-vehicle measurements to solve for the relative position states in the system.

8.3.3 Next Generation GPS Receiver

The GPS receiver described in chapter 3 has met the requirements of the blimp testbed, and the other projects it is being used on. However, there are several advances in the design that can be made in the future. In particular, there are two major

drawback of the current design. The first is that any data that must be shared *between* the correlator boards must be sent over the serial ports, which does present a bandwidth limitation, especially if more than two boards were used. The second is that the ARM processors must be used to do all the computation, to include closing the tracking loops and solving for the navigation solution, as well as handling the additional algorithms that the user may want to add.

A next-generation receiver could be based on a *bus* architecture, wherein the correlator cards are effectively mounted on PCI cards, and inserted into a simple computer bus. A PC-104 card would also be inserted to handle the computation of the high-level algorithms (pseudo-ranging based navigation, attitude, relative navigation, etc). The clock signal could be routed from a “clock” card (similar to the interface board described in Chapter 3), although whether that goes through the bus, or separate coax cable remains to be seen.

This architecture eliminates the drawbacks described earlier, and allows the user to easily build a receiver with many antennas (more than 4). The user could then add another card with cheap gyros or accelerometers on it to develop inertially aided solutions. This architecture would provide a simple means for a user to tailor the receiver for the specific application.

8.4 Closing

There has been a literal explosion in the use of GPS around the world. GPS has become pervasive in our society, with everyone from sailors to joggers using the system. This trend will continue as GPS receivers are placed into nearly everything, from automobiles to wrist watches. This thesis has described the use of GPS for the

formation flying application, and numerous issues related to it. But this is only the beginning, as researchers continue to think of new applications as yet undreamt of.

Appendix A

This appendix describes the sample problem which was selected to demonstrate the algorithms presented in chapter 5. There were 3 vehicles, each with an onboard pseudolite. For simplicity, each vehicle was modeled as a rigid body. There were assumed to be 7 GPS satellites visible. The corresponding lines-of-sight are given by

$$G = \begin{bmatrix} 0.5754 & 0.5179 & 0.6330 \\ 0.5581 & -0.6140 & 0.5581 \\ -0.6509 & 0.6509 & 0.3906 \\ -0.4924 & -0.6155 & 0.6155 \\ 0 & 0 & 1.0000 \\ 0 & 0.9535 & 0.2860 \\ -0.0976 & -0.9759 & 0.1952 \end{bmatrix} \quad (\text{A.1})$$

The initial positions (m) of the vehicles were $P_1 = (0,0,0)$, $P_2 = (10,0,0)$, and $P_3 = (10,10,10)$. The initial speed of each vehicle was 0. A final configuration constraint of 0 velocity was imposed on each vehicle. The other variables specified in the problem formulation were $C = 2.25$, $d = 3.5$ m, $\text{Thrust}_{\max}/\text{Mass}$ (TTM) = 0.12, $\Delta el_{i \max}^k = 60^\circ$, $\Delta az_{i \max}^k = 60^\circ$, $t_{\min} = 8$ sec, $S_{avg_i}^k = \text{TTM} \times t_{leg}/4$. The sample rate was 1 Hz.

~

Bibliography

- [AC95] Andrew R. Conway, *Autonomous Control of an Unstable Model Helicopter Using Carrier Phase GPS Only*, Ph.D. Dissertation, Stanford University, Dept. of Aeronautics and Astronautics, March 1995
- [AFR] Available on the web at <http://web.fie.com/htdoc/fed/afr/afo/any/text/any/afrba986.htm>.
- [AG74] A. Gelb, *Applied Optimal Estimation*, MIT Press, Cambridge, MA, 1974
- [BA99] A. E. Bryson, *Dynamic Optimization*. Addison Wesley Longman, Inc., California, 1999.
- [BJ82] J. Beser, B. W Parkinson, "The Application of NAVSTAR Differential GPS in the civilian community," *Navigation*, volume 29, no. 2, Summer 1982
- [BM96] M. S. Braasch, "Multipath Effects," *Global Positioning System: Theory and Applications, Volume 1*, Chapter 14, American Institute of Aeronautics and Astronautics(AIAA), Progress in Astronautics and Aeronautics Series, Volume 163, Washington, DC, 1996

- [BP97] P. W. Binning, *Absolute and Relative Satellite to Satellite Navigation using GPS*. Ph.D. Dissertation, Dept. of Aerospace Engineering Sciences. University of Colorado, April 1997.
- [BWP96-1] B. W. Parkinson, "Introduction and Heritage of NAVSTAR, the Global Positioning system," *Global Positioning System: Theory and Applications, Volume 1*, Chapter 1, American Institute of Aeronautics and Astronautics(AIAA), Progress in Astronautics and Aeronautics Series, Volume 163, Washington, DC, 1996
- [BWP96-2] B. W. Parkinson, "GPS Error Analysis," *Global Positioning System: Theory and Applications, Volume 1*, Chapter 11, American Institute of Aeronautics and Astronautics(AIAA), Progress in Astronautics and Aeronautics Series, Volume 163, Washington, DC, 1996
- [CB82] C. A. Balanis, *Antenna Theory: Analysis and Design*, John Wiley and Sons, Inc., New York, NY, 1982
- [CC92] Clark E. Cohen, *Attitude Determination Using GPS*, Ph.D. Dissertation, Stanford University, Dept. of Aeronautics and Astronautics, Dec. 1992
- [CC94] C. E. Cohen, et al., "Real-Time Flight Testing Using Integrity Beacons for GPS Category III Precision Landing," *Navigation*, volume 41, no. 2, Summer 1994
- [CR96] R. D. Chaney, et al. "Reduction of communication requirements for wide-area surveillance systems: multiscale clipping service" *Proceedings of the SPIE - The International Society for Optical Engineering (1996)*, Orlando, FL, April 1996

- [CS97] S. H. Cobb, *GPS Pseudolites: Theory, Design, and Applications*. Ph.D. Dissertation, Stanford University, Dept. of Aeronautics and Astronautics, Dec. 1997
- [DL96] David G. Lawrence, *Aircraft Landing Using GPS*, Ph.D. Dissertation, Stanford University, Dept. of Aeronautics and Astronautics, Sept. 1996
- [DP98] E. Olsen, C. W. Park, and J. P. How, *A GPS Testbed for Multi-Vehicle Control*,. Draper Final Technical Report, Project 909, June 1998.
- [DR99] R. J. DeBolt, P. A. Stadter, "A GPS Formation Flying Testbed for the Modeling and Simulation of Multiple Spacecraft," *Proceedings of the Institute of Navigation ION GPS-99 Conference*, Nashville, Tn, Sept. 1999
- [EL99] E. A. LeMaster, S. M. Rock, "Self-Calibration of Pseudolite Arrays Using Self-Differencing Transceivers," *Proceedings of the Institute of Navigation ION GPS-99 Conference*, Nashville, Tn, Sept. 1999
- [FB96] F. H. Bauer, J. R. O'Donnell, "Space-Based GPS: 1996 Mission Overview," *Proceedings of the Institute of Navigation ION GPS-96 Conference*, Kansas City, MO, Sept. 1996
- [FB97] F. Bauer, J. Bristow, D. Folta, K. Hartman, D. Quinn, J. P. How, "Satellite Formation Flying Using an Innovative Autonomous Control System (AUTOCON) Environment," *Proceedings of the American Institute of Aeronautics and Astronautics (AIAA) Guidance Navigation and Control Conference*, New Orleans, LA, May 1997

- [FB98] F. H. Bauer, K. Hartman, E. G. Lightsey, "Spaceborne GPS: Current Status and Future Visions," *1998 IEEE Aerospace Conference Proceedings*, IEEE, Aspen, CO, March 1998
- [GC90] C. C. Goad, "Optimal Filtering of Pseudoranges and Phases from Single-Frequency GPS Receivers," *Navigation*, volume 37, no. 3, Fall 1990, pp. 249-262
- [GL97] E. Glenn Lightsey, *Development and Flight Demonstration of a GPS Receiver for Space*, Ph.D. Dissertation, Stanford University, Dept. of Aeronautics and Astronautics, Jan. 1997
- [GPS96] B. W. Parkinson, J. J. Spilker, Jr., P. Axelrad, P. Enge, *Global Positioning System: Theory and Applications, Volumes 1 and 2*, American Institute of Aeronautics and Astronautics(AIAA), Progress in Astronautics and Aeronautics Series, Volumes 163 and 164, Washington, DC, 1996
- [HH80] P. Horowitz, W. Hill, *The Art of Electronics*, Cambridge University Press, New York, NY, 1980
- [HT97] E. Harrison Teague, *Flexible Structure Estimation and Control Using the Global Positioning System*, Ph.D. Dissertation, Stanford University, Dept. of Aeronautics and Astronautics, June 1997
- [JCA298] J. C. Adams, J. P. How, "Experiments in GPS Attitude Determination for Spinning Spacecraft with Non-aligned Antenna Arrays," *Proceedings of the Institute of Navigation ION GPS-98 Conference*, Nashville, TN, Sept. 1998

- [JCA96] J. C. Adams, A. D. Robertson, K. Zimmerman, J. P. How, "Technologies for Spacecraft Formation Flying," *Proceedings of the Institute of Navigation ION GPS-96 Conference*, Kansas City, MO, Sept. 1996
- [JCA98] J. C. Adams, J. P. How, "GPS Attitude Determination for Spinning Spacecraft with Non-aligned Antenna Arrays," *Proceedings of the Institute of Navigation National Technical Meeting ION NTM-98 Conference*, Long Beach, CA, Jan. 1998
- [JCA99] J. C. Adams, *Robust GPS Attitude Determination for Spacecraft*. Ph.D. Dissertation, Stanford University, Dept. of Aeronautics and Astronautics, 1999
- [JH99] J. P. How, *ORION Preliminary Design Review Presentation*, Stanford University, Dept. of Aeronautics and Astronautics, April 9. 1999
- [JJS96-1] J. J. Spilker, "GPS Navigation Data," *Global Positioning System: Theory and Applications, Volume 1*, Chapter 4, American Institute of Aeronautics and Astronautics(AIAA), Progress in Astronautics and Aeronautics Series, Volume 163, Washington, DC, 1996
- [JJS96-2] J. J. Spilker, "satellite Constellation and Geometric Dilution of Precision," *Global Positioning System: Theory and Applications, Volume 1*, Chapter 5, American Institute of Aeronautics and Astronautics(AIAA), Progress in Astronautics and Aeronautics Series, Volume 163, Washington, DC, 1996
- [JW78] J. R. Wertz, *Spacecraft Attitude Determination and Control*, D. Reidel Publishing Company, Boston, MA, 1978

- [JW91] J. T. Wu, S. C. Wu, G. A. Hajj, W. I. Bertiger, S. M. Lichten, "Effects of Antenna Orientation on GPS Carrier Phase," *Advances in the Astronautical Sciences*, 91-537, 1991
- [KC93] C. Kee, *Wide Area Differential GPS (WADGPS)*. Ph.D. Dissertation, Stanford University, Dept. of Aeronautics and Astronautics, Dec, 1993
- [KL97] K. Lau, S. Lichten, L. Young, "An Innovative Deep Space Application of GPS Technology for Formation Flying Spacecraft," *Proceedings of the American Institute of Aeronautics and Astronautics (AIAA) Guidance Navigation and Control Conference*, San Diego, CA, July 1996
- [KZ95] K. R. Zimmerman, R. H. Cannon Jr., "Experimental Demonstration of GPS for Rendezvous Between Two Prototype Space Vehicles," *Proceedings of the Institute of Navigation ION GPS-95 Conference*, Palm Springs, CA, Sept. 1995
- [KZ96] Kurt R. Zimmerman, *Experiments in the Use of the Global Positioning System for Space Vehicle Rendezvous*, Ph.D. Dissertation, Stanford University, Dept. of Aeronautics and Astronautics, Dec. 1996
- [LORAL] J. Kurt Brock, et al., "GPS Attitude Determination and Navigation Flight Experiment," *Proceedings of the Institute of Navigation ION GPS-95 Conference*, Palm Springs, CA, Sept. 1995
- [MAT] Matlab, The Mathworks, Inc., Cochituate Place, 24 Prime Park Way, Natick, Ma., 1999

- [MC97] M. Colavita, K. Lau, and M. Shao. "The New Millennium Separated Spacecraft Interferometer," in *Proc. Space Technology and Applications International Forum (STAIF-97)*, (Albuquerque, NM). 1997.
- [MOC97] Michael L. O'Connor, *Carrier Phase Differential GPS for Automatic Control of Land Vehicles*, Ph.D. Dissertation, Stanford University. Dept. of Aeronautics and Astronautics, March 1997
- [MP96] P.Y. Montgomery, *Carrier Differential GPS as a sensor for automatic control. Development of a full state estimation and flight control system for an autonomous aircraft based on the global positioning system..* Ph.D. Dissertation, Stanford University, Dept. of Aeronautics and Astronautics. 1996
- [RB87] R. H. Battin. *An Introduction to the Mathematics and Methods of Astrodynamics*, American Institute of Aeronautics and Astronautics(AIAA), Education Series, New York, NY, 1987
- [RB97] R. E. Best. *Phase-Locked Loops: Design, Simulation, and Applications*. McGraw-Hill, Inc., New York, NY, 1997
- [RF] Available from E.V. Roberts and Associates, Inc.
- [RH99] Personal communication with Cpt. Roger C. Hayward, USMC.. F-18 Pilot (1991-1996).
- [SH94] H. Seywald. "Trajectory Optimization Based on Differential Inclusion." *Guidance, Control and Dynamics*, volume 17, no. 3, pp. 480-487. 1994

- [SJ99] J. M. Stone, J. D. Powell, "Carrier Phase Model for Satellites and Pseudolites," *Proceedings of the Institute of Navigation ION GPS-99 Conference*. Nashville, Tn. Sept. 1999
- [TC97] T. Corazzini, A. Robertson, J. C. Adams, A. Hassibi, J. P. How, "Experimental Demonstration of GPS as a Relative Sensor for Formation Flying Spacecraft," *Navigation*, volume 45, no. 3, Fall 1998, pp. 195-207
- [TC98] T. Corazzini and J. How, "Onboard GPS Signal Augmentation for Spacecraft Formation Flying," presented at the *ION-GPS Conference*. Sept 1998.
- [TC99] T. Corazzini and J. How, "Onboard Pseudolite Augmentation for Relative Navigation," presented at the *ION-GPS Conference*. Sept 1999.
- [TPF] Available on the Web at <http://origins.jpl.nasa.gov/missions/overview.html>.
- [TS21] Available on the Web at <http://www.vs.afrl.af.mil/factsheets/TechSat21.html>.
- [VEL] Available on the web at <http://www.navcen.uscg.mil/gps/geninfo/gpsdocuments/default.htm>
- [VIS] Available on the web at <http://gnctech.gsfc.nasa.gov/gto/tech/formation/roadmap.html>